Poroelastic effects in reservoir modelling

Zur Erlangung des akademischen Grades eines

DOKTORS DER NATURWISSENSCHAFTEN

von der Fakultät für Physik
des Karlsruher Instituts für Technologie

genehmigte

DISSERTATION

von

Dipl.-Geophys. Johannes Benedikt Altmann

aus Freising

Tag der mündlichen Prüfung:	26. November 2010
Referent:	Prof. Dr. Friedemann Wenzel
Korreferent:	Prof. Dr. Serge Shapiro

Table of contents

Table of contents iii

Nomenclature v

Abstract vii

1 Introduction 1

1.1 Poroelastic coupling between pore pressure and stress 1
1.1.1 Effective stress 1
1.1.2 Pore pressure stress coupling 2
1.1.3 Coupling between pore pressure and all stress components 3
1.1.4 Summary, relevance for the thesis 3
1.2 Goals of the thesis 4
1.3 Methods 5
1.3.1 Analytical Modelling 5
1.3.2 Numerical Modelling 5

2 Theory 7

2.1 Stress, stress tensor 7
2.2 Principal stresses 8
2.3 Tectonic stress regimes 8
2.4 Mohr circle 9
2.5 Mohr-Coulomb failure criterion 10
2.6 Sign convention 11
2.7 Finite element method 11

3 Interaction of pore pressure and stress 13

3.1 Effective stresses 13
3.2 Observations and concept of pore pressure stress coupling 14
3.2.1 Pore pressure stress coupling in a normal faulting regime 14
3.2.2 Pore pressure stress coupling in a thrust faulting regime 16
3.2.3 Pore pressure stress coupling in a strike-slip regime 18
3.3 Mathematical expression of pore pressure stress coupling 18
3.4 Coupling during reservoir depletion 19

4 Analytical investigation of pore pressure stress coupling 21

4.1 Poroelastic equations 21
4.1.1 Continuous point injection into homogeneous full space 25
4.1.2 Pore pressure stress coupling – Derivation of the long-term limits 26
4.2 Analytical investigations 28
4.2.1 Spatio-temporal pore pressure, stress and pore pressure stress coupling 28
4.2.2 Influence of tectonic regime on rock stability during fluid injection 33
4.2.3 Influence of tectonic regime on rock stability during fluid depletion 41
4.2.4 Interpretation and discussion 42

5 Numerical Approach 49

5.1 Effective stress in Abaqus 49
5.2 Input-parameters for poroelastic modelling 49
5.3 Homogeneous axis-symmetric model 50

5.3.1 Model setup, boundary conditions, material properties 50
5.3.2 Investigation 52
5.3.3 Results 52
5.3.4 Summary 55
5.4 Inhomogeneous axis-symmetric model 56
5.4.1 Model setup, boundary conditions, material properties 56
5.4.2 Investigation 57
5.4.3 Results 58
5.4.4 Summary and interpretation 65
5.5 Inhomogeneous 3D model 71
5.5.1 Model setup, boundary conditions, material properties 71
5.5.2 Investigation 73
5.5.3 Results 74
5.5.4 Interpretation 81
6 Application to real reservoir geometry 83
6.1 Borehole breakouts 83
6.1.1 Definition 83
6.1.2 Application to reservoir model 85
6.1.3 Borehole breakouts along inclined wellbores 86
6.2 FE model 88
6.2.1 Model generation 89
6.2.2 Model setup 89
6.3 Elastic material properties 91
6.3.1 Material parameters 91
6.3.2 Initial state of stress 95
6.3.3 Model calibration, initial state of stress 98
6.3.4 Model calibration, boundary conditions 99
6.3.5 Results 100
6.4 Poroelastic rheology 102
6.4.1 Material parameters 102
6.4.2 Boundary conditions and model scenario 103
6.4.3 Results 104
6.4.4 Interpretation 107
7 Summary and concluding discussion 109
7.1 Interaction of pore pressure and stress 109
7.2 Discussion of results 110
7.3 Conclusion 113
7.4 Outlook 114
Acknowledgements 115
Appendix A 117
Appendix B 119
Appendix C 121
8 References 125

Nomenclature

c	diffusivity [m^2/s]
e	void ratio
e_0	initial void ratio
g	gravitational acceleration [m^2/s]
h	head [m]
k	permeability [m^2]
k	k-value, ratio of mean horizontal stress to vertical stress
k_f	hydraulic conductivity [m/s]
m_f	fluid mass content per unit volume [kg/m^3]
p	mean stress [Pa]
p_0	initial mean stress [Pa]
p_t^{el}	elastic tensile limit [Pa]
q	fluid volume per unit area and time [m/s]
r	distance [m]
t	time [s]
u_a	average pressure stress in other fluid [Pa]
u_w	average pressure stress in wetting liquid [Pa]
x_i	rectangular coordinates
B	Skempton's coefficient
C	cohesion [Pa]
E	Young's modulus [Pa]
G	shear modulus [Pa]
H	reciprocal of poroelastic expansion coefficient [Pa]
I	unit matrix
J^{el}	elastic volume change
K	permeability [m^3s/kg]
K_d	drained bulk modulus [Pa]
K_f	fluid bulk modulus [Pa]
K_g	grain bulk modulus [Pa]
K_u	undrained bulk modulus [Pa]
P	pore pressure [Pa]
Q	external source, fluid volume per time [1/s]
R	reciprocal of specific storage coefficient at constant stress [Pa]
V_{fl}	injection rate, fluid volume per time [m^3/s]
α	Biot-Willis coefficient
δ	angle of internal friction

δ_{ij}	Kronecker delta
Δ	Change in a variable, used as prefix
ε	strain
ε_t^{el}	logarithmic measure of elastic volume change
ζ	increment of fluid content
η	viscosity [Pa·s]
ϑ	angle around wellbore wall with respect to σ_H; orientation of a potential fracture plane with respect to the minimum principal stress direction σ_3
κ	logarithmic bulk modulus
λ	first Lamé parameter [Pa]
λ_u	undrained first Lamé parameter [Pa]
μ	second Lamé parameter [Pa]
μ^*	coefficient of internal friction
ν	Poisson's ratio
ρ_f	fluid mass density [kg/m^3]
ρ_{f_0}	fluid mass density, reference state [kg/m^3]
ρ_S	solid mass density [kg/m^3]
σ_1	maximum principal stress [Pa]
σ_2	intermediate principal stress [Pa]
σ_3	minimum principal stress [Pa]
σ_h	minimum horizontal stress [Pa]
σ_H	maximum horizontal stress [Pa]
σ_V	vertical stress [Pa]
$\sigma_{h,eff}$	effective minimum horizontal stress [Pa]
$\sigma_{H,eff}$	effective maximum horizontal stress [Pa]
$\sigma_{V,eff}$	effective vertical stress [Pa]
σ_n	normal stress [Pa]
τ	shear stress [Pa]
τ_{crit}	critical shear stress [Pa]
τ_{max}	maximum shear stress [Pa]
φ	porosity
Φ	fluid mass per time [kg/s]
χ	saturation
Ψ	poroelastic stress coefficient

Abstract

Optimized reservoir management is a challenge for today's and future energy supply. Key parameters for reservoir characterization are the pore pressure and stress states and their spatial and temporal changes. However, the changes observed in depleting reservoirs cannot be explained by standard models that are based on a decoupling of stress and pore pressure changes such as Terzaghi´s effective stress principle. In the standard models the minimum horizontal stress can be measured by current borehole logging technology, the maximum horizontal stress cannot be measured and the vertical stress is assumed to be given by the weight of the overburden and not to change. This is in contradiction to the modern interpretation of 4D time lapse seismics, which indicates that during reservoir depletion the vertical stress changes. These changes however, are not included in quantitative description of the reservoir stress state so far.

Key objective of this thesis is to investigate a process called pore pressure stress coupling which is expressed by the ratio of stress change and pore pressure change. This is important for wellbore stability and production from the reservoir. In order to quantify the 4D changes I use analytical and numerical solutions for the coupled poroelastic theory. The analytical approach is used for the principal understanding of the coupling between pore pressure and individual components of the stress tensor. The numerical approach has to be used to study the pore pressure stress coupling in more realistic reservoir setting, as the ultimate goal of this study is to provide means to predict the geomechanics of a depleting reservoir throughout its lifetime.

Here I combined for the first time the 3D analytical solution of the fully coupled poroelastic equations for pore pressure and stress changes in terms of pore pressure stress coupling ratios. The results show that pore pressure stress coupling affects the minimum horizontal stress, the maximum horizontal stress and vertical stress differently. The key consequence of this system behaviour is that the shear stresses in the reservoir change in space and time. This is impacting wellbore stability, the reactivation of reservoir bounding faults, fluid flow within the reservoir and can even cause failure of the reservoir cap rock. The changes of the shear stress can range – depending on elastic reservoir parameters – between 33% to 66% of the pore pressure change and are thus not negligible.

Furthermore, 3D analytical investigation of the pore pressure stress coupling shows that along the maximum principal orientation the shear stress has the maximum increase during fluid injection and maximum decrease during fluid depletion. Vice versa, along the minimum principal stress orientation, the behaviour is reverse.

To investigate the effect of pore pressure stress coupling in inhomogeneous settings I employ for the numerical solution the Finite Element method. To verify the used commercial code Abaqus against the analytical solution I first studied a 3D numerical

homogeneous model and showed the agreement of analytical and numerical results as well as the limitations in terms of boundary effects versus model time. Second I investigated the effect in an inhomogeneous model of a simple reservoir representation. The results show that the permeability contrast between the reservoir and the surroundings is the key parameter for the pore pressure stress coupling.

To test the new approach in a realistic reservoir setting I applied it to a real structure of an oil reservoir. The model consists of eleven layers that have an anticline structure with increasing flexure from top to bottom. One of the layers is the productive zone of the reservoir. The permeability of this layer is by a factor of 1000 higher than the permeability of the surroundings. The reservoir is depleted at nine points within the productive layer for 15 years. Due to the permeability contrast pore pressure changes occur basically inside the productive layer. Maximal negative maximum shear stress changes occur above and below the production point, maximal positive changes horizontally.

In previous approaches the shear stress changes are either absent or would be of different magnitude because they do not consider the differences in pore pressure stress coupling on the individual stress components as in this thesis. These differences can be of key importance in reservoir management such as the drilling of new wells or reservoir stimulation procedures.

1 Introduction

1.1 Poroelastic coupling between pore pressure and stress

Production and injection of fluids and gases into reservoirs, e.g. hydrocarbon production, stimulation of hydrocarbon and geothermal reservoirs, or CO_2 sequestration, causes spatial and temporal pore pressure changes throughout the reservoir and its surroundings. In the case of hydrocarbon production, pore pressure decreases with time, in case of reservoir stimulation and CO_2 sequestration, pore pressure increases with time. The highest pore pressure changes occur near the production or injection wells, and decline with distance to the wells. With duration of production and injection, the pore fluid diffuses with time and thus, the pore pressure change migrates.

1.1.1 Effective stress

Pore pressure counteracts the total stress which is acting on the rock frame. Because fluid is not able to transfer any shear stresses, pore pressure influences the normal stresses, but not the shear stresses. The pore pressure is carrying the normal stresses with the amount of the pore pressure, i.e. the pore pressure reduces the total normal stresses by the amount of pore pressure. This concept of effective stresses was first introduced by Terzaghi (1943), who defined the effective normal stresses as difference between total normal stresses and pore pressure. Now, a pore pressure change and its influence on the state of stress can be considered. If the pore pressure decreases, e.g. for hydrocarbon production, the effective normal stresses increase by the amount of pore pressure change, for pore pressure increase, e.g. geothermal stimulation, vice versa.

Because the pore pressure acts equally on all three normal stresses, and not at all on the shear stresses, the difference of maximum and minimum principal stress, known as differential stress, is constant; only the mean effective stress, known as sum of maximum and minimum principal stress divided by two, changes by the amount of pore pressure. This behaviour is illustrated by means of a Mohr diagram (Figure 1-1). In this plot of shear stress against normal stress, a Mohr circle describes one state of stress for all possible combinations of shear stress and normal stress arbitrary planes perpendicular to the σ_1-σ_3-plane. For fluid injection, and thus pore pressure increase, the Mohr circle shifts to the left in the Mohr diagram, for production (pore pressure decrease) to the right. As the shear stress is not affected by the pore pressure, the circle's diameter or the differential stress is constant.

With the concept of the effective stresses it is possible to explain rock failure during fluid injection, what is observed with stimulation in geothermal wells (Cuenot et al., 2006) or CO_2 sequestration and successfully interpreted to be related to pore pressure diffusion (Shapiro et al., 1998; 2003) or stress transfer (Rozhko 2010; Schoenball et al., 2010). However, production induced seismicity as observed world-wide in oil and gas

fields (Grasso 1992; Davis et al., 1995; Suckale, 2010), can not be explained by the concept of effective stresses.

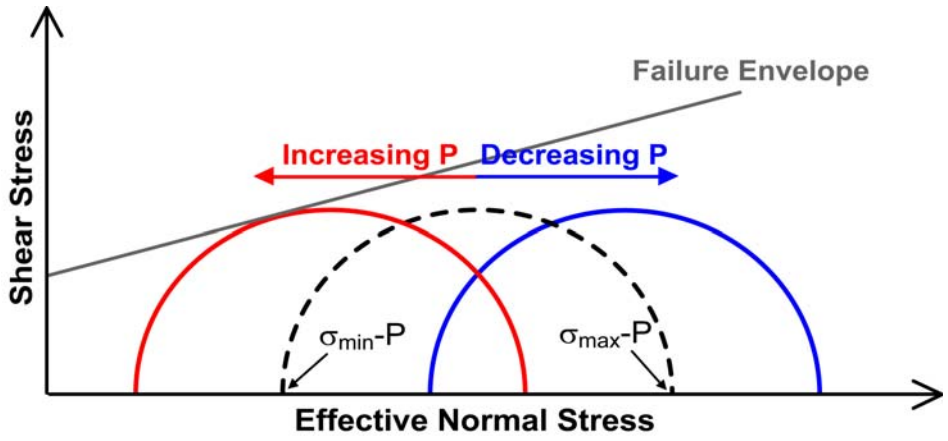

Figure 1-1. Mohr diagram, illustrating the effect of pore pressure change on the effective state of stress. σ_{max} and σ_{min} are equally influenced by the pore pressure, therefore the diameter of the Mohr circle is does not change. The dashed Mohr circle describes an initial state of stress, the red Mohr circle the effective state of stress after fluid injection, the blue Mohr circle the effective state of stress after depletion. During injection of fluid the Mohr circle shifts towards the failure envelope, thus failure becomes more likely. During fluid depletion, failure becomes more unlikely.

1.1.2 Pore pressure stress coupling

Addis (1997), Hillis (2000) or Goulty (2003) developed the concept of effective stresses of Terzaghi (1943) further, and state that pore pressure and total stress are coupled. More precisely, they consider the coupling between pore pressure P and minimum horizontal stress σ_h. Addis (1997) analyses the coupling between P and σ_h during depletion of reservoirs in different tectonic stress regimes, and calls the coupling stress-depletion response of reservoirs. He derives coupling coefficients $\Delta\sigma_h/\Delta P$ depending on the tectonic regime. Based on Engelder and Fischer (1994), who derived a coupling coefficient between P and σ_h, Hillis (2000) compares $\Delta\sigma_h/\Delta P$, what he calls pore pressure stress coupling, for measurements done in reservoirs world-wide. Besides normal faulting and normal compaction, Goulty (2003) considers poroelasticity as one possible coupling effect between P and σ_h. He calls the interaction of P and σ_h reservoir stress path. To consider the coupling between P and σ_h is most common for comparing it to data measured in the field. In hydrocarbon industry mainly σ_h is considered, because it can be determined by methods like hydraulic fracturing or leak off tests (Haimson, 1975). Using the approach of Addis (1997), Hillis (2000) or Goulty (2003), it is possible to explain rock failure due to fluid extraction. Due to the coupling between P and σ_h, the effective minimum horizontal stress increases less than the effective vertical

stress. This leads to an increase in differential stress and an enlargement of the Mohr circle.

Addis (1997), Hillis (2000) and Goulty (2003) have in common that they consider only pore pressure induced variations in minimum horizontal stress. They assume that the vertical stress given by the weight of the overburden is not affected by fluid injection or depletion. They also do not consider any changes in the strength of the coupling depending on the location in the reservoir. Part of this work is to investigate the coupling between pore pressure and all stress components depending on distance to an injection or depletion point, and along different directions with respect to the point source.

In this thesis, I will use the term of Hillis (2000), and call the poroelastic coupling between pore pressure and stress. Different from Hillis (2000), I will use it not to only describe the coupling between P and σ_h, but for the coupling between P and stress in general.

1.1.3 Coupling between pore pressure and all stress components

More recent publications show that the influence of pore pressure on total stress is not limited to σ_h. Vertical stress changes observed by time-lapse investigations (Sayers, 2004; 2006) in combination with geomechanical modelling (Herwanger and Horne, 2005; Settari and Sen, 2007; Schutjens et al., 2010) indicate that not only σ_h, but the entire stress tensor is affected by pore pressure changes. This means that the situation of pore pressure stress coupling becomes more complex. When all stress components are coupled to pore pressure changes, the influence of pore pressure on the effective stresses depends on the strength of the coupling which can be anisotropic. The change in maximum shear stress, $\Delta\tau_{max} = 0.5 \cdot (\sigma_{max} - \sigma_{min})$, between an initial state of stress and a stress state resulted after injection or production is one possibility to evaluate the strength of the effect of anisotropic coupling. Without any anisotropic coupling, $\Delta\tau_{max}$ is zero.

In general, changes in the effective stress affect fluid low in reservoirs and can lead to a number of problematic effects like subsidence, wellbore stability problems, reactivation of reservoir bounding sealing faults and microseismicity (Ruistuen et al., 1999; Hettema et al., 2002; Schutjens et al., 2004). Therefore, it is important to estimate the influence of poroelastic coupling between pore pressure and total stress components, and its consequences.

1.1.4 Summary, relevance for the thesis

Taking coupling between pore pressure and total stress into account, the influence of fluid injection or reservoir depletion, i.e. pore pressure variation, on the state of stress, and thus on rock stability, has been investigated by various authors. Some of the authors

also consider different tectonic regimes and the influence of it on pore pressure stress coupling. Chen and Nur (1992) calculate the effect of pore pressure change on the effective shear stress. They find that in a normal faulting regime the increase of pore pressure leads to stabilization of the rock, and reduction in pore pressure to destabilization, vice versa for a thrust faulting regime. Addis (1997) derives coupling coefficients for different tectonic regimes, and compares his results with measured field data. Hillis (2000; 2001; 2003) has shown that pore pressure increase leads to rock stabilization in a normal faulting, taking coupling between P and σ_h, and no coupling between P and σ_V into account. Goutly (2003) considers poroelasticity as one of three mechanisms that show a coupling between pore pressure and minimum horizontal stress. Soltanzadeh et al. (2009) have published modelling results that show the effect of pore pressure increase or decrease on the state of stress and the rock stability, for different locations. Depending on the location pore pressure increase as well as reduction can lead to both, stabilization and destabilization of the rock.

The influence of pore pressure variation on the state of stress depending on both, the tectonic regime and the location with respect to an injection source are not investigated by any of these authors. Therefore, in this work pore pressure stress coupling is considered in dependence on the location with respect to an injection or depletion point. This allows to investigate the anisotropy of the coupling for all stress components. The change in maximum shear stress is used as parameter to determine the difference of the pore pressure stress coupling depending on stress component and direction with respect to an injection/depletion source. Furthermore, so far the pore pressure stress coupling was considered as temporal constant. Changes of pore pressure stress coupling with time was not investigated. Therefore, a new aspect is the inclusion of the temporal development of fluid flow induced stress changes with duration of injection or depletion, which are realised in this work. In the end, this leads to a 4D model, fluid flow induced pore pressure and stress changes can be investigated in space and time.

1.2 Goals of the thesis

The poroelastic coupling between pore pressure and stress during fluid injection and extraction from reservoirs, and its consequences on the spatial and temporal evolution of the state of stress lead to a couple of questions which are addressed to this work.

a) How strong is the coupling between pore pressure and stress components, and does this coupling develop with duration of injection/production and distance from the injection/production source?

b) Is there a difference in the coupling between pore pressure and individual stress tensor components? If yes, how is the temporal and spatial evolution of the coupling between pore pressure and different stress components?

c) How does the tectonic stress regime influence the coupling between pore pressure and stress?

Concluding, this work should lead to a better understanding of the poroelastic coupling between pore pressure and all stress components as well as its consequences. Local changes in maximum shear stress, the influence of the tectonic stress regime and the reorientation of the stress directions have influence on the rock stability, and therefore can cause problems such as wellbore instabilities, opening and closures of fractures and thus also have impact on the fluid flow in reservoirs.

1.3 Methods

To answer the questions above, two different approaches are used. First an analytical modelling to better understand the spatio-temporal evolution of pore pressure and stress changes in poroelastic media caused by fluid injection/depletion. The analytical equations are also used to investigate qualitatively the spatio-temporal evolution of the anisotropic pore pressure stress coupling. Furthermore, with the finite element modelling a numerical method is used to calculate the influence of pore pressure changes on the state of stress by means of different numerical models. In general, reservoirs are complex underground storage volumes, what it makes necessary to use numerical methods to calculate spatio-temporal pore pressure and stress distributions.

1.3.1 Analytical Modelling

For the analytical modelling, two equations of Rudnicki (1986) are used, which describe the spatial and temporal evolution of pore pressure and stress due to fluid injection/depletion into a poroelastic full space. Using these equations, a pore pressure stress coupling ratio is derived for the entire stress tensor. For different stress components the coupling is calculated and compared to measured field data. The analytical modelling is used also to analyse the anisotropic coupling varying with time for different tectonic stress regimes, what leads to answer the parts of the questions a) to c).

1.3.2 Numerical Modelling

If a mathematical problem is too complex to solve it analytically, numerical methods such as the finite element method are used. With the finite element method, the model continuum is subdivided into small parts, the so-called finite elements. Each of the elements consists of nodes at the element corners and integration points inside the elements. The finite element solver is solving the partial differential equations for each element. The solution is an iterative process, and the solver finishes the calculation when the solution is within a certain limit. Accuracy of the solution depends on the resolution of the finite element model, i.e. the elements' size. The smaller the elements,

the better the solution. Counteracting is the calculation time which increases with higher resolution. After all, one has to find a compromise of accuracy and computation time. To solve the partial differential equations I have used the commercial software Abaqus. The big advantage of Abaqus is that it provides a fully coupled fluid flow stress analysis solver.

First I have built two models with a more simple geometry. A 2D axis-symmetric model, and a 3D block model. Both are described by poroelastic material properties, and continuous fluid injection at one point was used to generate spatio-temporal pore pressure and stress changes. On the one hand, I have used those models to compare the modelling results with the analytical solutions given by Rudnicki (1986). On the other hand to analyse the anisotropic coupling in space and time, and also the influence of different stress regimes on the coupling.

Then, I have set up a 3D model of a real oil reservoir to investigate the poroelastic coupling effects for a more realistic case. This modelling consists of two main parts. At first the geomechanical model was calibrated against stress orientations measured from borehole breakouts to find an initial state of stress. This was done with elastic material parameters describing the model volume. After, poroelastic material properties were used to compute pore pressure and stress changes due to production at several points. Beside pore pressure distribution and evolution, also the anisotropic coupling in terms of change in maximum shear stress was calculated.

2 Theory

Stress plays a major role in this work. Therefore, this chapter gives an brief overview about stress and quantities deduced from stress components. Some of the quantities, such as the maximum shear stress or the orientation of the maximum horizontal stress are later used to quantify the effect of pore pressure changes on the state of stress. The overview given here is based on relevant textbooks like Engelder (1993), Parry (1995), Eisbacher (1996), Turcotte and Schubert (2002) and Jaeger et al. (2007).

2.1 Stress, stress tensor

A force acting on a solid part of the earth, in general generates no acceleration of this part, but causes a counteraction of mechanical resistances. Theses resistances, resulting from the granular structure of the solid, inhibit an acceleration and are called stress. In general, two kind of forces can act on a body, body forces and surface forces. Body forces act on the entire volume of a body and depend on the body mass. In geophysics, the most important body force is the weight, generated by the acceleration of gravity acting on the mass of the earth. The stress vector $\vec{T}$, representing a surface force $\vec{F}_0$ that is acting on a surface A in any arbitrary direction to the surface, is defined as

$$\vec{T} = \lim_{\Delta A \to 0} \frac{\Delta \vec{F}_0}{\Delta A} \tag{2.1}$$

$\vec{F}_0$ can be divided up into a component $\vec{F}_n$ normal to the surface and a component $\vec{F}_s$ parallel to the surface (Figure 2-1). $\vec{F}_n$ and $\vec{F}_s$ acting on a surface A, generate two stress components, normal stress σ_n and shear stress τ, which are defined as

$$\sigma_n = \lim_{\Delta A \to 0} \frac{\Delta \vec{F}_n}{\Delta A}, \qquad \tau = \lim_{\Delta A \to 0} \frac{\Delta \vec{F}_s}{\Delta A}. \tag{2.2}$$

All normal stresses and shear stresses that act on an infinitesimal volume element ($\Delta A \to 0$) describe the state of stress at this infinitesimal volume element. The state of stress can be mathematically expressed as stress tensor σ_{ij} for a three-dimensional coordinate system with the axes x, y, z:

$$\sigma_{ij} = \begin{pmatrix} \sigma_{xx} & \sigma_{xy} & \sigma_{xz} \\ \sigma_{yx} & \sigma_{yy} & \sigma_{yz} \\ \sigma_{zx} & \sigma_{zy} & \sigma_{zz} \end{pmatrix} \tag{2.3}$$

The stress is a normal stress for $i = j$, and a shear stress for $i \neq j$. The first index i stands for the surface normal parallel to one of the coordinate axis, thus defines the surface a stress component is acting on. The second index j stands for the direction a stress component is acting.

As the volume element is in equilibrium and experiences no rotation, one concludes that counteracting shear stresses as the pairs (σ_{xy}, σ_{yx}), (σ_{xz}, σ_{zx}), (σ_{yz}, σ_{zy}) has to be equal. The consequence is that the stress tensor is symmetric.

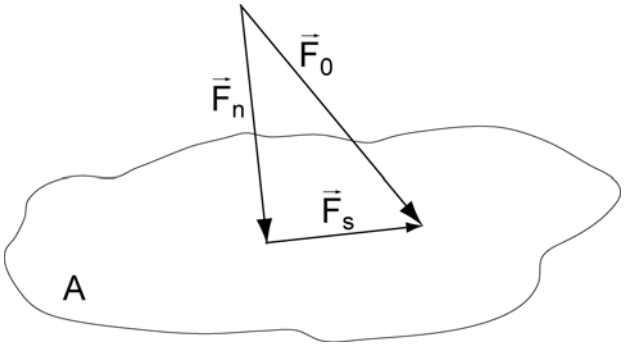

Figure 2-1. Stress vector $\vec{F}_0$, normal component $\vec{F}_n$ and shear component $\vec{F}_s$ acting on surface A.

2.2 Principal stresses

Performing a principal axis transformation, a coordinate system can be found where all shear stresses vanish and the three normal stresses are parallel to the coordinate axes of the transformed system, called principal axes. Then normal stresses are called principal stresses and the stress tensor is defined by the maximum principal stress σ_1, the intermediate principal stress σ_2 and the minimum principal stress σ_3. σ_1, σ_2 and σ_3 are entries on the diagonal of the stress tensor. Therefore, in a principal axis system σ_{ij} represents a diagonal matrix.

2.3 Tectonic stress regimes

In general, the vertical stress σ_V can be considered to be a principal stress. Then, in a principal axis system besides σ_V there are two horizontal principal stresses, the maximum horizontal stress σ_H and the minimum horizontal stress σ_h. Anderson (1905) found that the three tectonic stress regimes, normal, strike-slip and thrust faulting can be characterized by the magnitudes of the principal stresses σ_V, σ_H and σ_h. (Figure 2-2). For the three different tectonic stress regimes, the principal stresses are arranged as follows:

- Normal faulting regime: $\sigma_1 = \sigma_V > \sigma_2 = \sigma_H > \sigma_3 = \sigma_h$
- Strike-slip regime: $\sigma_1 = \sigma_H > \sigma_2 = \sigma_V > \sigma_3 = \sigma_h$
- Thrust faulting regime: $\sigma_1 = \sigma_H > \sigma_2 = \sigma_h > \sigma_3 = \sigma_V$

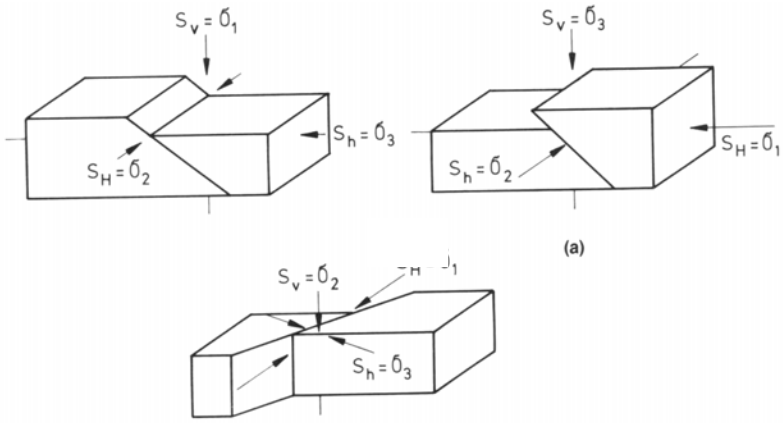

Figure 2-2. Principal stresses in normal faulting (left), strike-slip (middle) and thrust faulting (right) regimes. Figure from Eisbacher (1996).

2.4 Mohr circle

Mohr (1882) developed a graphical tool to illustrate shear and normal stresses on arbitrary oriented shear fracture planes in a rock sample, the principle stresses σ_1 and σ_3 are acting at. All possible combinations of shear and normal stresses on potential failure planes oriented between $0° \leq \vartheta \leq 90°$ describe a semicircle, called Mohr circle, in a τ-σ_n-diagram, called Mohr diagram (Figure 2-3).

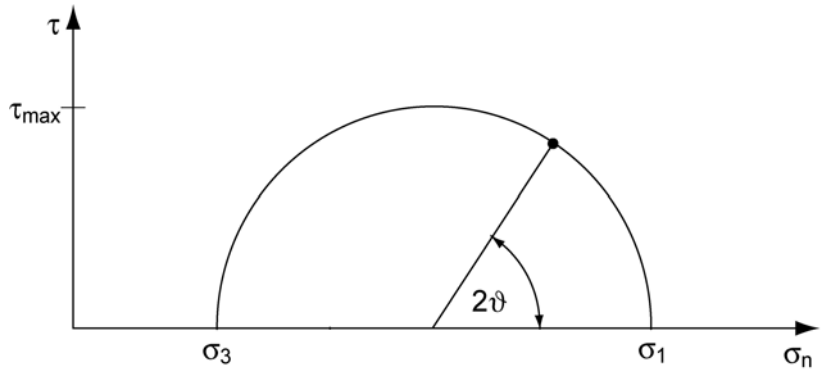

Figure 2-3. Principal of a Mohr circle. A point on the Mohr circle describes one state of stress in terms of normal and shear stress acting on a plane that is inclined by the angle 2ϑ with respect to the direction of the principal axis σ_3. The Mohr circle describes all possible combinations of normal and shear stresses for one state of stress, depending on the orientation (2ϑ) with respect to the principal axes.

The centre of the Mohr circle is determined by $(\sigma_1 + \sigma_3)/2$, the radius and thus also the maximum shear stress τ_{max} given by $(\sigma_1 - \sigma_3)/2$, where σ_1 - σ_3 is called differential stress σ_d. The maximum shear stress occurs for $2\vartheta = 90°$, i.e. for an angle between a possible fracture plane and the principal stresses of 45°.

2.5 Mohr-Coulomb failure criterion

A Mohr circle in combination with a failure criterion allows to analyse a state of stress on a plane with respect to its stability. Most common is the Mohr-Coulomb failure criterion, a brief overview of is given here. The Mohr-Coulomb failure criterion describes the relationship between shear stress τ and normal stress σ_n generated by the principal stresses σ_1 and σ_3, and acting on a potential failure plane inclined by an angle ϑ (Figure 2-4).

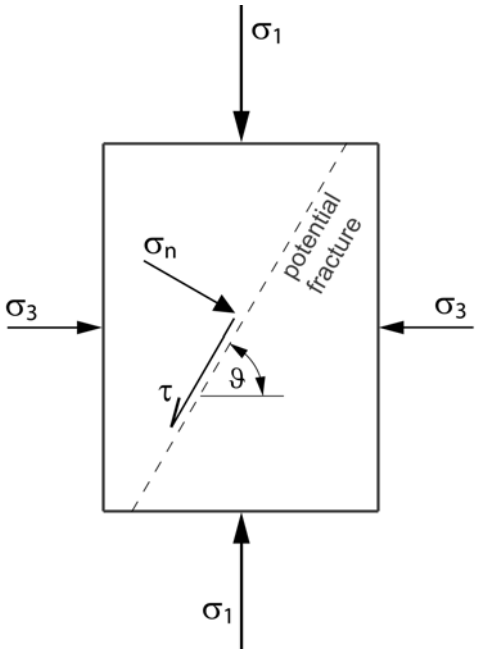

Figure 2-4. Shear stress τ and normal stress σ_n on a potential fracture plane in a rock sample the stresses σ_1 and σ_3 are acting on.

First Coulomb (1776) wrote down an equation for the shear stress that is necessary to cause shear failure on a potential failure plane:

$$\tau_{crit} = C + \mu^* \sigma_n \tag{2.4}$$

where C is a material property, called cohesion, and μ^* is the coefficient of internal friction. Eq. 2.4 is a linear equation with the gradient μ^* of the straight line. μ^* can be expressed by the angle δ between the abscissa and the straight line that is given by Eq. 2.4:

$$\mu^* = \tan\delta \tag{2.5}$$

with the angle of internal friction δ. μ^* should not be mixed up with the coefficient of sliding friction that describes the sliding on planes in broken material. μ^* cannot be measured directly and should be considered to only be the gradient of Eq. 2.4, $\mu^* = (\tau_{crit} - C)/\sigma_n$ (Handin, 1969).

The Mohr diagram together with Eq. 2.4 gives the Mohr-Coulomb failure criterion (Figure 2-5). The straight line given by Eq. 2.4 is called failure envelope, as it determines the onset of failure. All stress states described by Mohr circles that lie under

the failure envelope are in a stable state and no failure would occur. If a Mohr circle is tangent to the failure envelope or is cutting it, failure would occur for those stress states on those planes lying over the failure envelope (red part of the left Mohr circle in Figure 2-5).

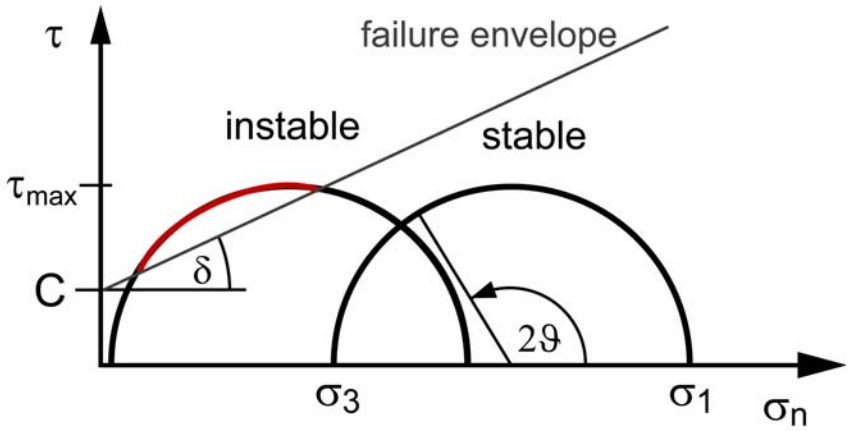

Figure 2-5. The Mohr-Coulomb failure criterion describes the critical shear stress τ_{crit}, that is necessary for failure to occur. τ_{crit} depends on the cohesion C, the angle of internal friction μ^* and the normal stress σ_n, and can be described mathematically by a straight line (failure envelope) (Eq. 2.4). If the shear stress τ, generated by the stress field of σ_1 and σ_3, acting on an arbitrary failure plane exceeds τ_{crit}, failure occurs. Then, stable and unstable stress states can be displayed in a Mohr diagram together with the Mohr-Coulomb failure criterion. If there is no osculation point between Mohr circle and failure envelope, the stress state is stable. If the failure envelope is tangent to the Mohr circle or even cuts it, then the stress state is unstable (red part of the left Mohr circle).

If σ_1 and σ_3 change not at the same amount, the size of the Mohr circle will change. Therefore, considering a change in maximum shear stress $\Delta\tau_{max}$ between two stress states, is a parameter for a not equal change of σ_1 and σ_3. As a major point in this work is the evaluation of induced anisotropic stress changes, $\Delta\tau_{max}$ is used as parameter for it.

2.6 Sign convention

Handling with stresses means to decide which sign do compressive and tensile stresses have. There exist two different views: In engineering sciences compressive stress is defined as negative, tensile stress as positive, in geo-science it is vive versa. In the course of this thesis I came in contact with both of these definitions. In order not to switch between those sign conventions, I decided to use the geo-science sign convention for the entire thesis, i.e. in the following compressive stresses are positive, tensile stresses negative.

2.7 Finite element method

A major part of this work is done by numerical modelling using the finite element method. Therefore, I will give a brief summary about the very basic idea of the finite

element method. Because the theory of the finite element method is quite complex, more than a short overview cannot be provided here. For more detailed information about the finite element method, see Zienkiewicz and Taylor (1994). If a partial differential equation cannot be solved analytically anymore, numerical methods such as the finite element method are used. Applying the finite element approach, a continuum is discretized into small parts, called finite element. These element have simple shapes, in the case of three-dimensional elements, in general they are tetrahedra or hexahedra. The elements consist of element nodes at the corner of the element and integration points inside the elements. At element nodes scalar and vectorial parameters such as temperature and displacement are calculated, at integration point tensorial parameters such as stress and strain. Tetrahedra elements consist of four nodes and one integration point, hexahedra elements of eight nodes and eight integration points. With tetrahedra elements more complex structures can be built than with hexahedra elements that give a more exact solution at a higher computing time. Because coupled fluid flow stress simulations requires more than one integration point, I have used tetrahedra elements in my work.

The finite element solver calculates a function as approximation to the exact solution of the partial differential equations in each element. In model areas a strong change in the solution of the function is expected, the resolution of the dicretization has to be higher. Higher resolution and thus more elements increase the number of equations to be solved, and thus computation time. Therefore, one also has to weigh up precision of the result and computation time. Especially for a transient fluid flow stress analysis with hexahedra elements, the computation time can increase quickly. For example, one time iteration of the geomechanical model of chapter 6 (~260,000 hexahedra elements) takes about 45 minutes. For a transient analysis with 65 time increments and in average two iterations per increment, the entire computation time is more than four days.

As numerical solver I have used the commercial software Abaqus. This software provides a fully coupled fluid flow stress analysis solver. In general, the main advantage of the finite element method is, that it can handle complex geometries. These can be discretized by a variety of different elements which can vary both in size and shape. This enables to discretize models in such way that parts of interest and strong variations in the field variable can be resolved highly, and parts of less interest and small variations in the field variable are performed with a coarse element mesh.

3 Interaction of pore pressure and stress

Pore pressure and stress changes in the underground can lead to spectacular and hazardous phenomena, such as blowouts in wells that unexpectedly drill into overpressured sequences, induced seismicity or mass movements such as landslides. This chapter describes the interaction of pore pressure and stress, mathematically by means of basic equations, by demonstrating field measurements of coupled pore pressure and stress changes, and by comparison of the effect of pore pressure stress coupling for different tectonic stress regimes.

3.1 Effective stresses

Changes in pore pressure affect the state of stress. Terzaghi (1943) developed a concept of how pore pressure is affecting the state of stress, and introduced effective stresses. In the case of principal stresses, the effective principal stresses $\sigma_{V,eff}$, $\sigma_{H,eff}$, $\sigma_{h,eff}$ are defined as subtraction of pore pressure P from the total principal stresses σ_V, σ_H, σ_h, thus are determined by:

$$\sigma_{V,eff} = \sigma_V - P, \qquad \sigma_{H,eff} = \sigma_H - P, \qquad \sigma_{h,eff} = \sigma_h - P \qquad (3.1\ a,b,c)$$

So, the effective state of stress describes the state of stress under consideration of a pore pressure, which is reducing the normal stresses by the amount of the pore pressure.

Assuming the total stresses don't change, a greater pore pressure is generating lower effective stresses, and vice versa. As the pore pressure is describing a fluid's pressure, no shear stresses can be transferred by the pore pressure. Thus, the pore pressure affects only the effective normal or effective principal stresses, but not the shear stresses. How this behaviour is affecting the effective state of stress can be illustrated by means of a Mohr diagram (Figure 1-1).

Summarizing Terzaghi's (1943) concept of effective stresses, the pore pressure reduces ($P > 0$) or increases ($P < 0$) the effective normal and effective principal stresses, respectively. In this concept the total stresses are independent of P, and the pore pressure itself has no influence on the shear stresses, Mohr circles don't change their diameter, only their horizontal position in a Mohr diagram (Figure 1-1), if P is changing. Assuming an increasing pore pressure the effective state of stress becomes more instable, for a decreasing P on the other hand more stable. Because the effective principal stresses increase or reduce all by the amount of P, they are independent of the tectonic regime. Therefore Figure 1-1 is valid for every tectonic regime.

Enhanced geothermal systems are increasing the pore pressure by pumping water into the rock, because they want to enlarge joints to generate aquifers. The result of cracking the rock and generating seismicity can be explained by the concept of effective stresses. For an increasing pore pressure the Mohr circle is moving to the left towards the failure

envelope, so the rock is becoming more instable. On the other hand, extraction of fluid increases the effective normal stresses, what leads to a stabilization of the rock.

3.2 Observations and concept of pore pressure stress coupling

Observations show an increased occurrence of seismicity in areas of hydrocarbon production. This contradicts the idea of rock stabilisation due to reduction of pore pressure, according to the concept of effective stresses (Terzaghi, 1943). Numerous authors have questioned and investigated the relationship between fluid or gas extraction from subsurface reservoirs and the occurrence of seismicity and the triggering of earthquakes, respectively. Induced earthquakes and microseismicity are studied for different oil and gas fields in the USA and Canada (Segall, 1989; Doser et al., 1992; Nicholson and Wesson, 1992; Rutledge et al., 1998; Simpson, 1986), the Netherlands (van Eck et al., 2006; van Eijs et al., 2006), the Lacq gas-field in France (Feignier and Grasso, 1990; Grasso and Wittlinger, 1990; Bardainne et al., 2008; Segall et al., 1994) or an oil and gas field in the Fahud Salt Basin in Oman (Sze et al., 2005). A triggering of three ms = 7.0 earthquakes at Gazli, Uzbekistan, near a major gas field, is hypothesized by Simpson and Leith (1985).

Together with the observation of seismicity in the vicinity of producing hydrocarbon reservoirs, minimum horizontal stresses σ_h and pore pressures P are measured in oil and gas fields. Teufel (1996) provides data for different fields in the North Sea and the USA. Hillis (2000) gives an overview of σ_h- and P-measurements done worldwide (Table 1). Hillis (2000) distinguish between field-scale data and basin-scale data, measured in depleting and in over-pressured reservoirs. Those measurements give strong evidence that σ_h and P are coupled, what is called pore pressure stress coupling, pore pressure/σ_h coupling (Hillis, 2000), also known as stress-depletion response (Addis, 1997). The strength of the coupling is expressed by the ratio $\Delta\sigma_h/\Delta P$, what brings pore pressure change in relation to change in σ_h, i.e. the larger $\Delta\sigma_h$ for a given ΔP, the stronger the coupling.

$\Delta\sigma_h/\Delta P$-values calculated from σ_h- and P-measurements at different reservoirs in the North Sea and the USA (Teufel, 1996) show values between 0.48 for the McAllen Ranch field, Texas, and 0.86 for the Eldfisk field, North Sea. In the overview of Hillis (2000) $\Delta\sigma_h/\Delta P$ is ranging between 0.34 and 1.18, with an average of 0.64 (Table 1).

3.2.1 Pore pressure stress coupling in a normal faulting regime

How pore pressure stress coupling is affecting the state of stress and the rock stability, is illustrated in a Mohr diagram (Figure 3-1). It shows a Mohr circle representing an initial state of stress (dashed line) for a normal faulting regime, i.e. $\sigma_{max} = \sigma_V$ and $\sigma_{min} = \sigma_h$, what is a typical regime for sedimentary basins (Hillis, 2000). Hillis (2000) assumes

that σ_V is not affected by changes in P, therefore, for increasing P, $\sigma_{V,eff}$ is reducing by the amount of pore pressure increase. Under consideration of coupling between P and σ_h, an increase in pore pressure leads to an increase in σ_h. The consequence is that $\sigma_{h,eff}$ decreases not by P, but by a reduced amount determined by the strength of the coupling, $\Delta\sigma_h/\Delta P$.

Therefore, for increasing pore pressure the effective differential stress is decreasing, a smaller Mohr circle (red line) compared to the initial one (dashed line) is the consequence. Hence, an increase of pore pressure can lead to stabilization of the rock. On the contrary, a decreasing pore pressure leads to a reduction in σ_h and thus $\sigma_{h,eff}$ is increasing less, whereas σ_V is unaffected by P and therefore $\sigma_{V,eff}$ is increasing by the amount of pore pressure decrease. The consequence is an increasing effective differential stress, what leads to a larger Mohr circle (blue line) approaching the failure envelope.

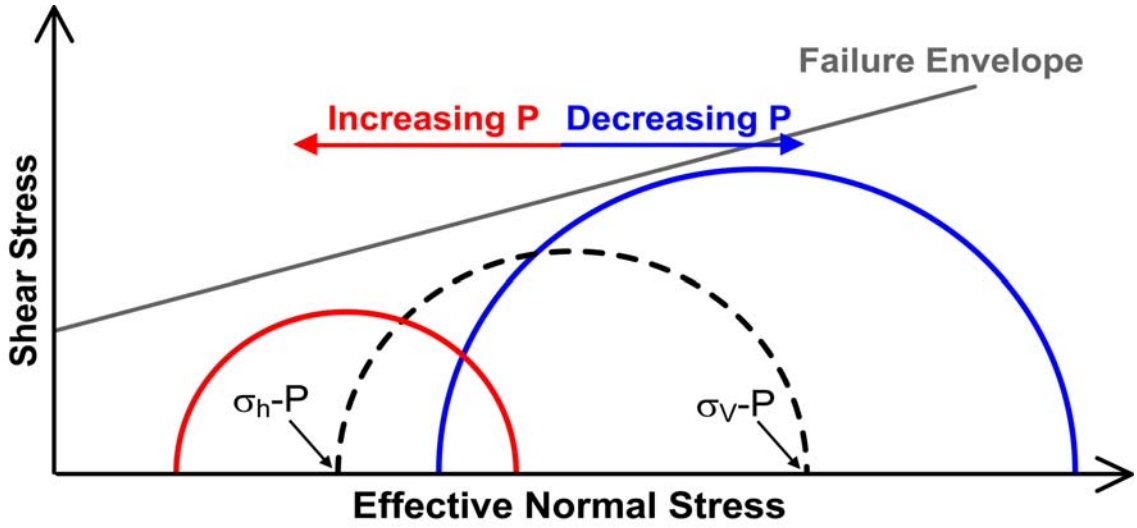

Figure 3-1. Mohr diagram under consideration of pore pressure stress coupling. For a given initial state of stress (dashed line) the effective differential stress is reduced for increasing pore pressure (red line). Decreasing *P* has the contrary effect (blue line).

The resulting effective stresses, under consideration of pore pressure stress coupling, are expressed by

$$\sigma'_{V,eff} = \sigma_{V,eff} - \Delta P' , \qquad \sigma'_{h,eff} = \sigma_{h,eff} + \frac{\Delta\sigma_h}{\Delta P}\cdot\Delta P' - \Delta P' . \qquad (3.2\ \text{a,b})$$

$\sigma_{V,eff}$ and $\sigma_{h,eff}$ represent the initial effective state of stress given by $\sigma_{V,eff} = \sigma_V - P$ and $\sigma_{h,eff} = \sigma_h - P$. Then the effective state of stress after a pore pressure change $\Delta P'$, $\sigma'_{V,eff}$ and $\sigma'_{h,eff}$, are given by Eqs. 3.2. $\Delta\sigma_h/\Delta P$ is the pore pressure stress coupling ratio and describes the strength of the coupling. Without coupling, $\Delta\sigma_h/\Delta P = 0$, Eqs. 3.2 are identical with Terzaghi's (1943) effective stresses (Eqs. 3.1).

Hence, the concept of pore pressure stress coupling, as described by various authors (Engelder and Fischer (1994), Hillis (2000; 2003), Tingay et al. (2003)) allows explaining the occurrence of seismicity in the context of production, i.e. pore pressure decrease.

Table 1. Pore pressure stress coupling ratios obtained from measurements at different reservoir sites. Table is modified after Hillis (2000). Data are based on Addis (1997), Bell (1990), Breckels and van Eekelen (1982), Hillis (2000), Salz (1977), Teufel et al. (1991), Tingay (pers. communication), Whitehead et al. (1987), Woodland and Bell (1989).

Area	Scale	$\Delta\sigma_h/\Delta P$
Scotian shelf, Canada	Over-pressured basin	0.76
North West shelf, Australia	Over-pressured basin	0.75
Gannet and Guillemot fields, North Sea	Over-pressured basin	0.60
Vicksburg formation, South Texas	Depletion in field	0.48
Travis Peak formation, East Texas	Depletion in field	0.57
Alberta basin, Western Canada	Depletion in field	0.34
Ekofisk field, North Sea	Depletion in field	~0.8
US Gulf Coast	Depletion in field and over-pressured basin	0.46
Lake Maracaibo, Venezuela	Depletion in field	0.56
Baram Delta Province, Brunei	Depletion in field and over-pressured basin	0.59
Magnus field, North Sea	Depletion in field	0.68
West Sole field, North Sea	Depletion in field	1.18
Wytch Farm field, UK	Depletion in field	0.65
Venture field, Canada	Over-pressured basin	0.56
Nile Delta, Egypt	Over-pressured basin	0.65

3.2.2 Pore pressure stress coupling in a thrust faulting regime

The above described approach considers only stress states in a normal faulting regime, and is based on the assumption that the vertical stress is not affected by pore pressure changes. In the following, the effect of pore pressure stress coupling is extended to the consideration of a thrust faulting regime ($\sigma_{max} = \sigma_H$, $\sigma_{min} = \sigma_V$) and again under the assumption that the total vertical stress is not affected by changes in P. According to Segall (1989) both normal faulting and thrust faulting is developing during the depletion of a reservoir. Normal faulting occurs on the flanks of the reservoir; thrust faulting

above and below the reservoir (Figure 3-2). How fluid depletion, under the assumption of constant vertical stress, is affecting the effective state of stress in a thrust faulting regime, and hence the rock stability, is shown in Figure 3-3.

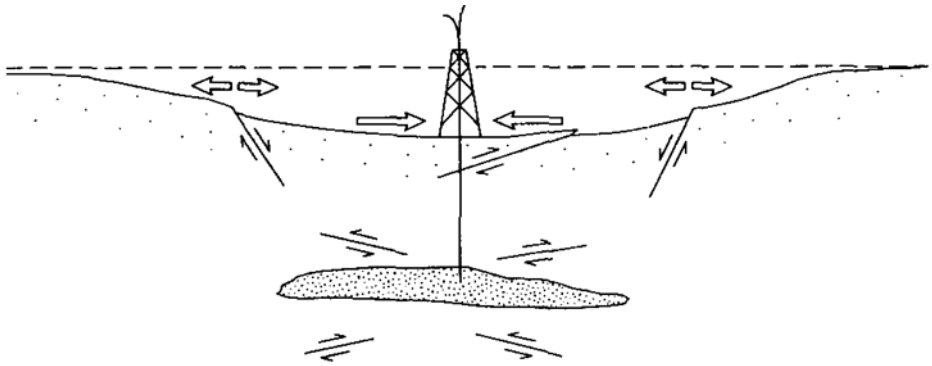

Figure 3-2. Stress regimes developing around a depleting reservoir. On the flanks of the reservoir normal faulting is occurring, above and below the reservoir thrust faulting. Open arrows indicate horizontal strain at the surface. Figure from Segall (1989).

Depletion or pore pressure decrease in a thrust faulting regime has the opposite effect as in a normal faulting regime. Due to the coupling of P and σ_H, σ_H is decreasing with P, and thus $\sigma_{H,eff}$ is increasing less than $\sigma_{V,eff}$, which increases by P because of the non-coupling between P and σ_V. The consequence is a reduction in effective differential stress, what leads to a smaller Mohr circle (blue line), which moves to the right, away from the failure envelope, due to pore pressure decrease. This means, under the aspect of pore pressure stress coupling, depletion in a thrust faulting regime intensifies rock stabilization, because both stabilization-effects, a movement to the right, away from the failure envelope, and a decreasing circle diameter are superposing.

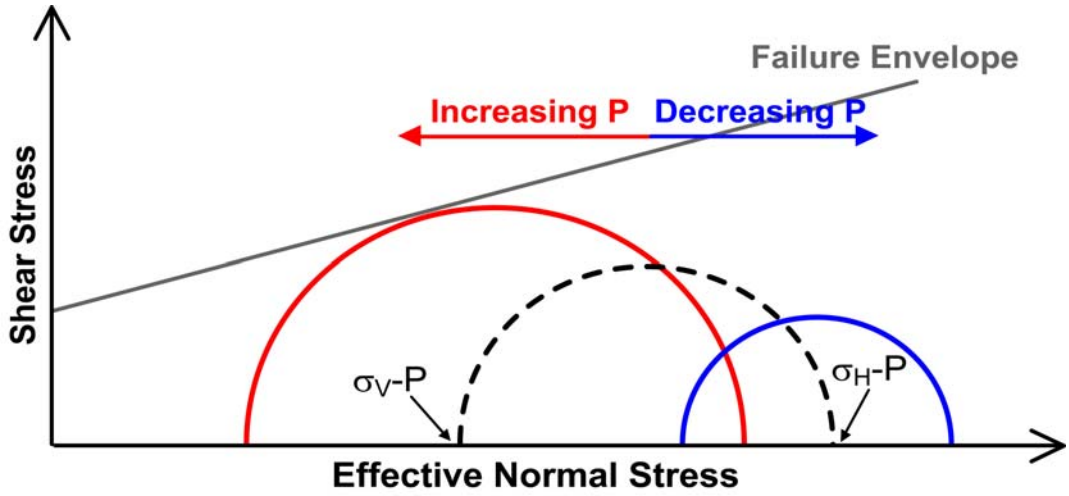

Figure 3-3. Mohr diagram, showing the effect of pore pressure increase (red line) and decrease (blue line) on an initial effective state of stress (dashed line) under consideration of a thrust faulting regime, and the assumption that the vertical stress is not affected by pore pressure change.

On the other hand, fluid injection, i.e. increase of pore pressure, has the opposite effect. Due to pore pressure stress coupling the effective differential stress increases (larger Mohr circle), and the Mohr circle moves to the left towards the failure envelope (red line) because of the increasing pore pressure. Those two effects superpose, and thus amplify the effect of rock destabilization.

Summarizing, under consideration of pore pressure stress coupling, the influence of pore pressure increase and decrease, respectively, on the state of stress, and thus on the rock stability is strongly dependent on the stress regime. In a normal faulting regime pore pressure reduction brings rock closer to failure, in a thrust faulting regime stabilization of the rock is the consequence. On the other hand, an increase in pore pressure results in rock stabilization in a normal faulting regime, and in destabilization in a thrust faulting regime. Hence, the tectonic regime leads to opposite effects concerning the influence of pore pressure change on the rock stability.

As mentioned above, the concept of pore pressure stress coupling is based on the assumption that the pore pressure is affecting the total horizontal stresses, but not σ_V (Engelder and Fischer, 1994; Hillis, 2000). However, time-lapse investigations (Sayers, 2004; 2006) and results of geomechanical modelling (Herwanger and Horne, 2005; Settari and Sen, 2007; Schutjens et al., 2010) show that σ_V is not a constant. This indicate that not only σ_h, but the entire stress tensor is affected by pore pressure changes. To investigate the coupling between P and σ_V , an analytical model (chapter 4) as well as a numerical model (chapter 5) are used. Hereby the effect of fluid injection, i.e. pore pressure increase, on the state of stress is investigated.

3.2.3 Pore pressure stress coupling in a strike-slip regime

Considering a strike-slip regime, i.e. $\sigma_{max} = \sigma_H$ and $\sigma_{min} = \sigma_h$, both maximum and minimum horizontal stresses are equally affected by pore pressure stress coupling. This means that the pore pressure stress coupling does not have any effect on the differential stress, and thus on the size of the Mohr circle. Thus, in a strike-slip regime the Mohr circle is only horizontally shifted in the Mohr diagram during fluid injection or depletion.

However, the coupling between pore pressure and total horizontal stresses leads to an increase of both maximum and minimum horizontal stress during fluid injection, and to a bigger effective stresses than without coupling. The reverse effect applies for depletion. In chapter 4.2 this effect is analysed in more detail.

3.3 Mathematical expression of pore pressure stress coupling

Changes in σ_h depending on P are described by the theory of poroelasticity (Biot, 1943), which in general describes the effect of adding or removing fluid from the soil on the mechanical behaviour of the rock. Using the theory of poroelasticity and under uniaxial

strain conditions, i.e. no lateral expansion or a horizontally infinite reservoir, Engelder and Fischer (1994) derive a space-and time-independent relationship between σ_h, σ_V and P:

$$\sigma_h = \frac{\nu}{1-\nu}\sigma_V + \alpha\frac{1-2\nu}{1-\nu}P \tag{3.3}$$

with the Biot-Willis coefficient α, defined as

$$\alpha = 1 - \frac{K_d}{K_g} \tag{3.4}$$

where K_d is the drained bulk modulus and K_g the bulk modulus of the grains. The vertical stress σ_V is given by the weight of the overburden. Engelder and Fischer (1994) assume that σ_V doesn't change during fluid injection or depletion. Under this assumption and considering a pore pressure change, Eq. 3.3 reduces to

$$\frac{\Delta\sigma_h}{\Delta P} = \alpha\frac{1-2\nu}{1-\nu}. \tag{3.5}$$

Eq. 3.5 allows to calculate a value for the coupling between σ_h and P. Using typical values for α and ν, e.g. $\alpha = 0.8$, $\nu = 0.25$, coupling ratio results in $\Delta\sigma_h/\Delta P = 0.53$. This is in agreement with the values obtained from σ_h- and P-measurements (Table 1). However, Eq. 3.5 is not able to explain the variability of the measured values, which range between 0.34 and 1.18. The variations in the coupling coefficient could result from changes in the Biot-Willis coefficient with depletion or within the reservoir as was investigated by Addis (1997). He calculates pore pressure stress coupling ratios and compares them to field measurement data. Also the use of non-unity values for the Biot-Willis coefficient depending on the porosity shows no satisfying match for the West Sole and Wytch Farm fields. Another reason for the variability of the measured data could be the fact that $\Delta\sigma_h/\Delta P$ is not a constant value within a reservoir, but depends on the time of measurement, i.e. time after start of injection or production, and on the location of measurement. Teufel et al. (1991) and Zoback and Zinke (2002) analysed σ_h- and P-data measured at oil reservoirs in the North Sea, and obtain $\Delta\sigma_h/\Delta P$-values depending on the measurement location: on the crest, the flank or the outer flank of the reservoir. $\Delta\sigma_h/\Delta P$, measured at the Tor formation of the Valhall field, varies between 0.70 at the crest and 0.88 at the flank of the reservoir.

3.4 Coupling during reservoir depletion

Addis (1997) and Goulty (2003) investigate the coupling between pore pressure and σ_h due to depletion of different oilfields. Besides pore pressure stress coupling, this coupling is also called stress-depletion response of reservoirs (Addis, 1997) or reservoir stress path (Goulty, 2003). Addis (1997) uses the passive basin response to explain most of the field data. The passive basin response assumes a passively and elastically reacting

reservoir during production and pressure decline. The passive basin response equation is given by

$$\frac{d\sigma_h}{dP} = \alpha\left(1 - \frac{\nu}{1-\nu}\right). \tag{3.6}$$

The passive basin response depends on the Biot-Willis coefficient and the Poisson's ratio. Besides Biot-Willis coefficients equal one, Addis (1997) considers Biot-Willis coefficients depending on the porosity. In addition he differentiates between the tectonic stress regimes depletion is occurring in, and defines mathematical equations of the stress-depletion responses for the three tectonic regimes.

Goulty (2003) specifies three mechanisms that govern the reservoir stress path, normal compaction, normal faulting and poroelasticity, and provides equations for $\Delta\sigma_h/\Delta P$ for each mechanism. Normal compaction is a mechanical compaction caused by irreversible reduction in porosity of sediments due to increasing the mean effective stress. Reservoir depletion resulting in pore pressure reduction causes the mean effective stress to increase. Then, the sediments undergo normal compaction during production with irreversible loss of porosity. Normal faulting describes the active faulting in rocks due to reservoir depletion. Goutly (2003) links the reservoir stress path with the Mohr-Coulomb failure criterion, and derives and expression for it depending on the coefficient of friction. The poroelastic mechanism is based on the theory of poroelasticity of Biot (1941), and analogous to Engelder and Fischer (1994) Goulty (2003) derives the equation of pore pressure stress coupling (Eq. 3.5).

In this work I concentrate only on the poroelastic effect between coupled pore pressure and stress changes. To further investigate the space- and time-dependence of the pore pressure stress coupling ratio, I use two different approaches, an analytical (chapter 4) and a numerical (chapter 5) one. The first is based on the spatio-temporal solutions for pore pressure and stress in an infinite homogeneous poroelastic medium after continuous fluid injection at one point (Rudnicki, 1986). With these equations a space- and time-dependent pore pressure stress coupling ratio can be calculated, which, for time tending towards infinity, results in Eq. 3.5. The second approach considers a numerical modelling of the fluid injection induced spatio-temporal pore pressure and stress distribution inside and around an ellipsoidal reservoir.

4 Analytical investigation of pore pressure stress coupling

As shown previously, the pore pressure stress coupling ratio is neither a constant considering different reservoirs nor constant inside one single reservoir, but depends on location and time of measurement. Therefore, the spatio-temporal character of $\Delta\sigma_h/\Delta P$ is analytically and numerically investigated in the following. The analytical part is based on the solutions for spatio-temporal pore pressure and stress changes due to continuous fluid injection in an infinite homogeneous poroelastic medium, which were derived by Rudnicki (1986). These equations enable to calculate a space- and time-dependent pore pressure stress coupling ratio, which again results in Eq. 3.5 for time tending towards infinity, what is briefly shown in chapter 4.1.2 and in detail in Appendix A.

As the analytical approach after Rudnicki (1986) is limited to an infinite homogeneous space, which is not a suitable description of a reservoir embedded in surroundings, numerical modelling is used in a next step. There, the influence of inhomogeneous material properties as well as the reservoir shape on the spatial and temporal stress and pore pressure distribution can be investigated.

4.1 Poroelastic equations

In the following a diffusion equation is derived, which Rudnicki (1986) solved in order to obtain the solutions for spatio-temporal pore pressure and stress changes due to continuous fluid injection at a point source in infinite homogenous poroelastic full space. The diffusion equation is based on the poroelastic theory of Biot (1941) for isotropic fluid-saturated porous media, and later derived by Rice and Cleary (1976) in a more direct formulation (Rudnicki, 1986). Wang (2000), whose approach I follow here, describes the derivation in detail.

The fluid mass content m_f, defined by Rice and Cleary (1976), is the fluid mass per unit reference volume. Then, the change in fluid mass content is given by $\delta m = m_f - m_0$, with the fluid mass content in the reference state, m_0. The increment of fluid content ζ is defined as

$$\zeta = \frac{\delta m_f}{\rho_{f_0}} \tag{4.1}$$

with the fluid density in the reference state, ρ_{f_0}. As δm_f is mass content per unit volume, ζ is a dimensionless variable standing for the fluid volume transported into or out of storage.

In principal coordinates the constitutive equations which relates strain ε and increment of fluid content ζ with stress σ and pore pressure P are given by four equations for four

dependent variables (ε_1, ε_2, ε_3, ζ) each depending on four independent variables (σ_1, σ_2, σ_3, P):

$$\varepsilon_1 = \frac{1}{E}\sigma_1 - \frac{\nu}{E}\sigma_2 - \frac{\nu}{E}\sigma_3 + \frac{1}{3H}P \tag{4.2}$$

$$\varepsilon_2 = -\frac{\nu}{E}\sigma_1 + \frac{1}{E}\sigma_2 - \frac{\nu}{E}\sigma_3 + \frac{1}{3H}P \tag{4.3}$$

$$\varepsilon_3 = -\frac{\nu}{E}\sigma_1 - \frac{\nu}{E}\sigma_2 + \frac{1}{E}\sigma_3 + \frac{1}{3H}P \tag{4.4}$$

$$\zeta = \frac{1}{3H}\left(\sigma_1 + \sigma_2 + \sigma_3\right) + \frac{1}{R}P \tag{4.5}$$

Neglecting the pore pressure added in Eqs. 4.2-4.5, they represent the equations of linear elasticity (Turcotte and Schubert, 2002). Eqs. 4.2-4.5 contain in total four poroelastic moduli: E and ν are known from standard elasticity theory as Young's modulus and Poisson's ratio, $1/H$ is called poroelastic expansion coefficient, is defined by

$$\frac{1}{H} \equiv \left.\frac{\delta\varepsilon}{\delta P}\right|_{\sigma=0} \tag{4.6}$$

and describes the change in bulk volume due to a change in pore pressure under constant stress conditions. The poroelastic modulus $1/R$ is defined by

$$\frac{1}{R} \equiv \left.\frac{\delta\zeta}{\delta P}\right|_{\sigma=0}. \tag{4.7}$$

$1/R$ is the specific storage coefficient at constant stress, also called unconstrained specific storage coefficient, and describes the change in increment of fluid content, i.e. the change in fluid volume added or remove from storage, due to pore pressure change under constant stress.

Adding Eqs. 4.2-4.4 and using the mean normal stress $\sigma = \left(\sigma_1 + \sigma_2 + \sigma_3\right)/3$, Eqs. 4.2-4.5 result in

$$\varepsilon = \frac{1}{K_d}\sigma + \frac{\alpha}{K_d}P \tag{4.8}$$

$$\zeta = \frac{\alpha}{K_d}\sigma + \frac{\alpha}{K_d B}P \tag{4.9}$$

where the relationships

$$B = \frac{R}{H}, \qquad \alpha = \frac{K_d}{H}, \qquad K_d = \frac{E}{3(1-2\nu)} \tag{4.10}$$

are used. α is the Biot-Willis coefficient (Eq. 3.4) and B is the Skempton's coefficient which is defined as ratio of pore pressure change due to a change in applied stress under

undrained conditions, i.e. no fluid exchange is allowed taking place, what is formally expressed by setting the increment of fluid content ζ equal to zero:

$$B \equiv \left.\frac{\delta P}{\delta \sigma}\right|_{\zeta=0} \tag{4.11}$$

After undertaking a series of experiments (Figure 4-1), measuring the amount of fluid flowing out of a water saturated sand column due to gravity forces, Darcy (1856) found an empirical relationship describing fluid flow through a porous medium. Darcy's law is given by

$$q_z = -k_f \frac{dh}{dz} \tag{4.12}$$

with the volume of fluid per unit area and time, q_z, the head h and the constant of proportionality k_f. k_f is the hydraulic conductivity in [m/s] and depends on the gravitational acceleration g, the permeability k [m^2], and on the fluid properties viscosity η [Pa·s] and fluid density ρ_f:

$$k_f = \frac{\rho_f g k}{\eta} \tag{4.13}$$

The head h is made up of an elevation head z and a pressure head $p/\rho_f g$:

$$h = z + \frac{p}{\rho_f g} \tag{4.14}$$

Combining Eqs. 4.12-4.14, Darcy's law can be rewritten in a three-dimensional form as:

$$\vec{q} = -\frac{k}{\eta}\vec{\nabla} P \tag{4.15}$$

The continuity equation including an external source Q is given by

$$\frac{\partial \zeta}{\partial t} + \vec{\nabla} \cdot \vec{q} = Q \tag{4.16}$$

Under the assumption that k and h do not vary spatially, then Darcy's law (Eq. 4.15) substituted into the continuity equation (Eq. 4.16) results in a partial differential equation governing fluid flow:

$$\frac{\partial \zeta}{\partial t} - \frac{k}{\eta}\nabla^2 P = Q \tag{4.17}$$

Substituting now Eq. 4.9 into Eq. 4.17 leads to an inhomogeneous diffusion equation for the pore pressure:

$$\frac{\alpha}{K_d B}\left[\frac{B}{3}\frac{\partial \sigma_{kk}}{\partial t} + \frac{\partial P}{\partial t}\right] - \frac{k}{\eta}\nabla^2 P = Q \tag{4.18}$$

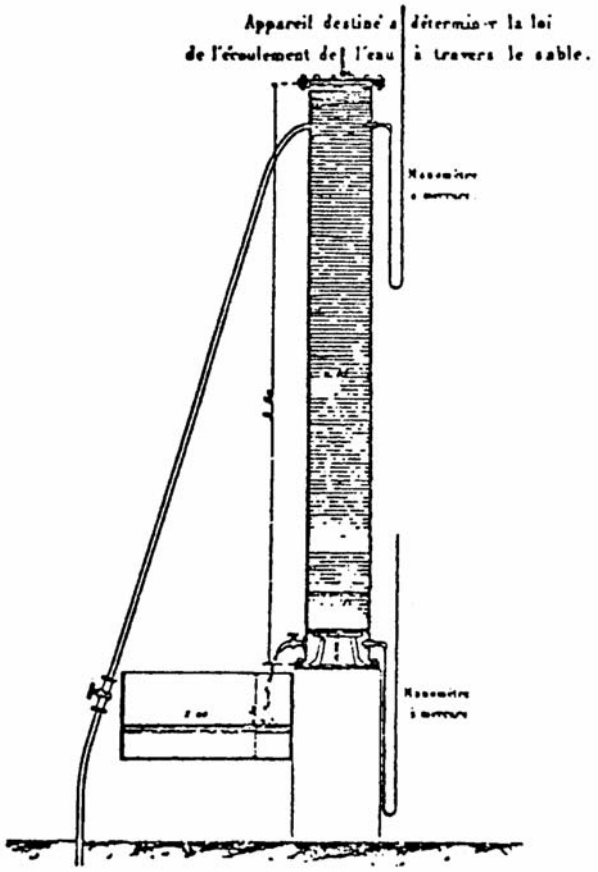

Figure 4-1. Sketch showing the configuration of Darcy's (1856) experiment. Darcy set up a steady state flow through a sand column and measured the pressure difference with manometers and the fluid discharge. Figure after Freeze (1994).

To finally obtain a diffusion equation for the increment of fluid content ζ, Eq. 4.9 is solved for the mean stress $\sigma = \sigma_{kk}/3$ and then substituted into Eqs. 4.18 and

$$\nabla^2\left[\sigma_{kk} + 4\psi P\right] = -\frac{1+\nu}{1-\nu}\vec{\nabla}\cdot\vec{F} \tag{4.19}$$

with the poroelastic stress coefficient ψ, a dimensionless variable defined by Detournay and Cheng (1993):

$$\psi = \frac{1-2\nu}{2(1-\nu)}\alpha \tag{4.20}$$

The two resulting equations are added, what leads to the diffusion equation for ζ:

$$\frac{\partial\zeta}{\partial t} = \frac{k}{\eta S}\nabla^2\zeta + Q + \frac{k}{\eta}\frac{\lambda_u - \lambda}{\alpha(\lambda_u + 2\mu)}F_{k,k} \tag{4.21}$$

The ratio $k/\eta S$ is defined as hydraulic diffusivity c, where S is the uniaxial specific storage. $F_{k,k}$ represents body forces and is defined by $F_{k,k} \equiv \partial F_k/\partial x_k$. λ and μ are the first and second Lamé parameter under drained conditions. μ is equivalent to the shear modulus G; λ can be expressed by μ and the drained bulk modulus K_d:

$$\lambda = K_d - \frac{2\mu}{3} \tag{4.22}$$

λ_u is the first Lamé parameter under undrained conditions and can be expressed by μ and the undrained bulk modulus K_u as:

$$\lambda_u = K_u - \frac{2\mu}{3} \tag{4.23}$$

According to Gassmann (1951) K_u is defined by:

$$K_u = \frac{K_g + K_d\left(\varphi\frac{K_g}{K_f} - \varphi - 1\right)}{1 - \varphi - \frac{K_d}{K_g} + \varphi\frac{K_g}{K_f}} \tag{4.24}$$

where K_g is the bulk modulus of the grains, K_f the bulk modulus of the wetting liquid and φ the porosity. The diffusion equation (Eq. 4.21) is uncoupled from displacement, strain and stress field, and without body forces $\vec{F}$ or fluid sources Q acting, ζ satisfies a homogeneous diffusion equation. Eq. 4.21 can be solved for various problems. In the following the solutions for pore pressure and stress obtained by Rudnicki (1986) are considered.

4.1.1 Continuous point injection into homogeneous full space

Rudnicki (1986) solved the diffusion equation (Eq. 4.21) for the case of continuous fluid injection at one point into infinite homogeneous poroelastic medium, and obtained solutions for the spatio-temporal pore pressure and stress changes:

$$P(x,t) = \frac{\Phi}{\rho_f c}\frac{1}{4\pi r}\left[\frac{(\lambda_u - \lambda)(\lambda + 2\mu)}{\alpha^2(\lambda_u + 2\mu)}\right] erfc\left(\frac{1}{2}\xi\right), \tag{4.25}$$

$$\sigma_{ij}(x,t) = \frac{\Phi}{\rho_f c}\frac{(\lambda_u - \lambda)\mu}{4\pi r c\alpha(\lambda_u + 2\mu)}\left\{\delta_{ij}\left[erfc\left(\frac{1}{2}\xi\right) - \frac{2}{\xi^2}g(\xi)\right] + \left(\frac{x_i x_j}{r^2}\right)\left[erfc\left(\frac{1}{2}\xi\right) + \frac{6}{\xi^2}g(\xi)\right]\right\} \tag{4.26}$$

where the ratio Φ/ρ_f is the injected fluid volume V_{fl} per time [m^3/s], $r = \sqrt{(x_k x_k)}$, and ξ:

$$\xi = \frac{r}{\sqrt{ct}} \tag{4.27}$$

with the diffusivity c [m^2/s] which is given by

$$c = \frac{K(\lambda_u - \lambda)(\lambda + 2\mu)}{\alpha^2(\lambda_u + 2\mu)}. \tag{4.28}$$

K [m^{3}s/kg] is a permeability defined by Rudnicki (1986) as the ratio of permeability k [m^2] divided by the fluid viscosity η [Pa·s]:

$$K = \frac{k}{\eta} \tag{4.29}$$

Solving Eq. 4.13 for k and substituting into Eq. 4.29, K can also expressed by the hydraulic conductivity k_f, the fluid density ρ_f and g:

$$K = \frac{k_f}{\rho_f g} \tag{4.30}$$

The function $g(\xi)$ in Eq. 4.26 is given by

$$g(\xi) = \frac{1}{2\sqrt{\pi}} \int_0^{\xi} s^2 \exp\left(-\frac{1}{4}s^2\right) ds = erf\left(\frac{1}{2}\xi\right) - \frac{\xi}{\sqrt{\pi}} \exp\left(-\frac{1}{4}\xi^2\right). \tag{4.31}$$

The error function erf(z) and the complementary error function erfc(z) (Abramowitz and Stegun, 1965), respectively, used in Eqs. 4.25, 4.26 and 4.31 are $erf(z) = 2\pi^{-1/2} \int_0^z e^{-t^2} dt$ and $erfc(z) = 1 - erf(z)$. As Rudnicki (1986) uses the engineering sign convention (compressive stress < 0, tensional stress > 0), he gives Eq. 4.26 with a negative sign.

By dividing Eq. 4.26 by Eq. 4.25 a spatio-temporal pore pressure stress coupling ratio for the entire stress tensor can be calculated. In chapter 4.1.2 it is shown that for time tending towards infinity this space- and time-dependent ratio is equal to Eq. 3.5, the expression Engelder and Fischer (1994) derived for the pore pressure stress coupling ratio.

4.1.2 Pore pressure stress coupling – Derivation of the long-term limits

a) For radial stresses

The strength of the coupling between pore pressure and stress can be expressed by the ratio of pore pressure change divided by stress change. By substituting Rudnicki's (1986) solutions (Eqs. 4.25 and 4.26) into this ratio, it is shown that, for time tending towards infinity, this ratio results in Eq. 3.5, the time-and space-independent ratio Engelder and Fischer (1994) derived. This can be achieved by substituting Eqs. 4.25, 4.26 into $\Delta\sigma_{ij} / \Delta P$ gives

$$\frac{\Delta\sigma_{ij}(x,t)}{\Delta P(x,t)} = \frac{\alpha\mu}{\lambda + 2\mu} \frac{\delta_{ij}\left[erfc\left(\frac{1}{2}\xi\right) - \frac{2}{\xi^2} g(\xi)\right] + \frac{x_i x_j}{r^2}\left[erfc\left(\frac{1}{2}\xi\right) + \frac{6}{\xi^2} g(\xi)\right]}{erfc\left(\frac{1}{2}\xi\right)} \tag{4.32}$$

In the following the coupling between P and the normal stresses σ_{ii} along the i-axes of a Cartesian coordinate system with origin at the injection point is considered. Those stresses represent the radial stress σ_r. Then for any radial stress σ_r ($i = j$), Eq. 4.32 simplifies to:

$$\frac{\Delta\sigma_r(x,t)}{\Delta P(x,t)} = \frac{2\alpha\mu}{\lambda+2\mu}\left[1+\frac{\frac{2}{\xi^2}g(\xi)}{erfc\left(\frac{1}{2}\xi\right)}\right] \tag{4.33}$$

Only the second summand of Eq. 4.33 has a time- and space-dependent component. Therefore, to determine the so-called long-term limit, the limes for time tending towards infinity, what is equal to $\xi \rightarrow 0$ (Eq. 4.27), only the second summand has to be considered. In Appendix A it is shown that

$$\lim_{t\to\infty}\frac{\frac{2}{\xi^2}g(\xi)}{erfc\left(\frac{1}{2}\xi\right)} = \lim_{\xi\to 0}\frac{\frac{2}{\xi^2}g(\xi)}{erfc\left(\frac{1}{2}\xi\right)} = 0 \tag{4.34}$$

According to Jaeger et al. (2007):

$$\frac{2\mu}{\lambda+2\mu} = \frac{1-2\nu}{1-\nu} \tag{4.35}$$

Applying Eqs. 4.34 and 4.35 to 4.33, then

$$\lim_{t\to\infty}\frac{\Delta\sigma_r(x,t)}{\Delta P(x,t)} = \alpha\frac{1-2\nu}{1-\nu}. \tag{4.36}$$

As the right hand side of Eq. 4.36 is space- and time-independent, it is called long-term limit. It is identical to the solution of Engelder and Fischer (1994) for the minimum horizontal sress (Eq. 3.5). This minimum horizontal stress is a radial stress if the direction along the orientation of the minimum horizontal stress is considered.

b) For tangential stresses

Tangential stress is called a normal stress σ_{ii}, which is observed along the *j*-axis. This taken into account, Eq. 4.32 leads to the spatio-temporal pore pressure stress coupling ratio for tangential stresses:

$$\frac{\Delta\sigma_t(x,t)}{\Delta P(x,t)} = \frac{\alpha\mu}{\lambda+2\mu}\left[1-\frac{\frac{2}{\xi^2}g(\xi)}{erfc\left(\frac{1}{2}\xi\right)}\right] \tag{4.37}$$

The second summand of Eq. 4.37 which has to be taken into consideration for $t \rightarrow \infty$ is the same as for the radial pore pressure stress coupling ratio (Eq. 4.33). Therefore, Eq. 4.34 applies, what is shown in Appendix A. Thus, the limit for t $\rightarrow \infty$ is given by:

$$\lim_{t\to\infty}\frac{\Delta\sigma_t(x,t)}{\Delta P(x,t)} = \alpha\frac{\mu}{\lambda+2\mu} = \frac{1}{2}\alpha\frac{1-2\nu}{1-\nu} = \frac{1}{2}\lim_{t\to\infty}\frac{\Delta\sigma_r(x,t)}{\Delta P(x,t)} \tag{4.38}$$

The long-term limit for tangential stresses is half the long-term limit for radial stresses.

4.2 Analytical investigations

Based on Eqs. 4.25 and 4.26 the spatio-temporal pore pressure and stress changes caused by continuous fluid injection are investigated. Then, with Eq. 4.32 the space- and time-dependent pore pressure stress coupling ratio is calculated for different stress components and compared to each other. In this section a Cartesian coordinate system with the origin at the injection point, the *x*- and *y*-axis pointing in horizontal direction and the *z*-axis in vertical direction, is used (Figure 4-2). The calculated stresses and pore pressure stress coupling ratios are related to this coordinate system.

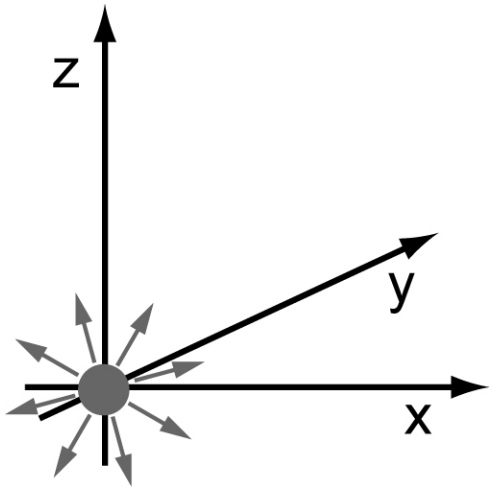

Figure 4-2. Cartesian coordinate system, calculated stresses and pore pressure stress coupling ratios are related to. The origin of the coordinate system is at the injection point.

4.2.1 Spatio-temporal pore pressure, stress and pore pressure stress coupling

In the following the spatial and temporal distribution of fluid injection induced pore pressure variations and changes of all principal stresses are investigated. Furthermore, the coupling between pore pressure and all principal stresses is analysed. Listed in Table 2 are the material parameters used for the pore pressure (Eq. 4.25) and stress calculations (Eq. 4.26), and thus also for the determination of the pore pressure stress coupling ratio.

To show both the spatial as well as the temporal evolution of pore pressure, stress and pore pressure stress coupling ratio, those three variables are plotted a) in dependence of the observation location with respect to the injection point for a fixed injection time *t*, and b) in dependence of injection time for a fixed observation point *r* (last two columns of Table 2).

Table 2. Material parameters used for the calculation of pore pressure and stress changes according to Eqs. 4.25 and 4.26. q/ρ_0 is the injected volume per time, c the diffusivity, λ_u the undrained first Lamé parameter, λ and μ the drained Lamé parameters, and α the Biot-Willis coefficient. t and r give the fixed injection time and location, respectively, for which the spatial and temporal evolution of pore pressure, stress and pore pressure stress coupling ratio is analysed.

Φ/ρ_f [m^3/s]	C [m^2/s]	λ_u [GPa]	λ [GPa]	μ [GPa]	α	t [d]	r [m]
0.05	0.005926	11.2	8.4	8.4	0.65	1000	200

a) P, σ and pore pressure stress coupling ratio depending on location (t = 1000 d)

The spatial distributions of pore pressure, stresses and pore pressure stress coupling ratios are calculated along the x-axis. As no shear stresses are developing along the coordinate axes, normal stresses considered along the coordinate axes are principal stresses. The pore pressure distribution is given by Eq. 4.25. The solution for the stress distribution (Eq. 4.26) depends on whether a radial stress, e.g. σ_{xx} along x-axis, or a tangential stress, e.g. σ_{yy} along x-axis, is calculated. For radial stresses, Eq. 4.26 gives

$$\sigma_r(x,t) = \frac{\Phi}{\rho_f c}\frac{(\lambda_u-\lambda)\mu}{4\pi r c\alpha(\lambda_u+2\mu)}\left[2\cdot erfc\left(\frac{1}{2}\xi\right)+\frac{4}{\xi^2}g(\xi)\right] \tag{4.39}$$

and for tangential stresses:

$$\sigma_t(x,t) = \frac{\Phi}{\rho_f c}\frac{(\lambda_u-\lambda)\mu}{4\pi r c\alpha(\lambda_u+2\mu)}\left[erfc\left(\frac{1}{2}\xi\right)-\frac{2}{\xi^2}g(\xi)\right] \tag{4.40}$$

For a given time since the beginning of injection, pore pressure and stress changes decrease with increasing distance from the injection point. For the chosen parameters, ΔP is higher than $\Delta\sigma_{xx}$ up to a distance of ~1500m For distances larger than 1500 m $\Delta\sigma_{xx}$ is higher than ΔP. Hence, ΔP decreases faster with distance than $\Delta\sigma_{xx}$ (Figure 4-3). This can be explained by the different propagation mechanisms of pore pressure and stress. While a change in pore pressure is diffusing through the pores of a rock matrix, whereas the speed of the diffusion process is strongly dependent on the rock's permeability, a stress change however is transferred immediately via the granular structure of the rock. It can be shown that the intersection radius is depending on the chosen permeability and that it is getting larger for higher permeability.

The change in tangential stress $\Delta\sigma_{yy} = \Delta\sigma_{zz}$ is less than the change in radial stress, and becomes negative before converging zero with increasing distance from the injection source, what is shown in Figure 4-4. This means, close to the injection source tangential stresses are compressive, before they become slightly tensile at larger distances from the injection point.

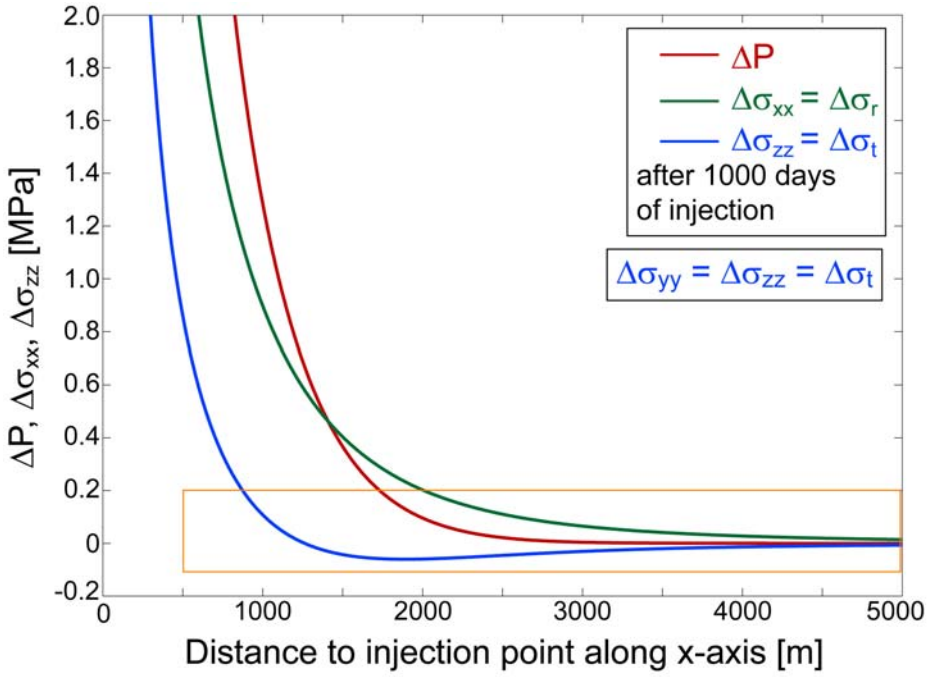

Figure 4-3. Pore pressure and stress changes developed after 1000 days of injection. $\Delta\sigma_{yy}$ and $\Delta\sigma_{zz}$, representing tangential stresses, are equal for observation points along the *x*-axis. The part of the diagram the orange box is enclosing is displayed in more detail in Figure 4-4.

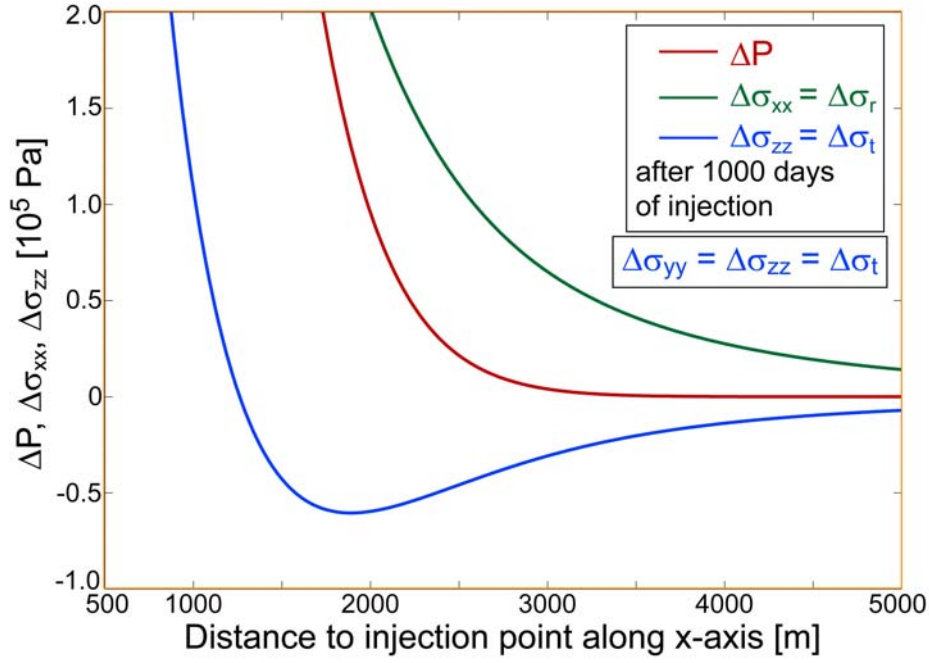

Figure 4-4. Zoom of Figure 4-3 (orange box). Tangential stresses become negative before they converge zero with distance.

Using the results of pore pressure and stress changes shown in Figures 4-3 and 4-4, pore pressure stress coupling ratios $\Delta\sigma_{xx}/\Delta P$ and $\Delta\sigma_{zz}/\Delta P$ are calculated, and the resulting graphs shown in Figure 4-5. Close to the injection point both pore pressure stress

coupling ratios are approaching the constant long-term limits which, according to Engelder and Fischer (1994), are calculated with Eq. 3.5, and plotted as dashed lines. For larger distances both ratios diverge from their long-term limits, $\Delta\sigma_{xx}/\Delta P$ increases, whereas $\Delta\sigma_{zz}/\Delta P$ decreases. This is the consequence of the faster than $\Delta\sigma_{ii}$ towards zero converging pore pressure change (Figure 4-3). Thus, the modulus of the resulting pore pressure stress coupling ratios has to increase with distance, $\Delta\sigma_{xx}/\Delta P$ towards $+\infty$ and $\Delta\sigma_{zz}/\Delta P$ towards $-\infty$, as $\Delta\sigma_{zz}$ becomes negative.

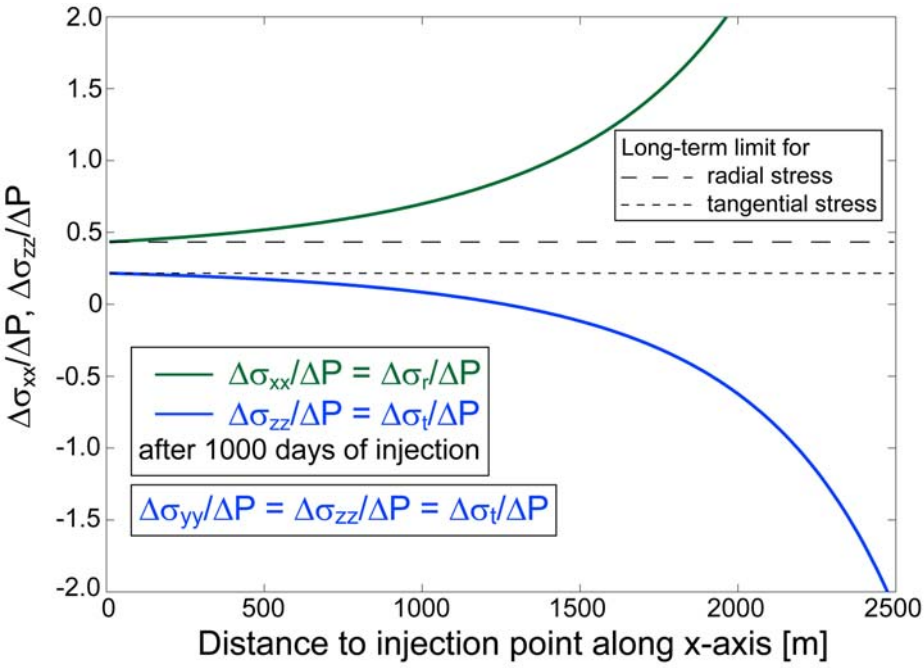

Figure 4-5. Spatial distribution of pore pressure stress coupling for radial stresses (green) and tangential stresses (blue). Dashed lines show the long-term limits for radial and tangential stresses, calculated by Eqs. 4.36 and 4.38 with $\nu = 0.25$ and $\alpha = 0.65$.

The results for $\Delta\sigma_{xx}$ and $\Delta\sigma_{yy} = \Delta\sigma_{zz}$, as well as for $\Delta\sigma_{xx}/\Delta P$ and $\Delta\sigma_{yy}/\Delta P = \Delta\sigma_{zz}/\Delta P$ are exchangeable, depending on the location of the observation point. Considering a point on the z-axis instead of the x-axis, $\Delta\sigma_{zz}$ would be the larger radial stress change, and $\Delta\sigma_{xx}$ and $\Delta\sigma_{yy}$ the smaller tangential stress changes.

b) P, σ and pore pressure stress coupling ratio depending on time (r = 200 m)

After considering pore pressure and stress depending on distance from the injection point, now the temporal evolution of pore pressure, stresses and pore pressure stress coupling ratios is investigated. Figure 4-6 shows the temporal character of pore pressure and stress changes at a distance of $r = x = 200$ m. Immediately after start of injection σ_{xx} and $\sigma_{yy} = \sigma_{zz}$ begin to change at the observation point, whereas for P it takes a few days until ΔP arrives. Again, this is due to the different propagation mechanisms of pore pressure and stress. The stress is spreading out via the granular structure of the rock

matrix; P is diffusing through the pore spaces. So, for short injection times, stress changes are higher than ΔP, that increases stronger than $\Delta\sigma_{xx}$ and $\Delta\sigma_{yy}$. Thus, after 11 days of injection ΔP is higher than the stress changes. The time axis in Figure 4-6 has a logarithmic scale. This is to better display ΔP and the stress changes, as the major part of the changes occur directly after the start of injection. After 1% (100 days) of the considered injection time, about 70% of the total pore pressure and stress changes have occurred.

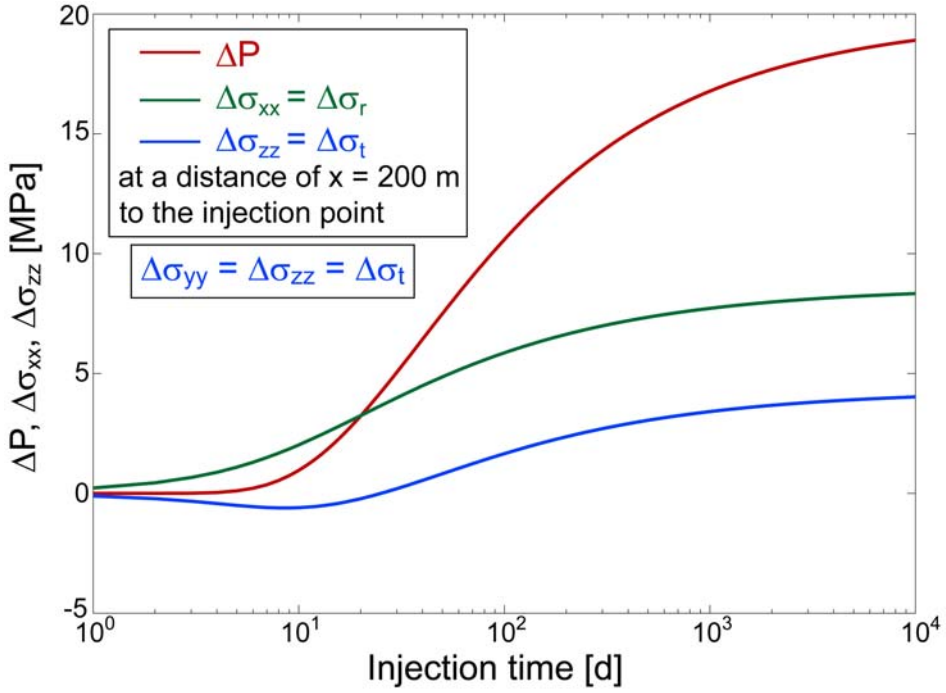

Figure 4-6. Temporal evolution of pore pressure, radial and tangential stress at a distance of x = 200 m from the injection point. Note the logarithmic scale of the time axis, in order to stretch the pore pressure and stress changes, as they mainly have occurred after 100 days of injection.

Because the pore pressure change takes more time than the stress changes to arrive at the observation point, the pore pressure stress coupling ratios $\Delta\sigma_{xx}/\Delta P$ and $\Delta\sigma_{yy}/\Delta P = \Delta\sigma_{zz}/\Delta P$ approach $\pm\infty$ for injection time going towards zero. With increasing injection time and thus increasing ΔP, the pore pressure stress coupling ratios become smaller and converge towards their long-term limits (dashed horizontal lines) for injection times longer than 1000 days (Figure 4-7).

Considering pore pressure and stress changes depending on time (Figure 4-6) together with pore pressure and stress changes depending on distance (Figure 4-3), it is clear that a) the larger the distance from the injection point the longer the injection time after which pore pressure is starting to change, b) the longer the injection time the larger the distance at which ΔP is smaller than $\Delta\sigma_{xx}$, c) the longer the injection time the larger the distance at which the tangential stress change is becoming negative, d) the longer the injection time the smaller the maximal negative change of the tangential stress.

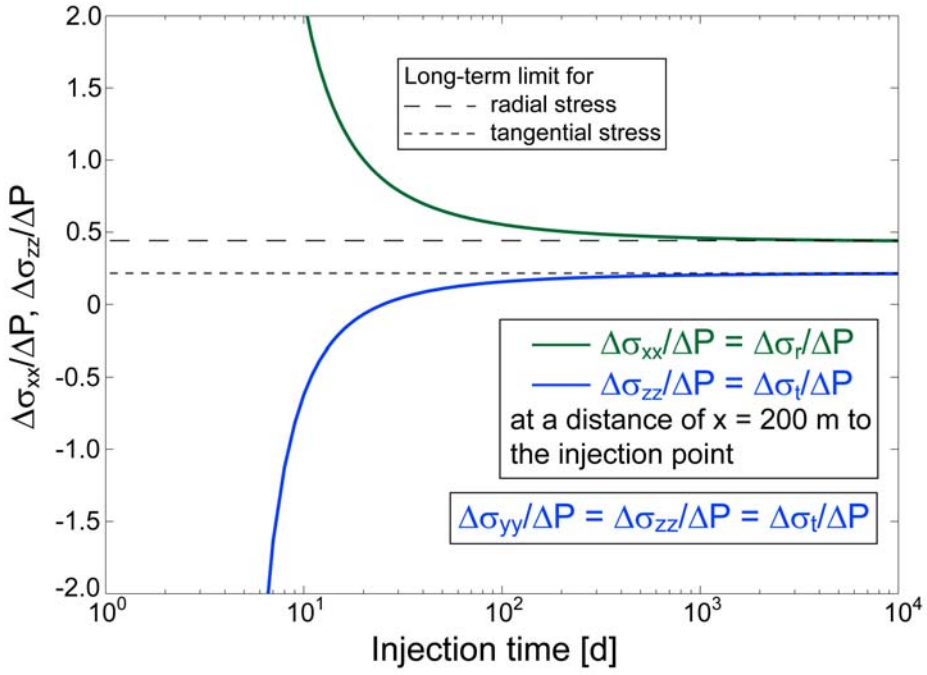

Figure 4-7. Temporal evolution of pore pressure stress coupling for radial stresses (green) and tangential stresses (blue). Dashed lines show the long-term limits of both stresses, calculated according to Eqs. 4.36 and 4.38 with $\nu = 0.25$.

4.2.2 Influence of tectonic regime on rock stability during fluid injection

Taking coupling between pore pressure P and total stress into account, the influence of fluid injection or reservoir depletion, i.e. pore pressure variation, on the state of stress, and thus on rock stability, under consideration of the tectonic regime, has been investigated by various authors. Chen and Nur (1992) calculate the effect of pore pressure change on the effective shear stress. They find that in a normal faulting regime the increase of pore pressure leads to stabilization of the rock, and reduction in pore pressure to destabilization. In the case of a thrust faulting regime, the results for pore pressure build-up and decline exchange. On the contrary, Hillis (2000; 2001; 2003) has shown that pore pressure increase leads to rock stabilization in a normal faulting, taking coupling between P and σ_h, and no coupling between P and σ_V into account. Recently, Soltanzadeh et al. (2009) have published modelling results, showing the effect of pore pressure increase or drawdown in a reservoir on the state of stress and the rock stability, at different locations. Depending on the location pore pressure increase and decrease can lead to both, stabilization and destabilization of the rock.

None of these authors has considered the influence of pore pressure variation on the state of stress depending on both, the tectonic regime as well as the location with respect to the injection/depletion point. Furthermore, a new point is the inclusion of the temporal development of the state of stress with duration of injection. Under these two

aspects, the effect of fluid injection on the state of stress and rock stability is discussed in the following.

According to Eqs. 4.25 and 4.26, fluid injection into poroelastic medium influences the spatio-temporal evolution of both pore pressure and stress, as shown previously. As stresses as well as pore pressure are changing during fluid injection, also the rock stability may be affected by this process. Furthermore, to what extent different tectonic regimes and the location, pore pressure and stress changes are observed at, with respect to the injection point influences the effective stress state is investigated. In the following a Mohr-Coulomb failure criterion (Coulomb, 1776; Engelder, 1993; Mohr, 1882; Parry, 1995) will be used to illustrate the influence of fluid injection on the effective state of stress and thus, how a changing effective stress state is affecting the rock stability.

According to Eqs. 4.25 and 4.26 pore pressure and stress changes with the material parameters provided in Table 2 are calculated at a distance of 200 m to the injection point, which is assumed to be in a depth of z = 3000 m, for three different injection times (14 days, 60 days, 2 years). As the influence of the tectonic regime is investigated, first a fictional effective initial stress state, i.e. $\sigma_{1,eff}$ and $\sigma_{3,eff}$, is generated. It is calculated by the difference of lithostatic and hydrostatic pressure, $\sigma_{V,eff} = (\rho_S - \rho_f)gz$, where ρ_S and ρ_f are the mass densities of the solid rock and the fluid, g is the gravitational acceleration, z is the depth. $\sigma_{V,eff}$ is dependent on depth, so the location of the observation point (on the σ_H or the σ_h-axis (z = 3000 m), or on the σ_V-axis above the injection point (z = 2800 m)) will influence the value of $\sigma_{V,eff}$. In order to calculate reasonable states of stress for these two depths, those variables are chosen to be: ρ_S = 2500 kg/m^3; ρ_f = 1000 kg/m^3; g = 10 m/s^2; z_1 = 3000 m for observation points on the σ_H-axis and the σ_h-axis; z_2 = 2800 m if the observation point is on the σ_V-axis. Then, $\sigma_{V,eff}$ is determined by:

$\boldsymbol{\sigma_{V,eff,1}}$ = 1500 kg/m^3 · 10 m/s^2 · 3000 m = **45 MPa** (observation point on σ_H- or σ_h-axis),

$\boldsymbol{\sigma_{V,eff,2}}$ = 1500 kg/m^3 · 10 m/s^2 · 2800 m = **42 MPa** (observation point on σ_V-axis).

In case of a normal faulting regime, where $\sigma_1 = \sigma_V$ and $\sigma_3 = \sigma_h$, additionally the effective minimum horizontal stress $\sigma_{h,eff}$ has to be determined. For this purpose, σ_h was set to $2\sigma_V/3$: $\sigma_{h,1} = 2\rho_S g z_1/3$ = 50 MPa and $\sigma_{h,2} = 2\rho_S g z_2/3$ = 46.7 MPa Then, $\sigma_{h,eff}$ is results as:

$\boldsymbol{\sigma_{h,eff,1}} = \sigma_{h,1} - \rho_f g z_1$ = 50 MPa - 30 MPa = **20 MPa** (observation point on σ_h-axis),

$\boldsymbol{\sigma_{h,eff,2}} = \sigma_{h,2} - \rho_f g z_2$ = 46.7 MPa - 28 MPa = **18.7 MPa** (observation point on σ_V-axis).

In case of a thrust faulting regime, $\sigma_1 = \sigma_H$ and $\sigma_3 = \sigma_V$, the effective maximum horizontal stress $\sigma_{H,eff}$ has to be determined in addition to $\sigma_{V,eff}$. To do this, σ_H was assumed to be $1.3\sigma_V$: Therefore, $\sigma_{H,1} = 1.3\rho_S g z_1$ = 97.5 MPa and $\sigma_{H,2} = 1.3\rho_S g z_2$ = 91 MPa. Then, $\sigma_{H,eff}$ arises as:

$\boldsymbol{\sigma_{H,eff,1}} = \sigma_{H,1} - \rho_f g z_1$ = 97.5 MPa – 30 MPa = **67.5 MPa** (observation point on σ_H-axis),

$\boldsymbol{\sigma_{H,eff,2}} = \sigma_{H,2} - \rho_f g z_2$ = 91 MPa – 28 MPa = **63.5 MPa** (observation point on σ_V-axis).

In case of a strike slip regime, $\sigma_1 = \sigma_H$ and $\sigma_3 = \sigma_h$, the maximum horizontal stress $\sigma_{H,eff}$ is assumed to be $1.2\sigma_V$, hence $\sigma_H = 1.2\rho_S g z_1 = 90$ MPa Then, for the effective maximum horizontal stress follows:

$\boldsymbol{\sigma_{H,eff}} = \sigma_H - \rho_f g z_1 = 90$ MPa - 30 MPa = **60 MPa**.

Similarly, σ_h is assumed to be $0.8\sigma_V$, i.e. $\sigma_h = 0.8\rho_S g z_1 = 60$ MPa. Thus, the effective minimum horizontal stress is given by:

$\boldsymbol{\sigma_{h,eff}} = \sigma_h - \rho_f g z_1 = 60$ MPa - 30 MPa = **30 MPa**.

Based on those effective initial stress fields, pore pressure and stress changes are calculated due to fluid injection, and the effect on rock stability is investigated. For this purpose, a Mohr-Coulomb failure criterion is defined with a cohesion $C = 5$ MPa, and an angle of internal friction of $\delta = 25°$. In total six scenarios, taking the tectonic regime and the observation location with respect to the injection source into account, are considered.

a) *Normal faulting regime, observation point on σ_V-axis*

A normal faulting regime is characterized by $\sigma_V > \sigma_H > \sigma_h$, i.e. $\sigma_1 = \sigma_V$ and $\sigma_3 = \sigma_h$. The observation point located on the σ_V-axis means that σ_V is a radial stress, and therefore changes in σ_V are calculated by Eq. 4.39. With the observation point on the σ_V-axis, σ_h then is a tangential stress and thus, a change in σ_h is calculated by Eq. 4.40. The resulting stress and pore pressure changes for injection times of 14 days, 60 days and 2 years, are listed in Table 3. The temporal evolution of the effective state of stress, caused by fluid injection, in a normal faulting regime with the observation point on the σ_V-axis is shown in Figure 4-8.

Table 3. Pore pressure and stress changes according to Eqs. 4.25, 4.39 and 4.40, with an observation point at $r = 200$ m on the σ_V-axis in a normal faulting regime, for three injection times.

Injection time	ΔP [MPa]	$\Delta\sigma_r = \Delta\sigma_V = \Delta\sigma_1$ [MPa]	$\Delta\sigma_t = \Delta\sigma_h = \Delta\sigma_3$ [MPa]
14 days	1.89	2.59	-0.48
60 days	8.35	5.15	1.05
2 years	16.26	7.57	3.26

Fluid injection influences the effective state of stress in two ways. On the one hand, fluid injection increases the pore pressure, what leads to smaller effective stresses and causes the Mohr circle to move to the left. On the other hand, under consideration of pore pressures stress coupling, fluid injection increases also the total stresses. As the observation point is on the σ_V-axis, σ_V is the radial stress and is increased more than the tangential stress σ_h. Together with the uniform pore pressure increase follows that $\sigma_{V,eff}$ is decreasing less than $\sigma_{h,eff}$, or even increases for short injection times, what leads to an increasing effective differential stress $\sigma_{V,eff} - \sigma_{h,eff}$ and to an increase in the Mohr circle's diameter, respectively. Hence, for this constellation fluid injection brings rock closer to

failure, and this process is amplified by the mechanism of pore pressure stress coupling which is affecting different stress components differently strong. Compared with the classical concept of uncoupled stresses (Terzaghi, 1943) (dashed lines in Figure 4-8), it will take less time to cause failure.

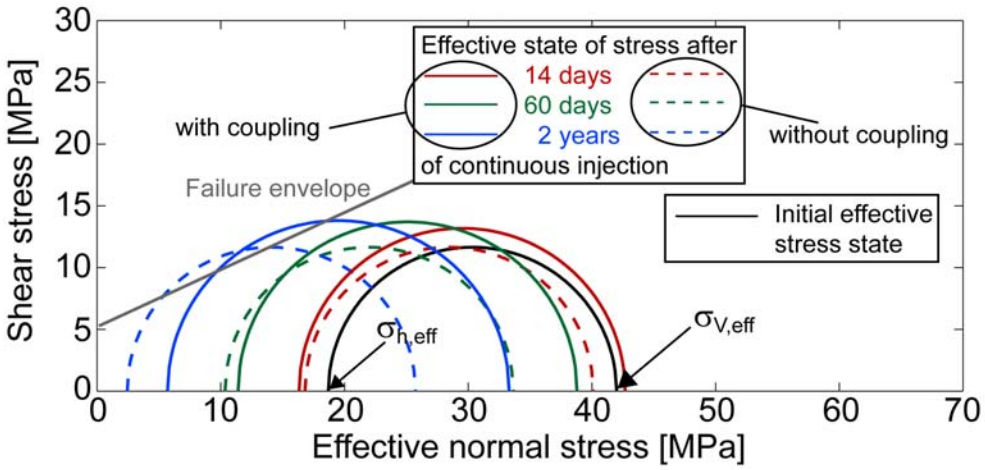

Figure 4-8. Temporal evolution of the effective state of stress in a normal faulting regime with the observation point on the σ_V-axis. Pore pressure stress coupling causes increasing Mohr circles (solid lines) compared to those without coupling (dashed lines). With duration of injection Mohr circles move to the left towards the failure envelope.

b) Normal faulting regime, observation point on σ_h-axis

Now the observation point is considered to be on the σ_h-axis. Thus, σ_h is the radial stress and σ_V the tangential one. Accordingly, the changes in pore pressure and stresses are provided in Table 4. Determining the failure linear line with $C = 5$ MPa and $\varphi = 25°$, the temporal evolution of the effective state of stress for an observation point on the σ_h-axis in a normal faulting regime is shown in Figure 4-9.

Table 4. Pore pressure and stress changes according to Eqs. 4.25, 4.39 and 4.40, with an observation point at $r = 200$ m on the σ_h-axis in a normal faulting regime, for three injection times.

Injection time	ΔP [MPa]	$\Delta\sigma_r = \Delta\sigma_h = \Delta\sigma_3$ [MPa]	$\Delta\sigma_t = \Delta\sigma_V = \Delta\sigma_1$ [MPa]
14 days	1.89	2.59	-0.48
60 days	8.35	5.15	1.05
2 years	16.26	7.57	3.26

Considering an observation point on the σ_h-axis instead of on the σ_V-axis in a normal faulting regime, fluid injection influences the effective state of stress in a different way. σ_h is the radial stress, σ_V the tangential stress, i.e. according to Eqs. 4.39 and 4.40, σ_h increases more than σ_V. Therefore, $\sigma_{V,eff}$ decreases stronger than $\sigma_{h,eff}$, that even can increase for short injection times, i.e. the effective differential stress and thus the Mohr

circle's diameter decreases. As pore pressure is increasing more than the total stresses with duration of injection, the smaller becoming Mohr circles are moving to the left towards the failure envelope (Figure 4-9). Summarizing, with an observation point on the σ_h-axis in a normal faulting regime, fluid injection brings rock closer to failure, but this effect is weakened by the different strong coupling mechanisms between pore pressure and radial and tangential stress. This is slowing down the process of rock destabilization compared to the situation of uncoupled total stresses (dashed lines).

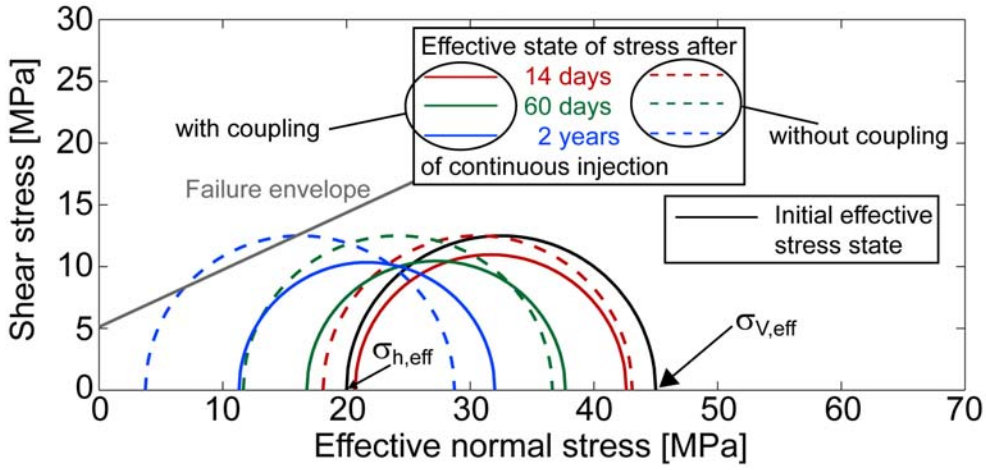

Figure 4-9. Temporal evolution of the effective state of stress in a normal faulting regime with the observation point on the σ_h-axis. Fluid injection causes Mohr circles to move towards the failure envelope. Pore pressure stress coupling is slowing down the process that rock comes closer to failure (solid lines) compared with the case of uncoupled total stresses (dashed lines).

c) Thrust faulting regime, observation point on σ_H-axis

Considering now a thrust faulting regime, i.e. $\sigma_H > \sigma_h > \sigma_V$, and an observation point on the σ_H-axis. This means that σ_H is the radial stress and σ_V the tangential stress. The calculated pore pressure and stress changes are provided in Table 5, the results showing the temporal evolution of the effective state of stress during fluid injection are shown in Figure 4-10.

Table 5. Pore pressure and stress changes according to Eqs. 4.25, 4.39 and 4.40, with an observation point at r = 200 m on the σ_H-axis in a thrust faulting regime, for three injection times.

Injection time	ΔP [MPa]	$\Delta\sigma_r = \Delta\sigma_H = \Delta\sigma_1$ [MPa]	$\Delta\sigma_t = \Delta\sigma_V = \Delta\sigma_3$ [MPa]
14 days	1.89	2.59	-0.48
60 days	8.35	5.15	1.05
2 years	16.26	7.57	3.26

With the observation point on the σ_H-axis, σ_H is the radial stress and increases more than the tangential stress σ_V. Therefore, $\sigma_{V,eff}$ is decreasing more than $\sigma_{H,eff}$, that even can increase for short injection times. The consequence is an increase in effective differential stress $\sigma_{H,eff}$ - $\sigma_{V,eff}$, and thus larger Mohr circles. Due to the fact that pore pressure increases stronger than the total stresses with duration of injection, leads to decreasing effective stresses and thus to Mohr circles shifting to the left towards the failure envelope (Figure 4-10). Considering points along the σ_H-axis in a thrust faulting regime, this process of bringing rock closer to failure is amplified by pore pressure stress coupling affecting the total stresses differently strong that diameter of the Mohr circle increases.

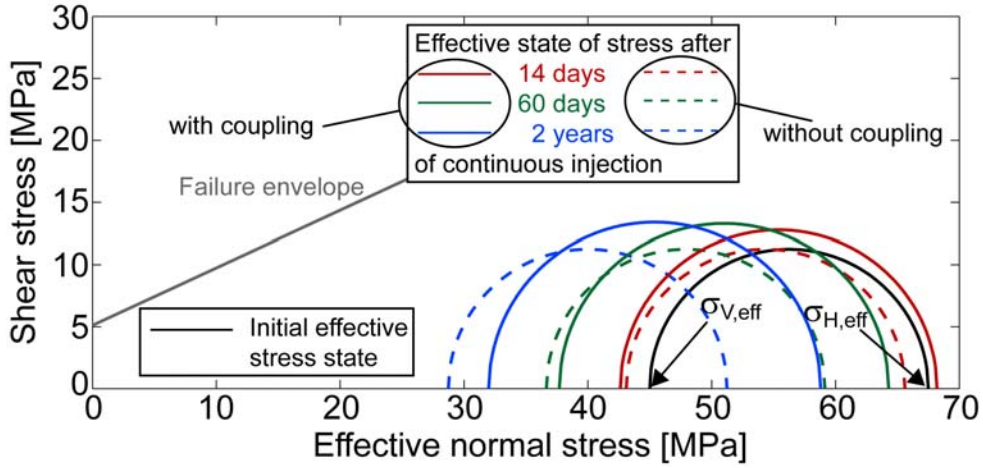

Figure 4-10. Temporal evolution of the effective state of stress in a thrust faulting regime with the observation point on the σ_H-axis. Under consideration of pore pressure stress coupling Mohr circles' diameter increase (solid lines) with duration of injection compared to the uncoupled case with constant Mohr circle diameters (dashed lines).

d) Thrust faulting regime, observation point on σ_V-axis

Considering observation points along the σ_V-axis, stress states are calculated at, then in a thrust faulting regime σ_V represents a radial stress and σ_H a tangential stress. Under these conditions, the resulting pore pressure and stress changes caused by fluid injection are listed in Table 6, and the temporal variation of the effective state of stress is illustrated in Figure 4-11.

If the observation point is located on the σ_V-axis in a thrust faulting regime, the radial stress σ_V increases more than the tangential stress σ_H. This leads to less decreasing $\sigma_{V,eff}$ compared to $\sigma_{H,eff}$, what results in reduction of effective differential stress $\sigma_{H,eff}$ - $\sigma_{V,eff}$ and to smaller Mohr circles, respectively (Figure 4-11). Hence, the different strong coupling between P and the radial and tangential stresses σ_V and σ_H weakens the effect that rock is brought closer to failure with duration of injection.

Table 6. Pore pressure and stress changes according to Eqs. 4.25, 4.39 and 4.40, with an observation point at r = 200 m on the σ_V-axis in a thrust faulting regime, for three injection times.

Injection time	ΔP [MPa]	$\Delta\sigma_r = \Delta\sigma_V = \Delta\sigma_3$ [MPa]	$\Delta\sigma_t = \Delta\sigma_H = \Delta\sigma_1$ [MPa]
14 days	1.89	2.59	-0.48
60 days	8.35	5.15	1.05
2 years	16.26	7.57	3.26

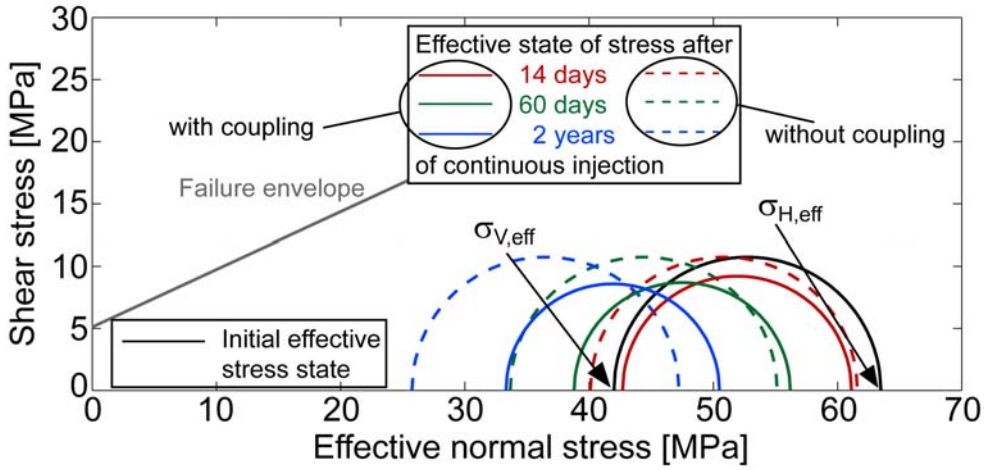

Figure 4-11. Temporal evolution of effective stress state in a thrust faulting regime, with the observation point on the σ_V-axis. Pore pressure stress coupling leads to decreasing differential stress (solid lines), whereas in the uncoupled case the differential stress is constant (dashed lines).

e) Strike-slip regime, observation point on σ_H-axis

A strike-slip regime is defined by $\sigma_H > \sigma_V > \sigma_h$, and considering an observation point on the σ_H-axis means that σ_H is the radial stress and σ_h the tangential one. Therefore, the pore pressure and stress changes at a point on the σ_H-axis with a distance of 200 m from the injection point are given in Table 7. The temporal evolution of the effective state of stress, and thus the effect on rock stability is shown by means of a Mohr diagram (Figure 4-12).

Fluid injection and thus increasing pore pressure leads to a reduction of the effective stresses, and causes the Mohr circle moving to the left. With an observation point on the σ_H-axis, the radial stress σ_H is stronger affected by the fluid injection than the tangential stress σ_h, and increases more than σ_h. Therefore $\sigma_{H,eff}$ is decreasing less than $\sigma_{h,eff}$, what leads to an increase of the effective differential stress, and thus of the diameter of the Mohr circle. Hence, the effect of destabilisation during fluid injection in a strike-slip regime is amplified by the effect of increasing effective differential stress caused by pore pressure stress coupling, if a point on the σ_H-axis is considered. In this case rock is

brought faster to failure than in the case without considering coupling between pore pressure and stress.

Table 7. Pore pressure and stress changes according to Eqs. 4.25, 4.39 and 4.40, with an observation point at r = 200 m on the σ_H-axis in a strike-slip regime, for three injection times.

Injection time	ΔP [MPa]	$\Delta\sigma_r = \Delta\sigma_H = \Delta\sigma_1$ [MPa]	$\Delta\sigma_t = \Delta\sigma_h = \Delta\sigma_3$ [MPa]
14 days	1.89	2.59	-0.48
60 days	8.35	5.15	1.05
2 years	16.26	7.57	3.26

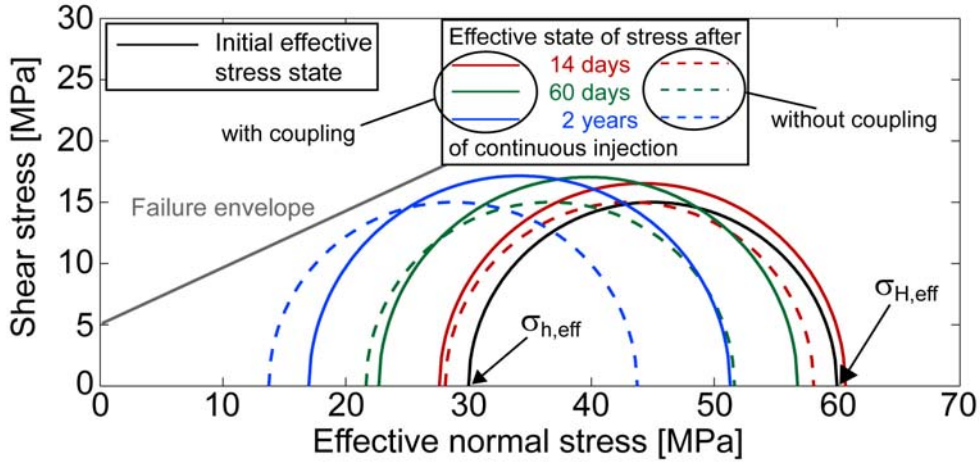

Figure 4-12. Temporal evolution of effective stress state in a strike-slip regime, with the observation point on the σ_H-axis. Fluid injection leads Mohr circles to move to the left towards the failure envelope with increasing differential stress (solid lines) in the case of coupling, and with constant differential stress (dashed lines) without coupling.

f) Strike-slip regime, observation point on σ_h-axis

If the observation point is located on the σ_h-axis, σ_h is the radial and σ_H the tangential stress. Table 8 provides pore pressure and stress changes for this setting. Figure 4-13 illustrates the temporal development of the effective state of stress induced by fluid injection.

Table 8. Pore pressure and stress changes according to Eqs. 4.25, 4.39 and 4.40, with an observation point at r = 200 m on the σ_h-axis in a strike-slip regime, for three injection times.

Injection time	ΔP [MPa]	$\Delta\sigma_r = \Delta\sigma_h = \Delta\sigma_3$ [MPa]	$\Delta\sigma_t = \Delta\sigma_H = \Delta\sigma_1$ [MPa]
14 days	1.89	2.59	-0.48
60 days	8.35	5.15	1.05
2 years	16.26	7.57	3.26

As σ_h is the radial stress, it is affected stronger by fluid injection than the tangential stress σ_H. Therefore, during fluid injection σ_h increases more than σ_H. This leads to a less decreasing $\sigma_{h,eff}$ compared to $\sigma_{H,eff}$. The consequence is a decrease in the effective differential stress, what is equivalent with a decreasing size of the Mohr circle. This stabilisation effect caused by the different coupling between P–σ_H and P–σ_h superposes the destabilisation effect of the increasing pore pressure caused by fluid injection, what is shifting the Mohr circle to the left towards the failure envelope. Thus, in total it takes more time to bring the rock to failure than for pore pressure stress coupling not taken into account.

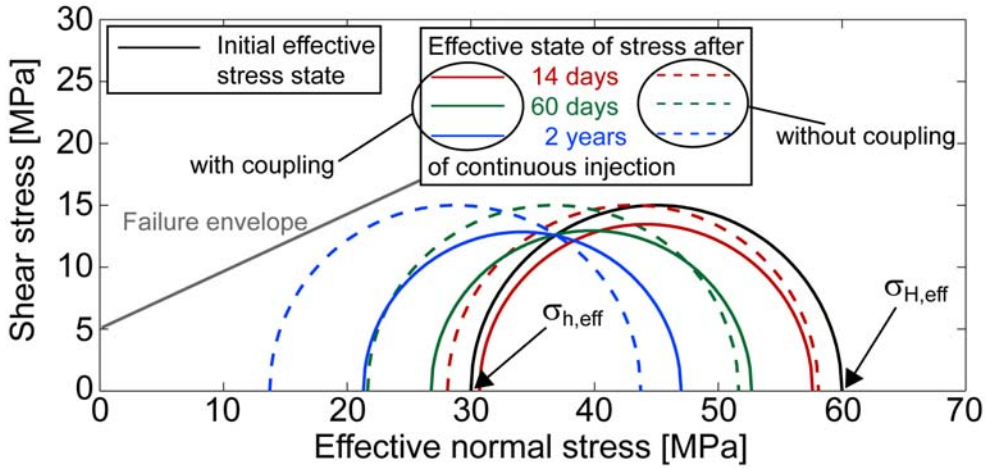

Figure 4-13. Temporal evolution of effective stress state in a strike-slip regime, with the observation point on the σ_h-axis. With duration of injection, pore pressure stress coupling leads to smaller Mohr circles (solid lines) compared to Mohr circles no coupling is considered (dashed lines).

4.2.3 Influence of tectonic regime on rock stability during fluid depletion

The examples above show the influence of fluid injection on the state of stress under consideration of pore pressure stress coupling. Also during fluid depletion the coupling between pore pressure and stresses can be analysed. Fluid depletion influences the stresses in the same way as fluid injection does, but with an opposite sign. Therefore, only a short summary about fluid flow induced stress changes during fluid depletion in combination with the presence of different tectonic stress regimes is provided here.

a) Normal faulting regime

In direction of the maximum principal stress σ_V, σ_V is radial stress and therefore will decrease more than the minimum principal stress σ_h during fluid depletion. Then the differential stress decreases what leads to smaller Mohr circles. For points along the σ_h-axis, σ_V and σ_h are affected in the opposite way. σ_h is decreasing more than σ_V, what leads to an increase in differential stress and thus to larger Mohr circles.

b) Thrust faulting regime

Fluid depletion induced stress changes in direction of the maximum principal stress σ_H affects σ_H more then the tangential stress σ_V. Therefore σ_H decreases more than σ_V does, what leads to a decrease in differential stress and smaller Mohr circles. Considering the effects of fluid depletion on the minimum principal stress axis σ_V, σ_V is radial stress and therefore affected more then the tangential stress σ_H. σ_V decreases more than σ_H, leading to higher differential stresses and larger Mohr circles.

c) Strike-slip regime

In a strike-slip regime maximum and minimum principal stresses are given by σ_H and σ_h. Along the σ_H-axis, σ_H is radial stress and σ_h tangential stress. Therefore, the coupling between pore pressure and σ_H is stronger than between pore pressure and σ_h. Under depletion and pore pressure reduction σ_H decreases more than σ_h. The consequence is a decreasing differential stress and smaller Mohr circles. In σ_h-direction, σ_h (now radial stress) is affected stronger by pore pressure stress coupling than σ_H (now tangential stress), what leads to an increase in differential stress and larger Mohr circles.

4.2.4 Interpretation and discussion

The effects of both fluid injection and depletion on the state of stress in different tectonic regimes show that due to different coupling between pore pressure and the radial stress or the tangential stress the temporal evolution of the effective state of stress during fluid injection or depletion depends on the location, the stresses are calculated at, with respect to the injection point as well as on the tectonic regime. The process, that rock comes closer to failure, caused by fluid injection and pore pressure increase (without process of different coupling mechanisms) is

- amplified in a normal faulting regime at observation points along the σ_V-axis, in a thrust faulting regime at observation points along the σ_H-axis, and in a strike-slip regime at observation point along the σ_H-axis due to an increase in differential stress.
- weakened in a normal faulting regime at observation points along the σ_h-axis, in a thrust faulting regime at observation points along the σ_V-axis, and in a strike-slip regime at observation point along the σ_h-axis due to a decrease in differential stress.

This occurs due to different coupling mechanisms between pore pressure and radial or tangential stress. For fluid depletion the same results can be found. Without coupling, fluid depletion and pore pressure reduction causes the effective stresses to increase, and thus the Mohr circle to move to the right away from the failure envelope. This effect is again

- amplified in a normal faulting regime along the σ_V-axis, in a thrust faulting regime along the σ_H-axis, in a strike-slip regime along the σ_H-axis due an increase in differential stress.
- weakened in a normal faulting regime the σ_h-axis, in a thrust faulting regime along the σ_V-axis, in a strike-slip regime along the σ_h-axis due to a decrease in differential stress.

In summary, independent of the present regime, along the maximum principal stress axis an amplification is taking place. This means, along the σ_1-axis rock comes faster to failure than without coupling due to fluid injection induced increase of differential stress. Fluid depletion increases the effective stresses and rock becomes more stable, what is amplified by decreasing differential stresses. However, along the σ_3-axis, pore pressure stress coupling counteracts the effects of decreasing (increasing) effective stresses during fluid injection (depletion), and thus destabilization (stabilization) of the rock. Depending on the initial state of stress and the initial vicinity of the failure envelope, along the σ_3-axis it is most likely to observe depletion induced failure due to poroelastic coupling.

In the examples of the previous chapter my intention was to highlight the effect of the different strong coupling between pore pressure and different stress components along the same direction. For this reason, I only have considered stress changes along the maximum and minimum principal stress axes. Along the medium principal stress axis both maximum and minimum principal stresses are tangential stresses and therefore would experience the same strength of coupling. In consequence, the differential stress and thus the size of the Mohr circle would be constant. Anyway, pore pressure and stresses are coupled, so that the effective stresses change differently from effective stresses considered without any coupling (Figure 4-14).

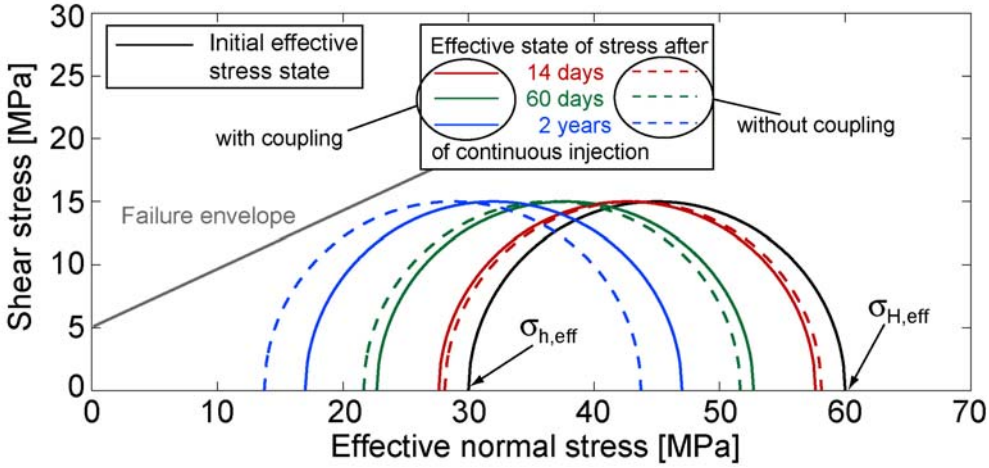

Figure 4-14. Comparison of coupled (solid Mohr circles) and uncoupled (dashed Mohr circles) effective stress changes due to fluid injection. The results are calculated along the σ_V-axis of a strike-slip regime.

During fluid injection pore pressure stress coupling increases the total stresses. Therefore, the effective stresses following from coupled stresses are larger then the effective stresses calculated without pore pressure stress coupling. Considering the poroelastic coupling between pore pressure and effective stress changes, one has to keep in mind the difference between coupled and uncoupled effective stress changes, even if the differential stress is constant.

Especially in the case, where the observation point is on the σ_3-axis and thus the differential stress is reduced by pore pressure stress coupling, is the difference between the effective stress states with coupling (solid Mohr circles) and without coupling (dashed Mohr circles) quite considerable and increases with duration of injection (Figures 4-9, 4-11, 4-13). Is the observation point on the σ_1-axis and pore pressure stress coupling leads to increasing differential stress and Mohr circles during fluid injection, the effect of pore pressure stress coupling regarding the rock stability is strongest for short injection times (Figures 4-8, 4-10, 4-12). If rock is in a critical state of stress before start of injection, i.e. close to failure, pore pressure stress coupling leads after start of injection to failure if the observation point is on the σ_1-axis, or prevents failure if the observation point is on the σ_3-axis, both compared to the uncoupled case (Figure 4-15). Hence, if rock is critically stressed, pore pressure stress coupling influences considerably the rock stability already for short injection times, when a significant stress change reached the observation point, but not yet the slower diffusing pore pressure.

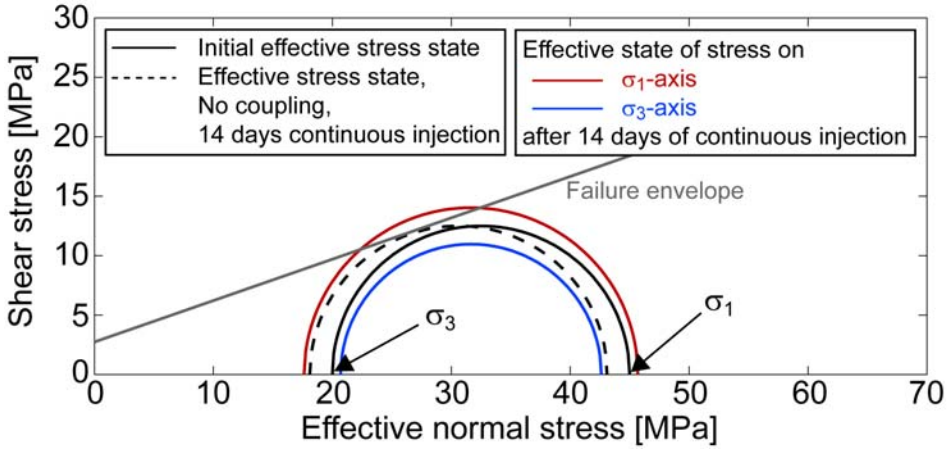

Figure 4-15. Effect of pore pressure stress coupling on the effective stress states for a point on the σ_1-axis (red Mohr circle) and a point on the σ_3-axis (blue Mohr circle) after a short injection time of 14 days, compared to the effective state of stress without pore pressure stress coupling (dashed Mohr circle).

Considering only 14 days of injection, the results Chen and Nur (1992) and Hillis (2000; 2001; 2003) found, can be validated. In Chen and Nur (1992) pore pressure increase leads to rock stabilization in a thrust faulting regime. Figure 4-11 (red Mohr circle) shows the same effect. Similarly, pore pressure increase leads to rock

destabilization in a normal faulting regime (Figure 4-8, red Mohr circle). In both cases the location of the observation point is on the σ_V-axis. Rock stabilization in a normal faulting regime due to pore pressure increase (Hillis, 2000; 2001; 2003) can be observed if the observation point is on the σ_h-axis (Figure 4-9, red Mohr circle).

Therefore, it is essential to consider both, the tectonic regime and the location at which the stresses are calculated, as those two effects are acting contrary. Not less important is the inclusion of the temporal aspect. An effect of stabilization during fluid injection (Hillis, 2000; 2001; 2003) is taking place if the observation point is on the σ_3-axis, independent of the tectonic regime (Figures 4-9, 4-11, 4-13). With duration of injection the effect of reduction of effective stress due to pore pressure increase exceeds the effect of stress increase due to pore pressure stress coupling. Therefore, for longer injection times fluid injection will always cause failure, but this is delayed in time by pore pressure stress coupling.

Another characteristic concerning the change of the Mohr circles' diameter with duration of injection can be seen in Figures 4-8 – 4-13 independent of the tectonic regime and the observation location. Due to different strong coupling between P and the radial and tangential stress, the effective differential stress or the size of the Mohr circle changes after start of injection, not anymore after longer injection times. This behaviour can be made clear by looking at the gradients of pore pressure and stress changes, $d\Delta P/dt$, $d\Delta\sigma_r/dt$, $d\Delta\sigma_t/dt$, this means how pore pressure and stress changes vary with time, what is shown in Figure 4-16 and in more detail in Figure 4-17.

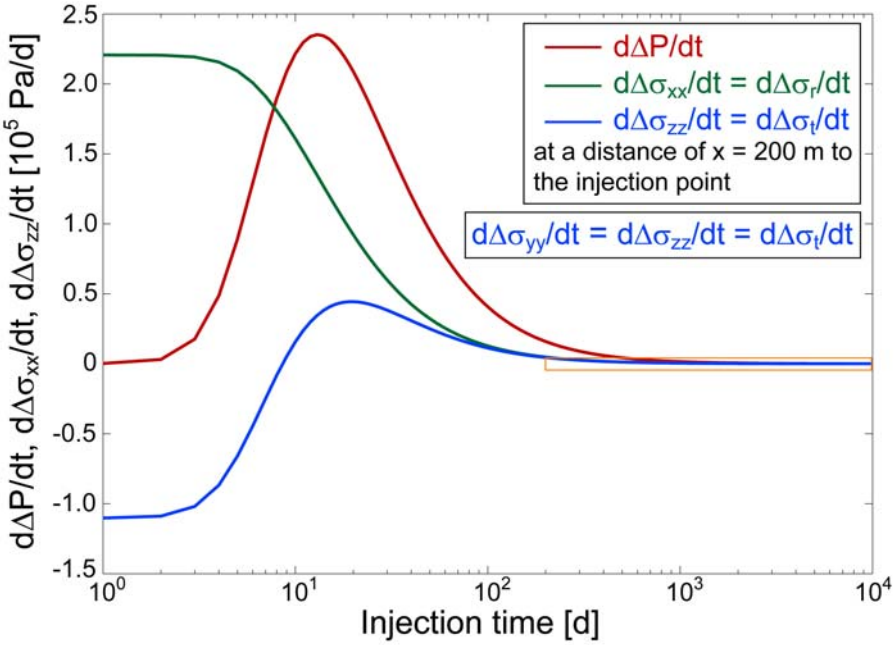

Figure 4-16. Gradients of pore pressure and stress changes. After start of injection stresses change maximal, whereas the gradient of pore pressure change is maximal after 10 days of injection due to diffusion process pore pressure is propagating with. Detail of orange box is shown in Figure 4-17.

As expected, directly after start of injection the stress changes, spreading out immediately via the solid rock structure, are maximal, the pore pressure change, diffusing through the pore spaces, is zero. With duration of injection the stresses change less, the gradient of pore pressure change reaches a maximum after 10 days before it declines again. Please note that both stress components (radial and tangential) change at the same rate after a few hundred days of injection. This means necessarily that also the maximum and the minimum effective stress is changing at the same amount, and therefore, the effective differential stress doesn't change and the size of the Mohr circle is constant, what can be seen in Figures 4-8 – 4-13 for long injection times.

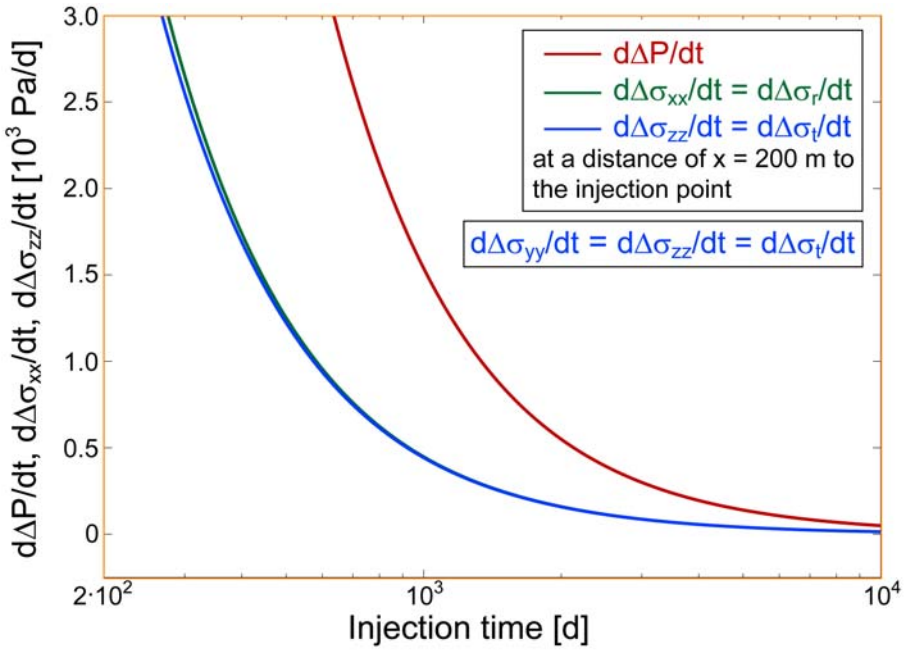

Figure 4-17. Radial ($\Delta\sigma_{xx}$) as well as tangential stresses ($\Delta\sigma_{yy}$, $\Delta\sigma_{zz}$) are changing at the same rate after a few hundred days of injection. The consequence is a constant effective differential stress or a constant Mohr circle size, respectively (Figures 4-8 – 4-13).

Even if the effective differential stress is constant after certain injection time, and thus with duration of injection the Mohr circle is moving to the left with a constant diameter, this does not mean that it behaves like in the case of Terzaghi's (1943) concept of effective stresses (Figure 1-1). Due to the coupling between pore pressure and stress, the total stresses increase (decrease) during injection (depletion), and therefore the effective stresses decrease (increase) less than in the case of uncoupled stresses.

Rudnicki's (1986) solutions (Eqs. 4.25 and 4.26) can be used to investigate the spatio-temporal character of pore pressure and stress due to fluid injection in poroelastic medium. Also the influence on the rock stability in dependence on the tectonic regime and on the location, pore pressure and stress is calculated at, with respect to the injection point, can be analysed with duration of injection.

The next step is to extend the calculation of pore pressure and stress to a medium which represents the setting of a reservoir embedded in surrounding of different material properties. As Eqs. 4.25 and 4.26 are limited to a homogeneous infinite poroelastic full space, and also no other analytical solution exists which describes the effect of fluid injection on the spatio-temporal distribution of pore pressure and stress in an inhomogeneous poroelastic medium, numerical modelling is used to calculate the spatio-temporal pore pressure and stress distribution.

5 Numerical Approach

The approach of numerical modelling enables to calculate pore pressure and stress distributions inside a poroelastic volume containing inhomogeneities and complex geometries that cannot be described by analytical solutions. Such numerical models simulate the stress and pore pressure distributions in realistic geometries better than the analytical solution for an infinite homogeneous poroelastic full space (Rudnicki, 1986), and can be used to model the pore pressure and stress distribution inside and around a reservoir. Using the approach of numerical modelling, and thus the possibility to create models containing inhomogeneities, the influence of inhomogeneous material on the pore pressure and stress distribution can be investigated. In this thesis the finite element method is used to solve the resulting coupled partial differential equations within the model volume.

5.1 Effective stress in Abaqus

ABAQUS uses a generalised form of Terzaghi's (1943) principle to calculate the effective state of stress. According to ABAQUS Documentation (2008) the effective state of stress is given by

$$\sigma_{eff} = \sigma + \left(\chi u_w + (1-\chi)u_a\right)I \tag{5.1}$$

where χ stands for the saturation of the system, u_w is the average pressure stress in the wetting liquid, u_a the average pressure stress in the other fluid (in unsaturated cases), and I is the unit matrix. In fully saturated systems, which are considered here, $\chi = 1$, and Equation 5.1 simplifies to

$$\sigma_{eff} = \sigma + u_w I \tag{5.2}$$

which is identical with the effective state of stress described by Terzaghi (1943) (Eq. 3.1). The different signs result from different sign conventions. ABAQUS uses the engineering sign convention with compressive stresses to be negative.

5.2 Input-parameters for poroelastic modelling

Using the commercial software package ABAQUS as solver for the resulting partial differential equations, a set of input-parameters is required to be specified by the user. For the modelling of pore pressure and stress induced by fluid flow in poroelastic medium the parameter set is given by:

- Mass density ρ_S [kg/m^3]
- Bulk modulus of solid grains K_g [Pa]
- Bulk modulus of fluid K_f [Pa]
- Specific weight of the wetting liquid $\rho_f g$ [kg/m^{2}s^2]
- Hydraulic conductivity k_f [m/s]

- Void ratio e [1]
- Logarithmic bulk modulus κ [1]
- Poisson's ratio ν [1]
- Injection rate V_{fl} [m^3/s]

Most of the above parameters are well-known. Only the logarithmic bulk modulus κ should be explained in more detail, as it is a special ABAQUS variable. According to ABAQUS Documentation (2008), the elastic part of the volume ratio between the current and a reference state, J^{el}, is defined as

$$J^{el} = \frac{\kappa}{1+e_0} \ln\left(\frac{p_0 + p_t^{el}}{p + p_t^{el}}\right) + 1 \tag{5.3}$$

where κ is the logarithmic bulk modulus, e_0 the initial void ratio, p and p_0 are the mean and the initial mean stress, and p_t^{el} is the elastic tensile limit. Under the assumptions $p_t^{el} >> p_0$ and $p_t^{el} >> p$, κ can be expressed in terms of e_0, p, p_t^{el} and the drained bulk modulus K_d:

$$\kappa = \frac{1+e_0}{K_d}\left(p + p_t^{el}\right) \tag{5.4}$$

The derivation of Eq. 5.4 as well as the transformation of the above given parameter set into the parameter set (μ, λ, λ_u, α, c) used by Rudnicki (1986) and in Eqs. 4.25 and 4.26 is shown in Appendix B.

5.3 Homogeneous axis-symmetric model

At first a finite element model with homogeneous poroelastic rheology was set up in order to compare the model results with the results achieved from Rudnicki's (1986) analytical solutions (Eqs. 4.25 and 4.26). This comparison also enables to check whether the transformation (Appendix B) between ABAQUS-variables and variables used in Eqs. 4.25 and 4.26 is correct, what is not possible if inhomogeneous material is used, where no analytical solutions are available.

For axis-symmetric problems ABAQUS gives the possibility to use axis-symmetric elements. The major advantage of these elements compared to 3D elements is that an axis-symmetric model is handled as a 2D model, what is much less computational time consuming than a 3D model. As a consequence, this gives the opportunity to choose a higher resolution, especially near the injection point where the largest pore pressure and stress changes will occur. A higher resolution will improve the precision of the results.

5.3.1 Model setup, boundary conditions, material properties

The homogeneous axis-symmetric model has vertical and horizontal extensions of each 25 km, representing a model with a diameter of 50 km. The dimension of the model is chosen that large to avoid boundary effects, as the analytical solution is valid for an

infinite medium. The model has a resolution of 8 m near the injection source, and the element size increases to ~300 m at the surface boundary, and up to 1100 m at the vertical and the bottom boundary. The model consists of 46477 four node axis-symmetric continuum elements which are able to handle pore pressure. Figure 5-1 shows a sketch of the model setup and the applied boundary conditions.

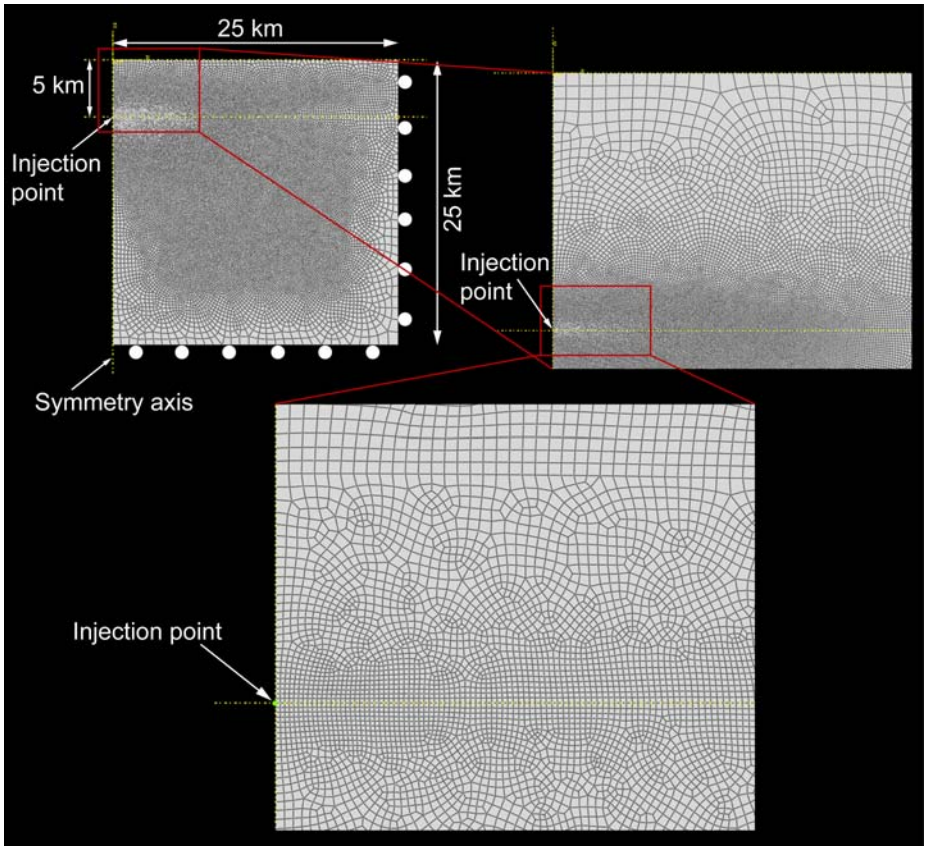

Figure 5-1. Setup, mesh and boundary conditions of axis-symmetric model.

The bottom and the side of the model are fixed in normal direction. To the surface no constraints are applied. Undrained boundary conditions are applied to the model, i.e. fluid cannot flow out of the model. The injection point is located on the vertical symmetry axis in a depth of 5 km. Gravity is not applied to the model. Only changes in pore pressure and stress induced by continuous fluid injection are considered. For this, the initial state of stress is unimportant, because only stress changes with respect to an initial stress state are of interest.

This model setup is used to simulate continuous fluid injection at a point source into homogeneous poroelastic space, and to model the fluid induced pore pressure and stress changes. The material properties defining a poroelastic rheology are given in Table 9. It is separated in parameters required as ABAQUS input, parameters needed for the transformation from ABAQUS-parameters into Rudnicki-parameters (Appendix B), and the Rudnicki-parameters themselves.

Initial conditions for pore pressure, stress, saturation and void ratio have to be assigned to the model. Pore pressure and stress state are initially set to zero, what means that the ΔP and $\Delta\sigma$ distributions generated by fluid injection represent also the pore pressure and stress state in the model. Furthermore, the saturation is initially set to $\chi = 1$ (fully saturated medium), and the initial void ratio is $e_0 = 0.1$.

Table 9. Material properties of homogeneous axis-symmetric model.

ABAQUS-parameters								
K_g [GPa]	K_f [GPa]	κ	ν	p_t^{el} [MPa]	e	k_f [m/s]	ρ_f [kg/m^3]	V_{fl} [m^3/s]
40	2	0.01	0.3	200	0.1	1.0E-7	1000	0.02

Parameters for transformation			
K_d [GPa]	φ	K_u [GPa]	K [m^{3}s/kg]
22	0.091	25.7	1.0E-11

Rudnicki-parameters					
α	λ [GPa]	μ [GPa]	λ_u [GPa]	c [m^2/s]	Φ/ρ_f [m^3/s]
0.45	15.2	10.2	18.9	0.166	0.02

5.3.2 Investigation

The point injection induced pore pressure and stress distributions in a homogeneous poroelastic medium, which is defined by the material parameters of Table 9, are modelled and compared to the analytical solutions of Rudnicki (1986) (Eqs. 4.25 and 4.26). Those modelling results enable to calculate the pore pressure stress coupling ratios for both, the radial stress and the tangential stress, which are compared to the ratios derived from the analytical solutions.

5.3.3 Results

a) Spatial distribution of pore pressure and stress (t = 34 days)

Figure 5-2 shows the spatial distributions of modelled pore pressure and stress changes, and those derived from the analytical solutions. As the results are plotted against the distance to the injection point along the *x*-axis, σ_{xx} is the radial stress and σ_{zz} the tangential stress. There is a reasonable good fit between numerical (dots) and analytical (solid lines) results for both, short distances (left subfigure) and large distances (right subfigure) to the injection point. Close to the source, the pore pressure change is larger than the stress changes, but decreases faster then the stress changes with distance to the injection point.

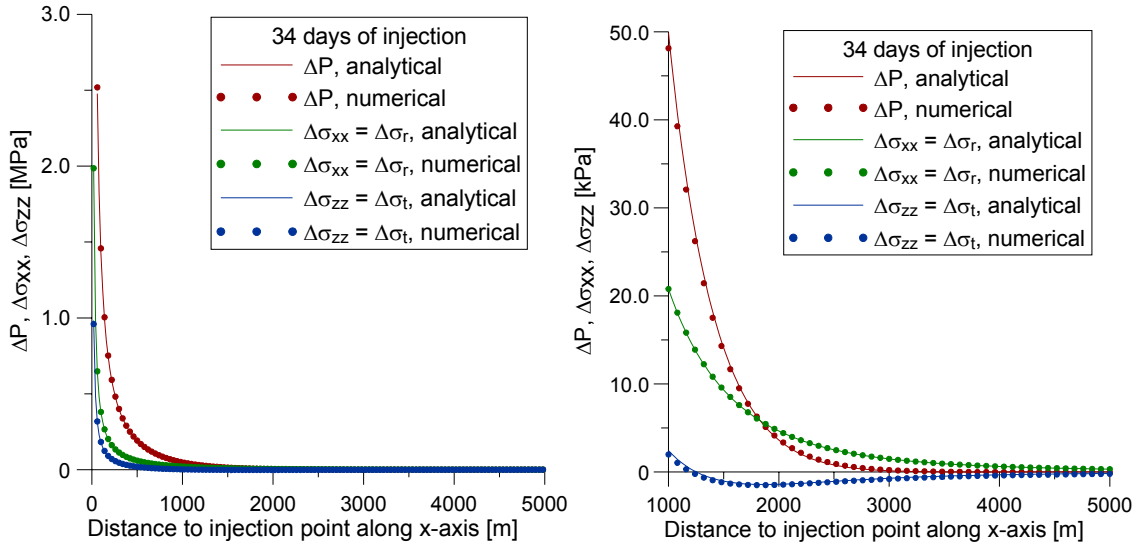

Figure 5-2. Spatial pore pressure and stress distribution after continuous fluid injection of 34 days along the horizontal *x*-axis. Right subfigure shows the section between 1000 and 5000 m of the left subfigure.

b) Spatial distribution of pore pressure stress coupling ratios (t = 34 days)

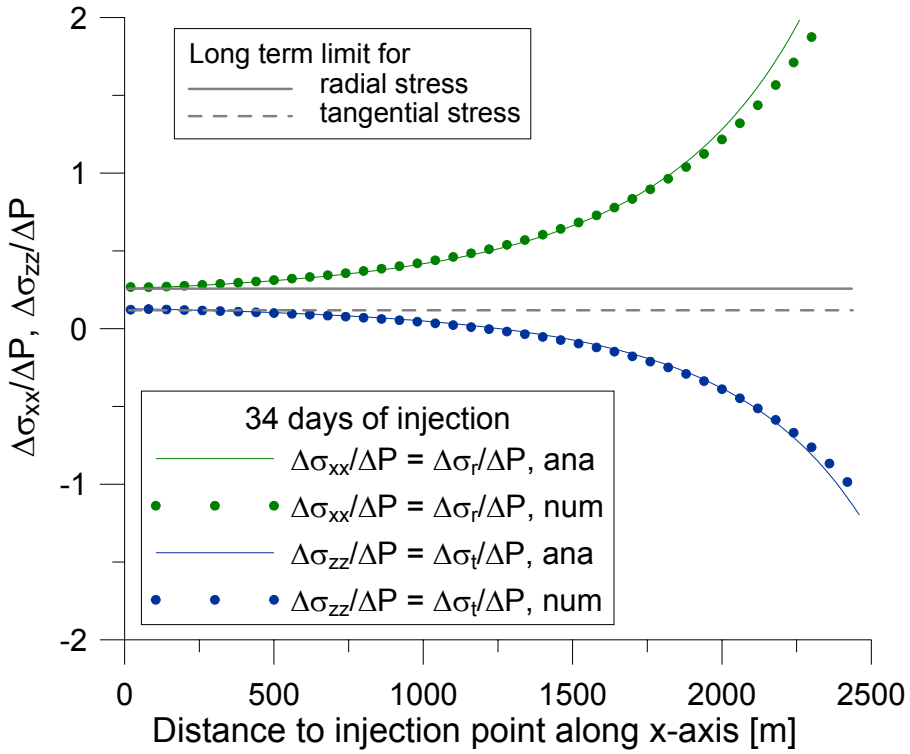

Figure 5-3.Comparison between modelled (dots) pore pressure stress coupling ratios and those derived from analytical solutions (solid lines), in dependence of the distance to the injection point along the horizontal *x*-axis.

The pore pressure stress coupling ratios are calculated by dividing the radial and the tangential stress change, respectively, by the pore pressure change. Both ratios are

plotted in Figure 5-3, which are derived from numerical simulation (dots) and from analytical calculation (solid lines). The pore pressure stress coupling ratios for the radial stress as well as for the tangential stress show quite a good fit between numerical and analytical results. Close to the injection point (x < 200 m) both values converge to their long-term limits, which are calculated after Eqs. 4.36 and 4.38, and plotted as grey horizontal solid (radial stress) and dashed (tangential stress) lines. The pore pressure stress coupling ratios diverge from their long-term limits with increasing distance to the point source. The reason for this deviation is the fact that it takes more time for the pore pressure change to diffuse than for the stress change to spread out. With distance to the injection point pore pressure change becomes smaller compared to the stress change, and thus pore pressure stress coupling ratio increases.

c) Temporal evolution of pore pressure and stress (x = 206 m)

In Figure 5-4 the temporal evolution of modelled (dots) and analytically derived (solid lines) pore pressure and stress changes at a distance of x = 206 m to the injection point are compared to each other. The graphs show a good match between numerical and analytical results. Here again, the different diffusion character of pore pressure and stress can be seen. For short injection times the radial stress change is larger than the pore pressure change. With duration of injection this behaviour flips.

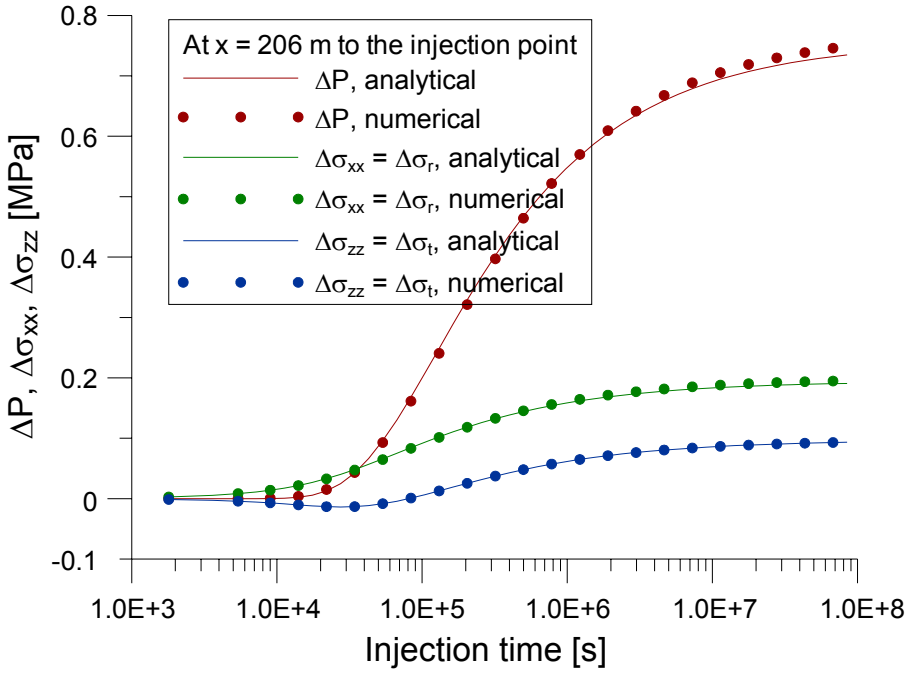

Figure 5-4. Comparison between numerical (dots) and analytical (solid lines) pore pressure, radial and tangential stress changes depending on injection time.

d) Temporal evolution of pore pressure stress coupling ratios (x = 206 m)

Using the previously modelled pore pressure and stress changes in dependence of time, the temporal evolution of the pore pressure stress coupling ratios is calculated and compared to ratios derived from analytical solutions. This is shown in Figure 5-5, where numerical (dots) and analytical (solid lines) pore pressure stress coupling ratios are plotted versus time and show quite a good fit. The long-term limits for the radial and the tangential stress, calculated by Eqs. 4.36 and 4.38, are illustrated as grey horizontal lines. With increasing injection time, the modelled and analytically derived radial and tangential pore pressure stress coupling ratios converge to their long-term limits.

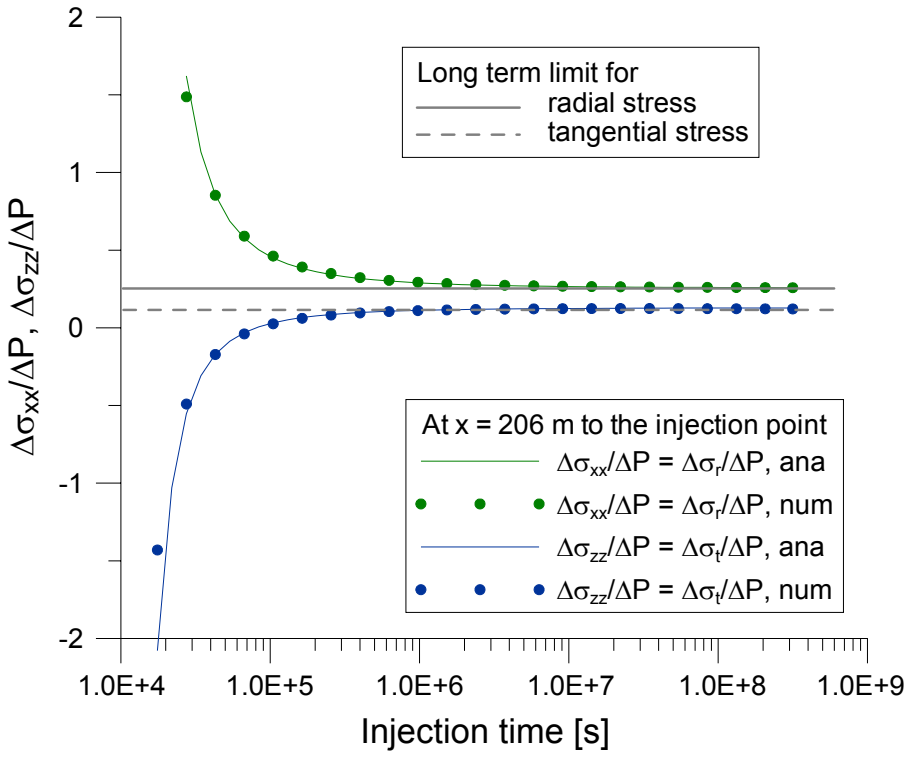

Figure 5-5. Temporal evolution of pore pressure stress coupling ratios derived from modelled data (dots) and from analytical solutions (solid coloured lines). The grey horizontal lines denote the long-term limits of the radial (solid) and the tangential (dashed) pore pressure stress coupling ratio.

5.3.4 Summary

Spatial as well as temporal distributions of pore pressure, stresses and pore pressure stress coupling ratios show quite a good match between numerical and analytical results. Also the modelled long-term limits of both pore pressure stress coupling ratios are in agreement with the observed field measurements for long injection times ($t > 5 \cdot 10^6$ s) or short distances to the injection point ($d < 300$ m). There are small deviations between numerical and analytical results in pore pressure, stress and pore pressure stress coupling ratios. These deviations mainly occur for after long injection times and at

bigger distances to the point source. The analytical solutions are valid for an infinite full space. On the contrary, the numerical model represents not an infinite space, but has boundaries. Tough the boundaries are far from the injection point, after long injection time, the pore pressure had time to diffuse and has reached the boundaries. As undrained boundary conditions are applied to the model, the fluid cannot escape or diffuse further at the model boundaries. This lead to an accumulation of fluid at the boundaries, and the pore pressure increases more than predicted by the analytical solutions. Due to pore pressure stress coupling also the stresses are affected by this effect. The longer the injection time, the stronger the effect of the undrained boundaries, and the more time that areas more far from the model boundaries are affected. Figure 5-3 shows the boundary effect at larger distance to the injection point, Figure 5-4 with duration of injection.

Nevertheless, the match between numerical and analytical results is satisfying. The results also show that the formulae for the transformation between ABAQUS parameters and Rudnicki parameters, provided in Appendix B, are correct, and ABAQUS was used in a proper way to model coupled fluid flow stress simulations with poroelastic material behaviour. Thus, in a next step, inhomogeneous poroelastic rheology will be applied in numerical simulations, where analytical solutions are not available anymore.

5.4 Inhomogeneous axis-symmetric model

In the following section fluid injection induced pore pressure and stress distributions inside an inhomogeneous poroelastic medium are modelled. For this purpose the homogeneous axis-symmetric model of the previous section is modified by including an ellipsoid, representing a reservoir, with material properties different from the surrounding.

5.4.1 Model setup, boundary conditions, material properties

The model dimensions and boundary conditions are shown in Figure 5-6. Compared to the homogeneous model (Figure 5-1) an ellipsoid is included, representing a reservoir. In the centre point of the reservoir fluid is injected at constant rate. The material properties of reservoir and surroundings are provided in Table 10. The material properties of the surroundings are equal to those of the homogeneous model (Table 9). The injection rate is now increased to V_{fl} = 50 l/s at the centre of the ellipsoidal reservoir. The reservoir is characterized by higher permeability, higher void ratio, higher Poisson's ratio and higher logarithmic bulk modulus compared to the background material.

No gravity was applied to the model, because only pore pressure and stress changes with respect to an initial state are investigated. Then, for pore pressure and stress states

any arbitrary initial states can be defined. The initial pore pressure and stress state was chosen to be zero. Thus, fluid injection induced pore pressure and stress change distributions are identical with the pore pressure and stress distributions. The poroelastic medium is considered to be fully saturated, therefore the saturation is initially set to χ = 1. Another initial condition applied to the model is the void ratio, which is set to e_0 = 0.3 in the ellipsoidal reservoir and e_0 = 0.1 in the surroundings.

5.4.2 Investigation

Table 10. Injection rate (values indented) and material properties of the inhomogeneous poroelastic axis-symmetric model.

	Parameter	Value, Ellipsoidal Inclusion	Value, Surroundings
ABAQUS-parameters	K_g [GPa]	40	40
	K_f [GPa]	2	2
	κ	0.03	0.01
	ν	0.4	0.3
	p_t^{el} [MPa]	200	200
	e	0.3	0.1
	k_f [m/s]	1.0E-5	1.0E-7
	ρ_f [kg/m^3]	1000	1000
	V_{fl} [m^3/s]	0.05	
Transformation-parameters	K_d [GPa]	8.67	22
	φ	0.23	0.09
	K_u [GPa]	13.41	25.72
	K [m^{3}s/kg]	1.0E-9	1.0E-11
Rudnicki-parameters	α	0.78	0.45
	λ [GPa]	7.43	15.23
	μ [GPa]	1.86	10.15
	λ_u [GPa]	12.17	18.95
	C [m^2/s]	5.5	0.1
	Φ/ρ_f [m^3/s]	0.05	

With the model setup shown in Figure 5-6 and the material properties given in Table 10, continuous fluid injection induced pore pressure and stress changes in an inhomogeneous poroelastic medium are modelled. The main focus of this investigation

is on the influence of the higher permeable reservoir on the resulting pore pressure and stress distribution inside and outside the reservoir.

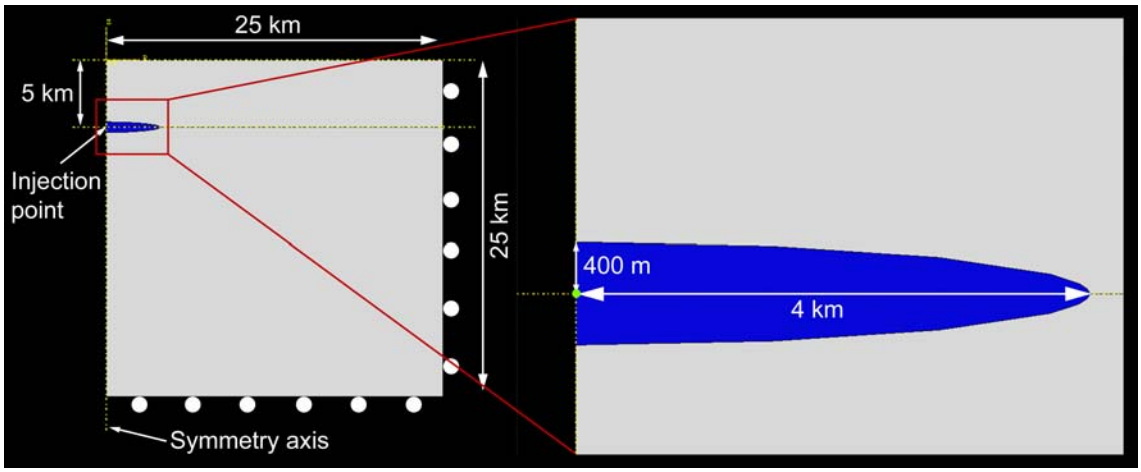

Figure 5-6. Inhomogeneous axis-symmetric model setup. The bottom and the model sides are fixed in normal direction. The injection point is located in the centre of the ellipsoid that has different material properties than the surroundings (Table 10). The same mesh was used as for the homogeneous model (Figure 5-1).

5.4.3 Results

Figures 5-7 and 5-8 show the pore pressure and total stress changes ΔP, $\Delta\sigma_{xx}$, $\Delta\sigma_{zz}$ along the x-axis and the z-axis, respectively, after 34 days and 255 days of fluid injection. As the permeability in the surroundings is by a factor of 100 lower than in the reservoir, pore pressure diffusion in the surroundings is slowed down, and therefore ΔP declines rapidly at the transition zone inside the surroundings. Once the pore pressure front reaches the reservoir-surroundings boundary, and P cannot diffuse as fast as in the reservoir anymore, fluid is accumulated inside the reservoir what leads ΔP to raise.

The tangential stress change $\Delta\sigma_t$ is more affected by the inhomogeneity than the radial stress change $\Delta\sigma_r$. After declining with distance from the injection point, $\Delta\sigma_t$ increases inside the reservoir before reaching the reservoir-surroundings boundary. This effect is lager along the vertical axis, where $\Delta\sigma_t = \Delta\sigma_{xx}$, (Figure 5-8) than along the horizontal axis, where $\Delta\sigma_t = \Delta\sigma_{zz}$, (Figure 5-7). At the reservoir-surroundings boundary, $\Delta\sigma_t$ declines in a step. Along the horizontal axis, $\Delta\sigma_r = \Delta\sigma_{xx}$ declines within a short distance in the vicinity of the reservoir-surrounding boundary (Figure 5-7), whereas along the vertical axis, $\Delta\sigma_r = \Delta\sigma_{zz}$ seems to be unaffected by the material contrast between reservoir and surroundings (Figure 5-8) and decreases continuously with distance from the injection source.

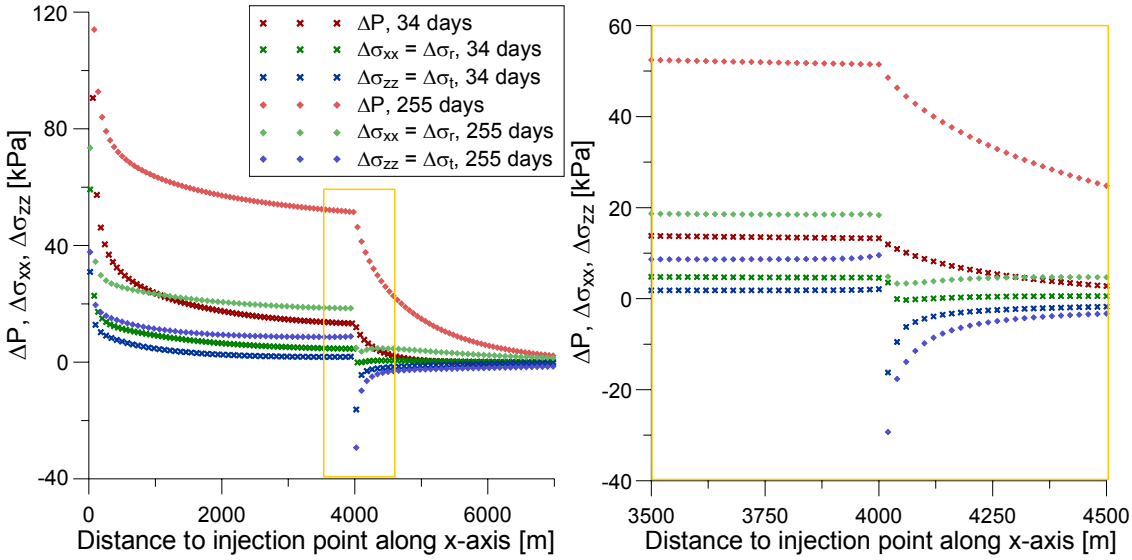

Figure 5-7. Pore pressure and stress changes along the horizontal *x*-axis for two injection times. The radial stress change is given by $\Delta\sigma_{xx}$, the tangential one by $\Delta\sigma_{zz}$. Right subfigure shows the area of the reservoir-surroundings transition zone in more detail compared to left subfigure. $\Delta\sigma_t$ becomes negative in the surroundings.

Figures 5-9 –5-13 show the pore pressure, total and effective σ_{xx}, σ_{zz} distributions on a vertical cross section after 34 and 255 days of continuous fluid injection. The absolute values of pore pressure and stresses are increasing and spreading out with time. The different material properties of reservoir and surroundings lead to strong pore pressure and stress changes at the reservoir-surroundings boundary. The apex of the reservoir is acting as stress concentrator, and leads to a large stress change at the boundary. The vertical stresses $\Delta\sigma_{zz}$ and $\Delta\sigma_{zz,eff}$, tangential stresses concerning the apex of the ellipsoid, are stronger affected (Figures 5-11, 5-13) by the stress concentration at the apex of the ellipsoid than the horizontal stresses $\Delta\sigma_{xx}$ and $\Delta\sigma_{xx,eff}$ (Figures 5-10, 5-12), which are radial stresses in this case.

Figure 5-9 shows that fluid injection leads to a positive ΔP inside the entire model, and thus to an increases in P. As the pore pressure initial condition was set to zero for the entire model, ΔP is equal to the resulting P-distribution. At a constant time, the largest amount of ΔP occurs close around the injection source, and then it decreases with distance. Inside the reservoir, ΔP declines continuously with distance. The higher permeability inside the horizontally elongated reservoir gives P a preferred diffusion direction, which causes pore pressure to diffuse faster inside the reservoir than in the surroundings. Thus, for distances larger than 400 m (distance between injection point and reservoir boundary along z-axis), ΔP reduces less in horizontal than in vertical direction, what leads to higher ΔP in horizontal than in vertical direction at the same distance from the injection point. At the reservoir boundary ΔP declines strongly due to the reduced diffusion capability inside the less permeable surroundings. With duration of injection, pore pressure increases within the model volume along any arbitrary direction.

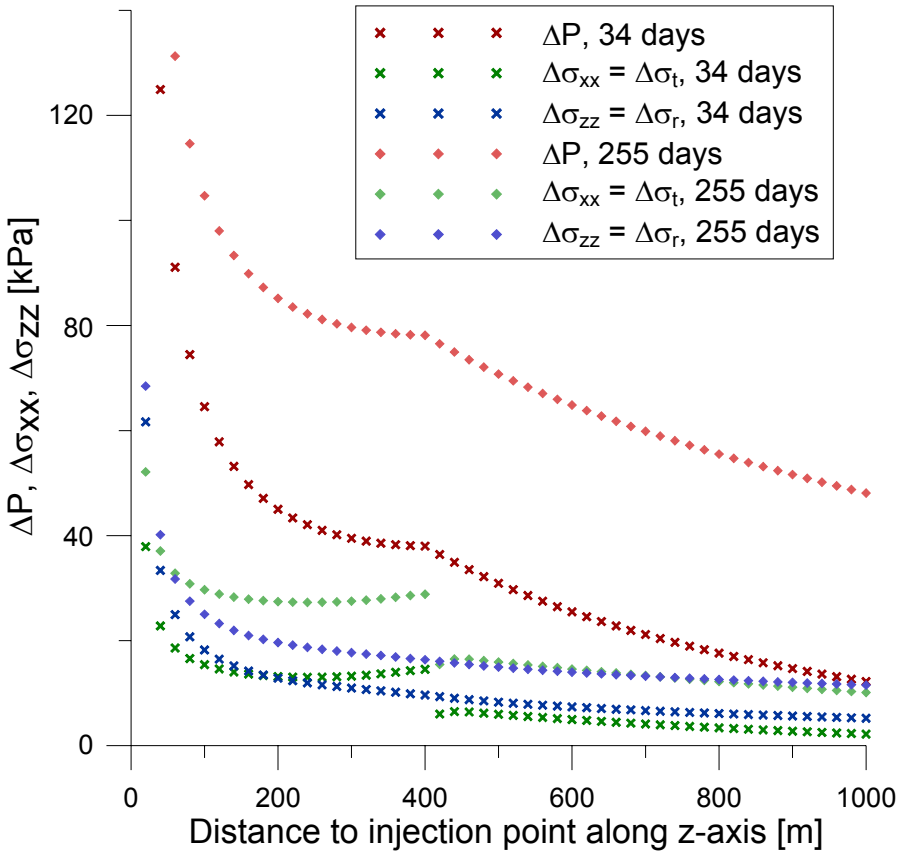

Figure 5-8. Pore pressure and stress changes along the vertical *z*-axis for two injection times. The radial stress change is given by $\Delta\sigma_{zz}$, the tangential one by $\Delta\sigma_{xx}$. $\Delta\sigma_r$ does not see the reservoir-surrounding boundary, whereas $\Delta\sigma_t$ shows a negative step at there.

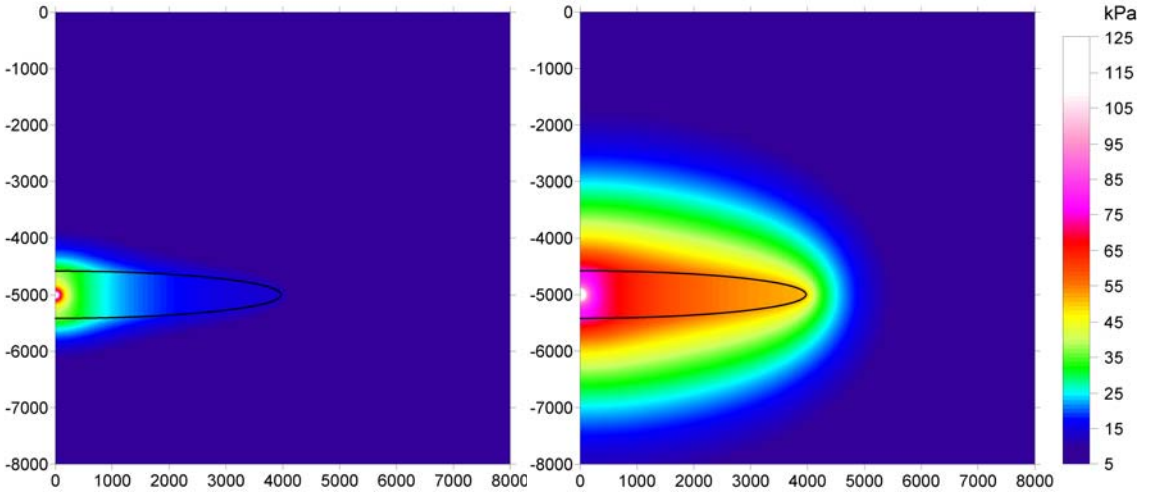

Figure 5-9. Pore pressure distribution after 34 days (left) and 255 days (right) of continuous fluid injection. The black solid line displays the reservoir boundary.

After longer duration of injection (Figure 5-9, right subfigure), when ΔP had time to diffuse into the surroundings, ΔP has diffused farer from the reservoir boundary into the surroundings above and below the injection point (ca. 2.6 km after 255 days of injection) than from the lateral boundary (ca. 1.2 km after 255 days of injection).

Another consequence is that at the same distance from the reservoir boundary ΔP is larger above and below the injection point (53 kPa at 500 m from the boundary) than laterally of the reservoir (26 kPa at 500 m from the boundary). Because of the ellipsoidal reservoir shape ΔP reaches the closer top and bottom boundaries before the farer horizontal boundary, and thus has above and below the injection point already diffused into the surroundings before the ΔP front reaches the horizontal boundary.

Like the pore pressure increases due to fluid injection, also the total normal stress changes $\Delta\sigma_{xx}$ and $\Delta\sigma_{zz}$ in horizontal and vertical direction, respectively, increase (Figures 5-10, 5-11). Similar to ΔP, $\Delta\sigma_{xx}$ and $\Delta\sigma_{zz}$ are largest at the injection point and decrease continuously with distance. At the reservoir boundary $\Delta\sigma_{xx}$ shows a stepwise decrease, which is largest at the apex of the ellipsoidal reservoir, where $\Delta\sigma_{xx}$ drops within a few tens of meters almost to zero, to increase after slightly again (Figure 5-10). Going from the top and bottom boundary of the reservoir in vertical direction outwards, $\Delta\sigma_{xx}$ declines and even becomes negative. With duration of injection this area expands and the minimum value becomes smaller. Like the pore pressure, the $\Delta\sigma_{xx}$ distribution is influenced by the permeability contrast between reservoir and surroundings. After longer duration of injection (255 days, right subfigure), $\Delta\sigma_{xx}$ is larger at any point inside the reservoir (> 20 kPa) than in the surroundings (< 17 kPa). This means that the largest stress changes occur inside the reservoir, and thus the $\Delta\sigma_{xx}$ distribution reflects the shape of the reservoir. The material properties of reservoir and surroundings differ not only in permeability, but also in logarithmic bulk modulus, Poisson's ratio and void ratio (Table 10). The diffusion process is mainly dependent on the permeability, thus the ΔP distribution is most influenced by the permeability contrast. In contrast, σ_{xx} is transferred by the solid parts of the rock, and therefore also logarithmic bulk modulus and Poisson's ratio (solid rock properties) will influence the stress distribution.

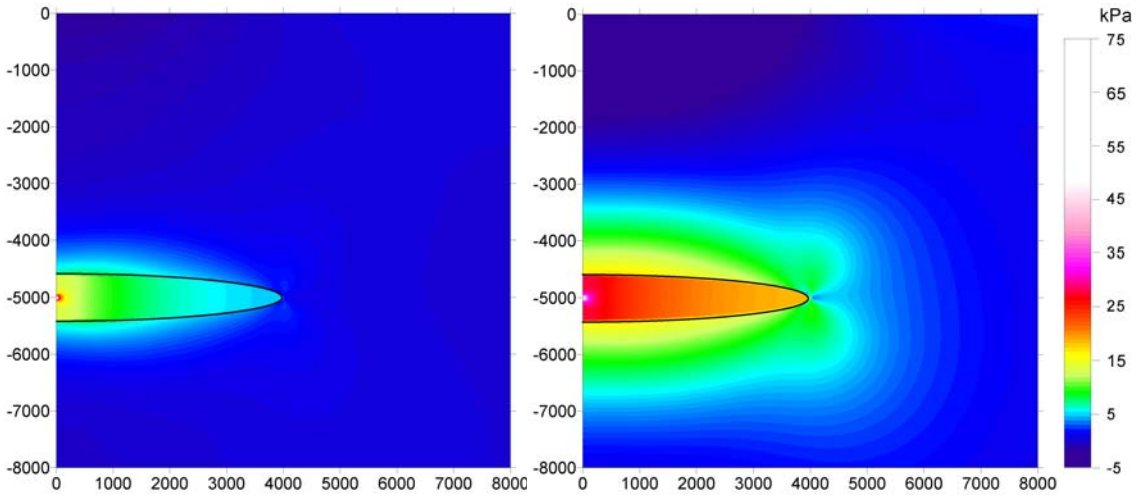

Figure 5-10. $\Delta\sigma_{xx}$ distribution after 34 days (left) and 255 days (right) of continuous fluid injection. The black solid line displays the reservoir boundary.

Considering the change in the total normal stress $\Delta\sigma_{zz}$ (Figure 5-11), the situation is a different one. Inside the reservoir at the same distance to the injection point, $\Delta\sigma_{zz}$ is larger in vertical than in horizontal direction. As the distance between point source and reservoir boundary is small above and below the injection point (400 m) compared to the distance to the lateral reservoir boundary (4000 m), the effect that the vertical is the preferred propagation direction of $\Delta\sigma_{zz}$ is marginal and can slightly be seen after short injection times (Figure 5-11, left). For longer injection times and areas not close to the apex of the ellipsoid, $\Delta\sigma_{zz}$ seems to spread out isotropic (Figure 5-11, right). Going in vertical direction from the injection point, the permeability contrast between reservoir and surrounding doesn't influence $\Delta\sigma_{zz}$. No strong decrease like in the case of ΔP or stepwise reduction ($\Delta\sigma_{xx}$) can be seen; $\Delta\sigma_{zz}$ decreases continuously in vertical direction with distance from the injection point, what also is shown in Figure 5-8. At the apex of the reservoir $\Delta\sigma_{zz}$ decreases largely in the surroundings close the reservoir boundary, and even becomes negative. This means that at this point, despite of fluid injection and pore pressure increase, the total normal stress σ_{zz} is reducing. After the same injection time, the maximum changes of $\Delta\sigma_{xx}$ and $\Delta\sigma_{zz}$, which occur at the injection point, are equal. With increasing distance to the injection point, in x-direction $\Delta\sigma_{xx}$ is larger than $\Delta\sigma_{zz}$, in z-direction vice versa. $\Delta\sigma_{xx}$ in x-direction is larger than $\Delta\sigma_{zz}$ in vertical direction, i.e. a larger difference between $\Delta\sigma_{xx}$ and $\Delta\sigma_{zz}$ in x- than in z-direction.

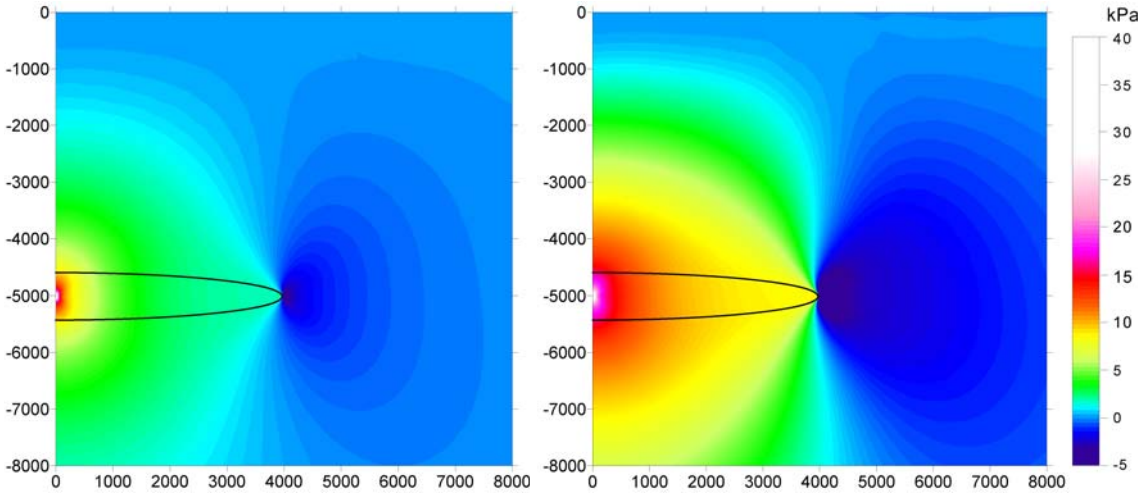

Figure 5-11. $\Delta\sigma_{zz}$ distribution after 34 days (left) and 255 days (right) of continuous fluid injection. The black solid line displays the reservoir boundary.

The distribution of the effective stress changes $\Delta\sigma_{xx,eff}$ and $\Delta\sigma_{zz,eff}$ on a vertical cross section are shown in Figures 5-12 and 5-13. Both effective stress changes are negative, i.e. the effective stress magnitudes are reduced by fluid injection. This is clear, because fluid injection, and thus pore pressure increase, lead to a decreasing effective stress state (Terzaghi, 1943). $\Delta\sigma_{xx,eff}$ and $\Delta\sigma_{zz,eff}$ are strongly influenced by the permeability contrast between reservoir and surroundings. Both values spread out faster inside the higher permeable reservoir before than in the surroundings. This can be seen best after short

injection times (left subfigures of Figures 5-12, 5-13). $\Delta\sigma_{xx,eff}$ and $\Delta\sigma_{zz,eff}$ show the largest changes at the injection point, which decrease with increasing distance. $\Delta\sigma_{xx,eff}$ shows also a strong reduction in a thin band around the reservoir. There, the change is even larger than in the reservoir itself, except close to the injection point, (Figure 5-12). Going from the reservoir boundary outwards, the magnitude of $\Delta\sigma_{xx,eff}$ declines in *x*-direction faster than in *z*-direction. Thus, at the same distance from the reservoir boundary, the magnitude of $\Delta\sigma_{xx,eff}$ is larger above and below (-30 kPa at 1 km from the reservoir boundary after 255 days of injection) than laterally of the reservoir (-12 kPa at 1 km from the reservoir boundary after 255 days of injection).

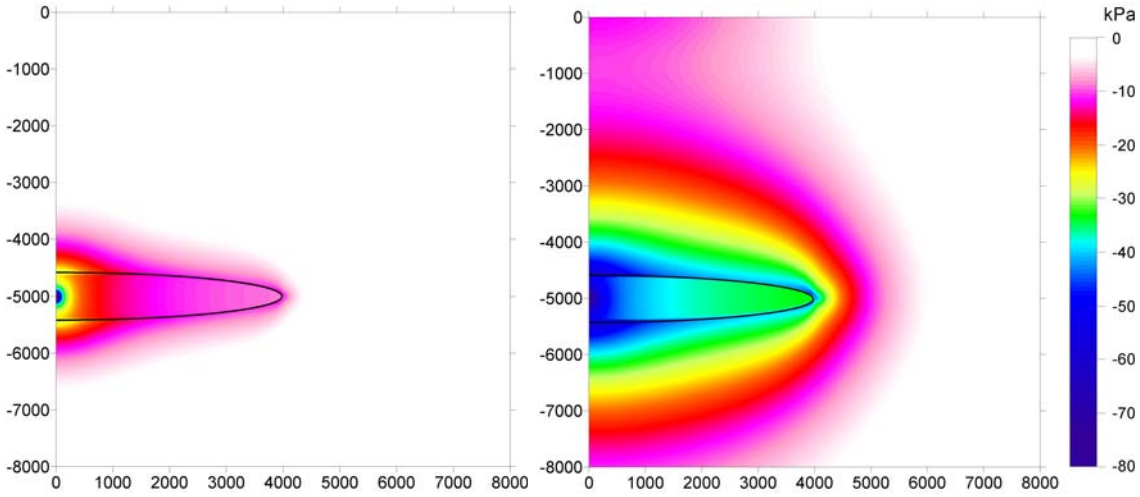

Figure 5-12. $\Delta\sigma_{xx,eff}$ distribution after 34 days (left) and 255 days (right) of continuous fluid injection. The black solid line displays the reservoir boundary.

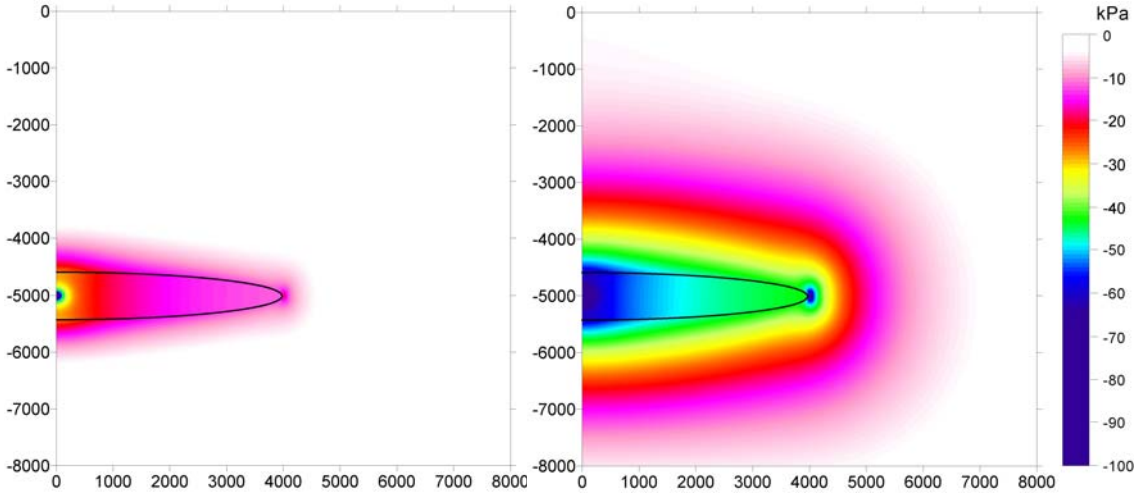

Figure 5-13. $\Delta\sigma_{zz,eff}$ distribution after 34 days (left) and 255 days (right) of continuous fluid injection. The black solid line displays the reservoir boundary.

However, $\Delta\sigma_{zz,eff}$ shows a strong spot-change inside the surroundings close to the apex of the reservoir (Figure 5-13). This is the same location, where $\Delta\sigma_{zz}$ is negative (Figure

5-11). With exception of this narrow localized negative value, the absolute value of $\Delta\sigma_{zz,eff}$ decreases isotropically with increasing distance from the reservoir boundary. The magnitudes of $\Delta\sigma_{xx,eff}$ and $\Delta\sigma_{zz,eff}$ behave vice versa than in the case of the total stress changes. In x-direction is $\Delta\sigma_{zz,eff}$ larger than $\Delta\sigma_{xx,eff}$, in z-direction is $\Delta\sigma_{xx,eff}$ larger than $\Delta\sigma_{zz,eff}$.

In Figures 5-14, 5-15 the spatial distribution of the pore pressure stress coupling ratios, $\Delta\sigma_{xx}/\Delta P$ (Figure 5-14) and $\Delta\sigma_{zz}/\Delta P$ (Figure 5-15), after 34 and 255 days of continuous fluid injection is illustrated. [Note: After short duration of injection (left subfigures) ΔP hasn't diffused that far. In areas, the ΔP diffusion front has not reached, ΔP should be zero. However, due to numerical wiggling, marginal pore pressure changes, which can either be positive or negative, are generated in areas the ΔP diffusion front has not reached. This leads to large positive or negative pore pressure stress coupling ratios, displayed as dark red and dark blue areas. These regions have to be neglected in the analysis of pore pressure stress coupling ratios.]

Despite ΔP and $\Delta\sigma_{xx}$ are changing inside the reservoir (Figures 5-9, 5-10), $\Delta\sigma_{xx}/\Delta P$ is constant there with a value of $\Delta\sigma_{xx}/\Delta P = 0.4$ for both injection times (Figure 5-14). At the reservoir boundary, $\Delta\sigma_{xx}/\Delta P$ decreases stepwise to a value of about 0.25 inside the surroundings. Above and below the reservoir, $\Delta\sigma_{xx}/\Delta P$ declines with increasing distance to the reservoir boundary, becomes zero and even negative. This is caused by the negative stress changes $\Delta\sigma_{xx}$ in this area (Figure 5-10). Laterally of the reservoir, $\Delta\sigma_{xx}/\Delta P$ increases with distance to the reservoir boundary. Those areas of pore pressure stress coupling decrease and increase are spreading out with duration of injection.

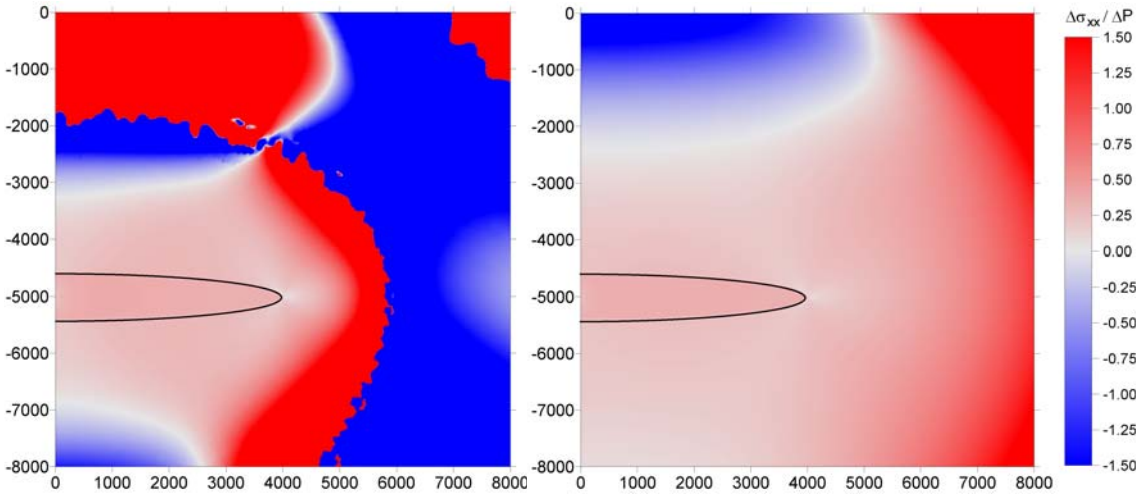

Figure 5-14. Pore pressure stress coupling ratio $\Delta\sigma_{xx}/\Delta P$ on vertical cross section after 34 days (left) and 255 (right) days of continuous fluid injection. The black solid line displays the reservoir boundary.

$\Delta\sigma_{zz}/\Delta P$ is about 0.2 inside the reservoir, what is half of the value of $\Delta\sigma_{xx}/\Delta P$. This is in agreement with the theoretical values for the long-term limits of the pore pressure stress

coupling ratios, which determines $\Delta\sigma_{zz}/\Delta P$ to be half the value of $\Delta\sigma_{xx}/\Delta P$ (Eqs. 4.36, 4.38). Due to the horizontally extended shape of the reservoir, $\Delta\sigma_{xx}$ can be assumed as radial stress change, $\Delta\sigma_{zz}$ as tangential stress change. In contrary to $\Delta\sigma_{xx}/\Delta P$, $\Delta\sigma_{zz}/\Delta P$ changes continuously at the top and bottom reservoir boundary. With increasing distance to the reservoir boundary $\Delta\sigma_{zz}/\Delta P$ increases. In lateral direction, $\Delta\sigma_{zz}/\Delta P$ declines within short distance from the reservoir boundary, and changes the sign from positive to negative. This is caused by the negative stress change in this area (Figure 5-11). With increasing lateral distance to the reservoir boundary, $\Delta\sigma_{zz}/\Delta P$ further declines, leading to larger negative values. The positive $\Delta\sigma_{zz}/\Delta P$ region above and below the reservoir, and the negative $\Delta\sigma_{zz}/\Delta P$ region laterally of the reservoir are spreading out with duration of injection.

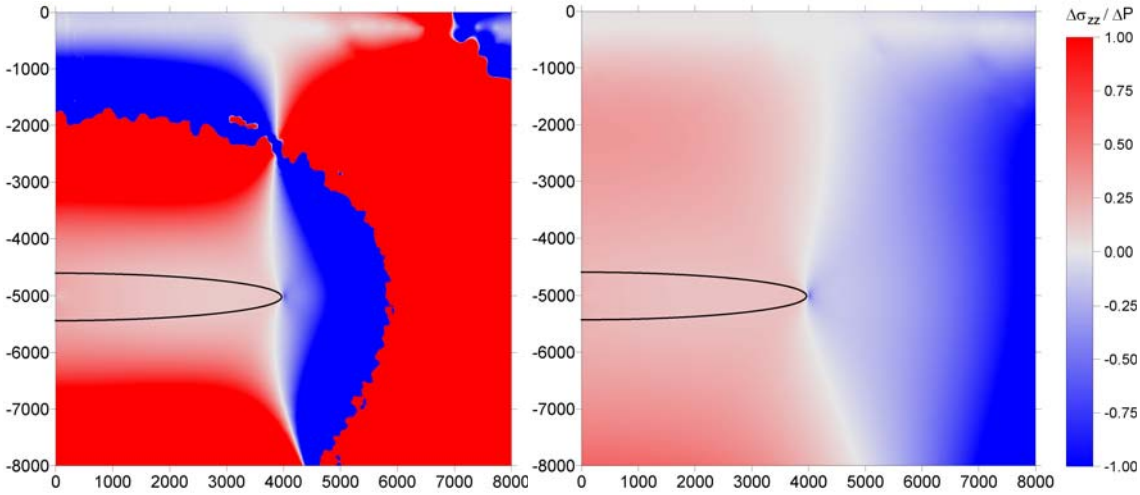

Figure 5-15. Pore pressure stress coupling ratio $\Delta\sigma_{zz}/\Delta P$ on vertical cross section after 34 days (left) and 255 days (right) of continuous fluid injection. The black solid line displays the reservoir boundary.

5.4.4 Summary and interpretation

Summarizing, the results of fluid injection induced pore pressure and stress changes inside an inhomogeneous poroelastic medium, that is described by an ellipsoidal reservoir embedded in surroundings (Figure 5-6), which have different poroelastic material properties (Table 10), show the following features:

ΔP, $\Delta\sigma_{xx}$ and $\Delta\sigma_{zz}$ are all affected by the material properties contrast between reservoir and surrounding. The permeability contrast causes the main effect on the pore pressure distribution, because it is a fluid material parameter, and therefore will affect ΔP, which is generated by the fluid distribution. In contrary, the difference of logarithmic bulk modulus and Poisson's ratio, parameters of the solid rock, between reservoir and surroundings, shouldn't have any effect on ΔP at all. The void ratio contrast with a factor of 3 between reservoir and surroundings is much weaker than the permeability

contrast with a factor of 100 between reservoir and surroundings. Hence, the permeability contrast plays the major role with respect to the pore pressure distribution. To verify this, ΔP is calculated inside the axis-symmetric model, with the permeability the only parameter varying between reservoir and surroundings. The result is shown in Figure 5-16. No obvious difference can be seen between this ΔP distribution and Figure 5-9, that displays the ΔP distribution of the axis-symmetric model with material properties as given in Table 10. Therefore, the influence of the other material property contrast is marginal compared to the effect of the permeability contrast or not present.

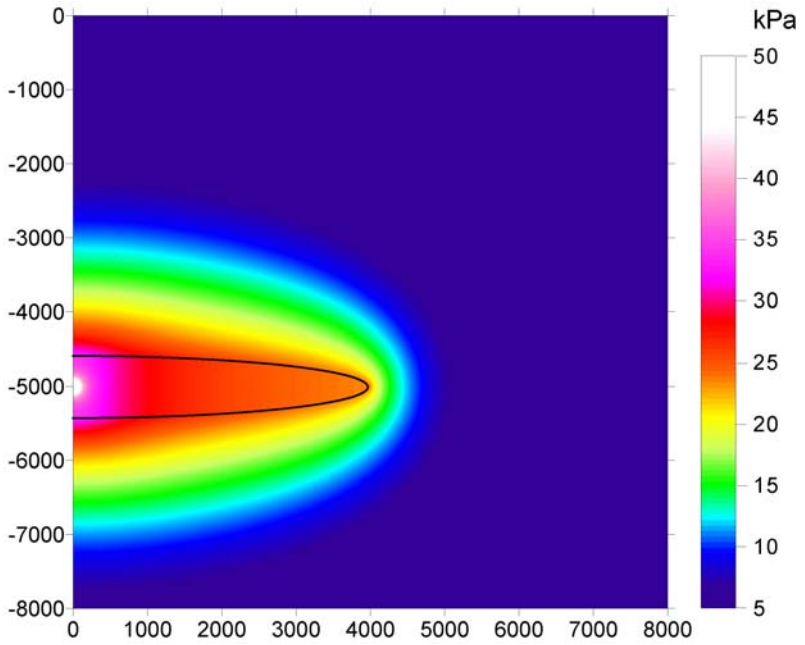

Figure 5-16. ΔP distribution after 255 days of fluid injection into axis-symmetric model. Inhomogeneity is given only by different permeabilities of reservoir (k_f = 1.0E-5 m/s) and surroundings (k_f = 1.0E-7 m/s). The black solid line displays the reservoir boundary.

For the sake of completeness, Figures 5-17 – 5-19 illustrate the pore pressure distributions of the axis-symmetric model, in which only one single material property varies between reservoir and surroundings. Neither the logarithmic bulk modulus (Figure 5-17), nor the Poisson's ratio (Figure 5-18), nor the void ratio (Figure 5-19) show any influence on the pore pressure distribution. In all three cases, ΔP is spreading out isotropically, and the distribution is radial symmetric. Hence, only the difference in permeability is affecting the distribution of pore pressure.

The higher permeability of the reservoir leads the pore pressure to diffuse faster inside the reservoir than in the surroundings. At the reservoir boundary diffusion is retarded due to the lower permeability in the surroundings, what leads to a) a fast decreases of ΔP with distance from the reservoir boundary, b) increasing pore pressure inside the reservoir (Figures 5-7 – 5-9), once the pore pressure has reached the reservoir boundary. Therefore, the ΔP distribution reflects the shape of the reservoir, and thus P is strongest

influenced close to the injection source and inside the reservoir. Outside the reservoir, P is stronger and more widely affected above and below the reservoir than lateral of it, because the top and bottom reservoir boundaries are closer than the lateral boundary, and thus P had more time to diffuse into the surroundings above and below the injection point.

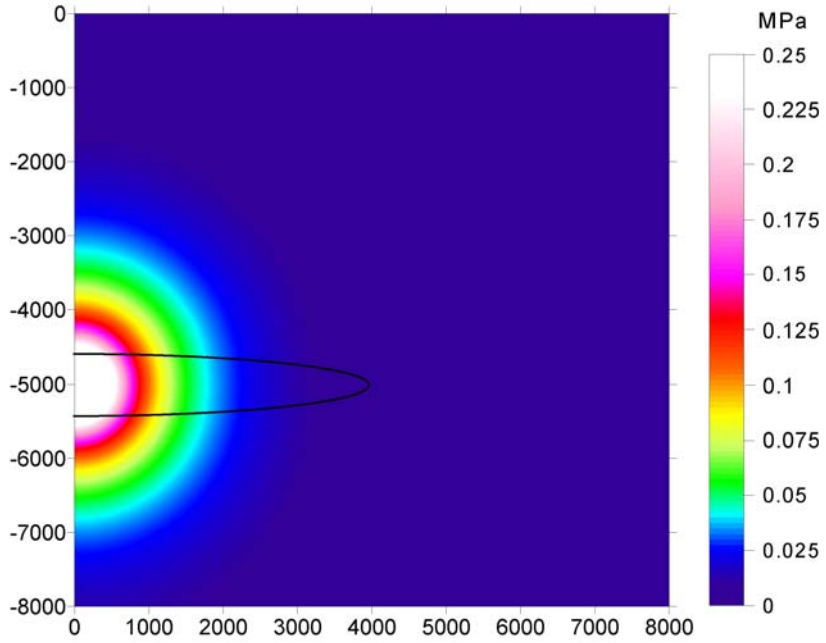

Figure 5-17. ΔP distribution of the axis-symmetric model with only a logarithmic bulk modulus contrast between reservoir ($\kappa = 0.03$) and surroundings ($\kappa = 0.01$), after 267 days of fluid injection. The black solid line displays the reservoir boundary.

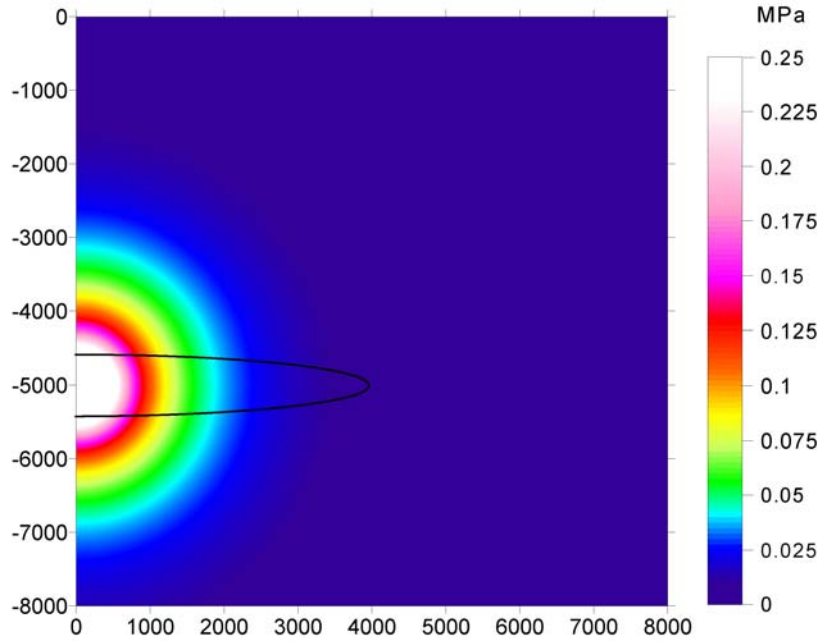

Figure 5-18. ΔP distribution of the axis-symmetric model with only the Poisson's ratio varying between reservoir ($\nu = 0.4$) and surroundings ($\nu = 0.3$), after 267 days of fluid injection. The black solid line displays the reservoir boundary.

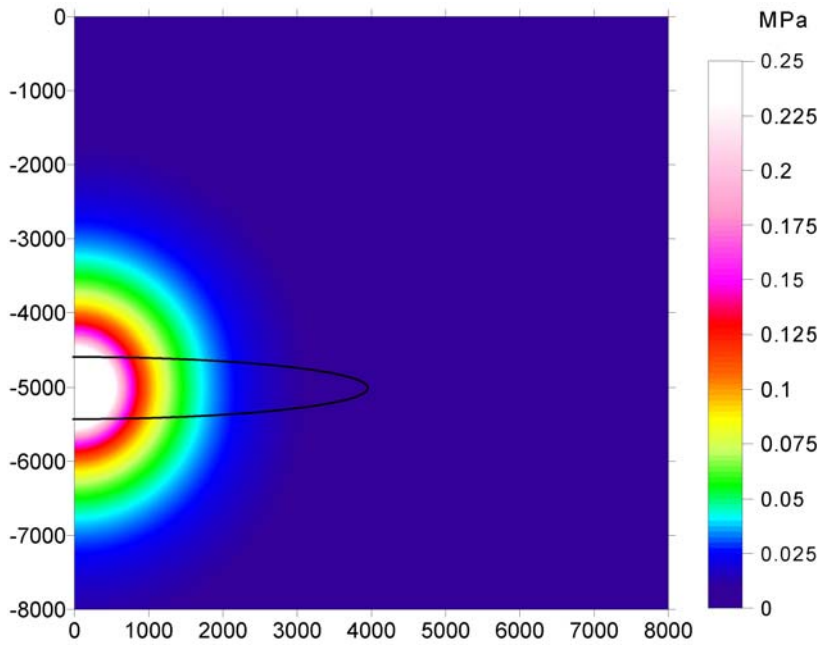

Figure 5-19. ΔP distribution of the axis-symmetric model, where the inhomogeneity is given by only the void ratio between reservoir (e = 0.3) and surroundings (e = 0.1), after 257 days of fluid injection.

$\Delta\sigma_{xx}$ shows a similar distribution like ΔP, with the difference that the decrease at the reservoir boundary occurs in a shorter distance, and the apex of the ellipsoid creates an anomaly of lower $\Delta\sigma_{xx}$ values. This anomaly is not present in the ΔP distribution, which is only affected by the permeability contrast, as shown before. Thus, the permeability contrast can't be in charge of the anomaly in the σ_{xx} distribution. Figure 5-20 shows the σ_{xx} distribution calculated in a model, where permeability is the only material property that differs between reservoir and surroundings. In this case, the anomaly of low $\Delta\sigma_{xx}$ values in the surroundings close to the apex of the reservoir is not existent. This means, it is not generated by the permeability contrast, but by the material property difference of either the logarithmic bulk modulus or the Poisson's ratio or the void ratio or any combination out of these three. To investigate this feature, $\Delta\sigma_{xx}$ is calculated in models characterized by the contrast of one single of those three material properties between reservoir and surroundings. Only the $\Delta\sigma_{xx}$ distribution of the model the logarithmic bulk modulus is varying between reservoir and surroundings shows the spot of low $\Delta\sigma_{xx}$ near the apex of the reservoir (Figure 5-21), similar to Figure 5-10. The other two material properties (Poisson's ratio and void ratio) don't lead to this discrete minimum in the change of σ_{xx}.

Nevertheless, $\Delta\sigma_{xx}$ is affected by the permeability contrast, as shown in Figure 5-20. As the permeability is a fluid material property, one should assume that $\Delta\sigma_{xx}$ is not influenced by it. The reason why $\Delta\sigma_{xx}$ depends on the permeability distribution is pore pressure stress coupling. σ_{xx} is radial stress along the x-axis, and the ellipsoidal reservoir is elongated in that direction. Therefore, σ_{xx} approximately is radial stress

inside the reservoir. As known from theory (Eq. 4.36), the coupling between pore pressure and the radial stress is strongest. ΔP is large inside the reservoir due to the permeability contrast, then, due to pore pressure stress coupling, also the radial stress change is large in this area, what can be seen in Figure 5-20. Hence, the permeability contrast between reservoir and surroundings is indirectly influencing the $\Delta\sigma_{xx}$ distribution, what pore pressure stress coupling is responsible for.

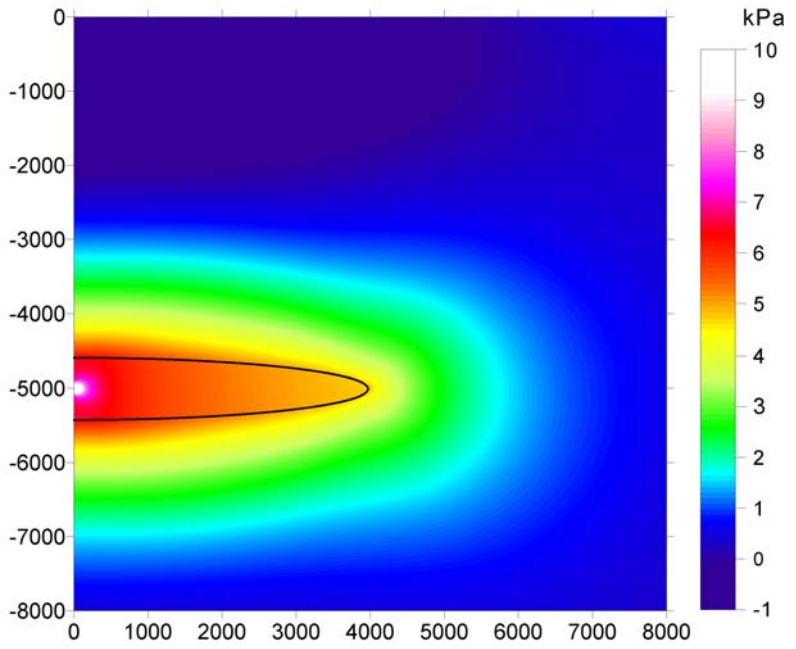

Figure 5-20. σ_{xx} distribution of the axis-symmetric model, where the inhomogeneity is given only by a different permeability of reservoir (k_f = 1.0E-5 m/s) and surroundings (k_f = 1.0E-7 m/s), after 255 days of fluid injection.

Like $\Delta\sigma_{xx}$, also $\Delta\sigma_{zz}$ is affected by the permeability distribution of the model, what can be explained by pore pressure stress coupling, analogue to the coupling between ΔP and $\Delta\sigma_{xx}$. In Figure 5-22 the $\Delta\sigma_{zz}$ distribution generated in an axis-symmetric model, with the only parameter that changes between reservoir and surroundings is the permeability, is displayed. Note the similarity between Figures 5-22 and 5-11, and thus the strong influence of the permeability on $\Delta\sigma_{zz}$ in comparison to the influence of other parameters.

As the effective stress changes $\Delta\sigma_{xx,eff}$ and $\Delta\sigma_{zz,eff}$ are calculated from ΔP and the stress changes, also $\Delta\sigma_{xx,eff}$ and $\Delta\sigma_{zz,eff}$ has to depend on the permeability contrast between reservoir and surroundings, like ΔP, $\Delta\sigma_{xx}$ and $\Delta\sigma_{zz}$ do. Therefore, the effective stress changes are calculated in a model, where the permeability is the only material property differing between reservoir and surroundings, in order to investigate the effect of the permeability contrast on $\Delta\sigma_{xx,eff}$ and $\Delta\sigma_{zz,eff}$. Figure 5-23 shows that, as expected, $\Delta\sigma_{xx,eff}$ as well as $\Delta\sigma_{zz,eff}$ depend on the permeability distribution of the model.

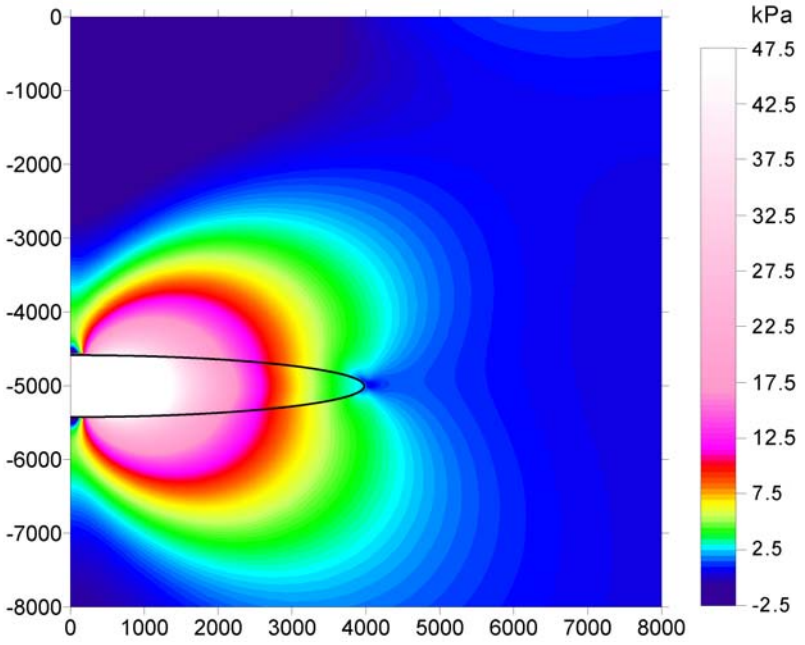

Figure 5-21. σ_{xx} distribution of the axis-symmetric model with the logarithmic bulk modulus as the only parameter differing between reservoir ($\kappa = 0.03$) and surroundings ($\kappa = 0.01$), after 267 days of fluid injection.

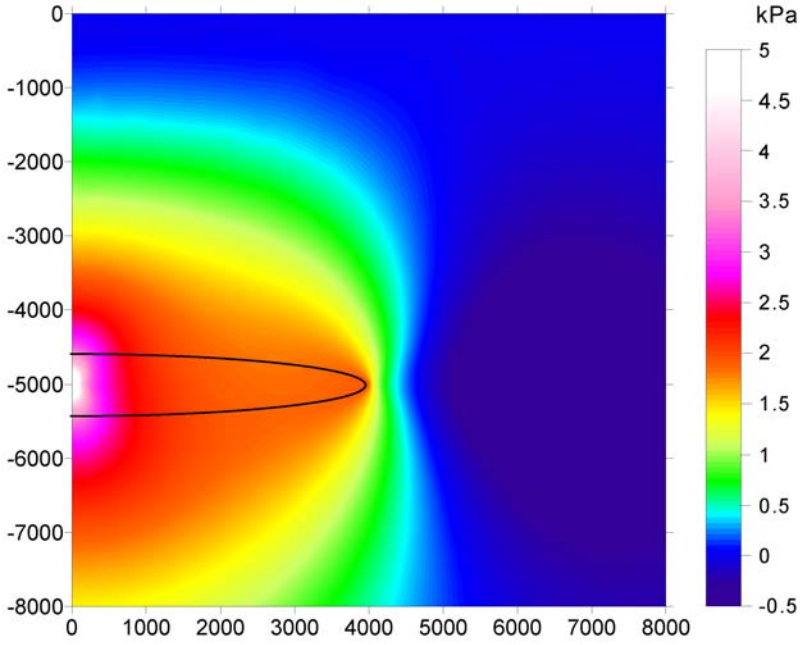

Figure 5-22. $\Delta\sigma_{zz}$ distribution of a axis-symmetric model characterized by different permeability between reservoir (k_f = 1.0E-5 m/s) and surroundings (k_f = 1.0E-7 m/s), after 255 days of fluid injection.

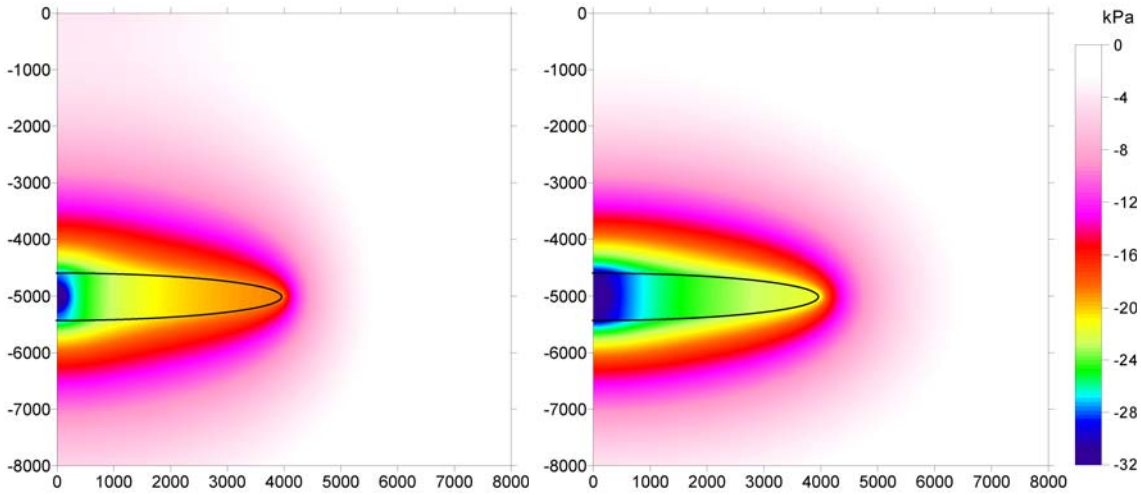

Figure 5-23. $\Delta\sigma_{xx,eff}$ (left) and $\Delta\sigma_{zz,eff}$ (right) depending only on the permeability contrast between reservoir (k_f = 1.0E-5 m/s) and surroundings (k_f = 1.0E-7 m/s), after 255 days of fluid injection.

In summary, permeability is the only parameter influencing the pore pressure distribution. It is my intention to analyse the poroelastic coupling effect of inhomogeneously distributed pore pressure on stress. To avoid any effect on the stress induced by inhomogeneous distributed rock parameters such as bulk moduli that do not affect the pore pressure, I have decided that in the following inhomogeneity is given by only the permeability.

5.5 Inhomogeneous 3D model

With the axis-symmetric model pore pressure and stress distribution can be calculated like in full space, but it is limited to two directions. In order to model pore pressure and stress distribution in real full space, a 3D model is used next. Then, the dependency of the stress components, and thus of pore pressure stress coupling, on all space directions can be investigated. Furthermore, a 3D model enables to apply an initial 3D stress state in order to define a tectonic stress regime. Therefore, also the influence of different tectonic stress regimes on the state of stress is investigated here.

5.5.1 Model setup, boundary conditions, material properties

The 3D poroelastic model is represented by a cube with an edge length of 10 km. This cube consists of two parts, an inner cuboid and its surroundings. Figure 5-24 shows the entire model (left) and a vertical cut through the model (right) to see structure and size of the inner and outer parts. The yellow part indicates the inner cuboid, which is representing a reservoir, and the outer part or surroundings are mapped in blue. The bottom and the sides of the model are fixed in normal direction, undrained boundary conditions are applied to the model boundaries, i.e. no fluid flow is allowed through the model boundaries. Fluid flow is generated by continuous fluid injection at one point. The injection point is located inside the reservoir at 5 km depth.

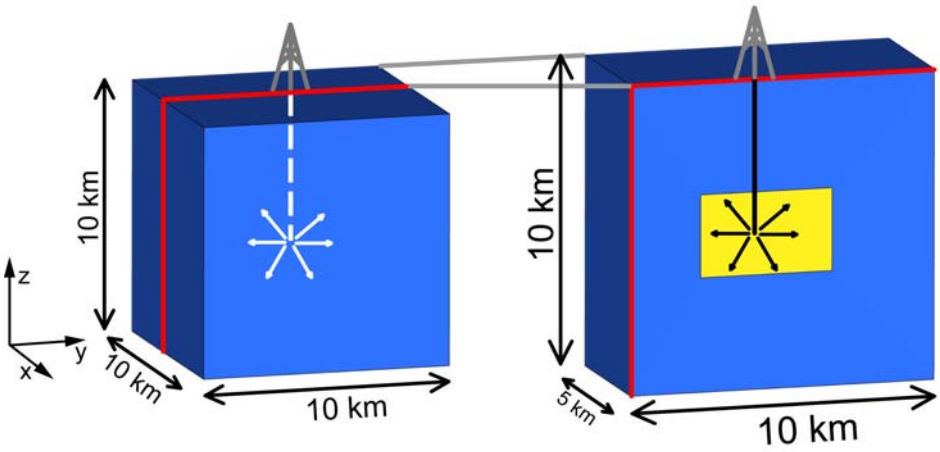

Figure 5-24. Setup of the inhomogeneous poroelastic 3D model. The permeability of the inner block (yellow), representing a reservoir with the dimensions of 3.4 x 4.3 x 2.7 km^3, is by a factor of 10 higher than in the outer region (blue). The injection point is located at x = 5 km, y = 4 km, z = 5 km, and with respect to the reservoir central in x- and z-direction, and at distances of 1.7 km and 2.7 km from the smaller and the larger, respectively, reservoir boundary in y-direction. The element size is 100 m inside the reservoir and increases up to 370 m at the model boundaries. The entire model consists of 146048 nodes and of 142443 hexahedral elements.

As demonstrated in the previous section, a permeability contrast between reservoir and surroundings has a much higher impact on the pore pressure and stress distribution than other material properties. Therefore, the same poroelastic rheology was chosen for both the cuboid and the surroundings, with exception of the permeability or diffusivity, respectively, which in the reservoir is 10 times higher than in the surroundings. By initial conditions, the saturation is set to $\chi = 1$, what means that the medium is fully saturated. The initial void ratio is $e_0 = 0.4$. For the full poroelastic material description, see Table 11.

To investigate the influence of the tectonic stress regime on fluid flow induced stress changes, gravity as well as an initial state of stress is applied to the model. The vertical stress is given by the weight of the overburden, the horizontal stresses are initially set to a certain ratio of the vertical stress. To realize a normal faulting regime, I have set the maximum horizontal stress to $0.9 \cdot \sigma_V$ in x-direction, the minimum horizontal stress to $0.6 \cdot \sigma_V$ in y-direction. To apply a strike-slip regime to the model, the factor of the maximum horizontal stress was increased to $1.1 \cdot \sigma_V$ in x-direction. Therefore, for the normal faulting regime principal stresses are orientated:
x-direction: $\sigma_2 = \sigma_H$, y-direction: $\sigma_3 = \sigma_h$, z-direction: $\sigma_1 = \sigma_V$

Analogous, for the strike-slip regime, the principal stresses are orientated:
x-direction: $\sigma_1 = \sigma_H$, y-direction: $\sigma_3 = \sigma_h$, z-direction: $\sigma_2 = \sigma_V$

Table 11. Injection rate (values indented) and material properties of the 3D inhomogeneous poroelastic model. The inhomogeneity is generated by only the permeability; related properties are printed bold.

	Parameter	Reservoir	Surroundings
ABAQUS-parameters	K_g [GPa]	40	40
	K_f [GPa]	2	2
	κ	0.025	0.025
	ν	0.25	0.25
	p_t^{el} [MPa]	250	250
	e	0.4	0.4
	k_f [m/s]	**2.0E-7**	**2.0E-8**
	ρ_f [kg/m^3]	1000	1000
	ρ_S [kg/m^3]	2500	2500
	V_{fl} [m^3/s]	0.1	
Transformation-parameters	K_d [GPa]	14	14
	φ	0.29	0.29
	K_u [GPa]	16.8	16.8
	K [m^{3}s/kg]	**2.0E-11**	**2.0E-12**
Rudnicki-parameters	α	0.65	0.65
	λ [GPa]	8.4	8.4
	μ [GPa]	8.4	8.4
	λ_u [GPa]	11.2	11.2
	C [m^2/s]	**0.12**	**0.012**
	Φ/ρ_f [m^3/s]	0.1	

5.5.2 Investigation

The model setup allows calculating spatio-temporal pore pressure and stress changes inside the reservoir and the surroundings, which are induced by continuous fluid injection at a point source. Furthermore, the modelled stress changes are used to calculate spatio-temporal changes in maximum shear stress $\Delta\tau_{max}$. Here, $\Delta\tau_{max}$ is used as a parameter to investigate the effect of inhomogeneous pore pressure stress coupling. In addition $\Delta\tau_{max}$ gives information whether rock is brought closer to failure or is stabilized due to pore pressure stress coupling affecting stress components differently. The main

objectives are a) to investigate how the permeability contrast influences the temporal and spatial distributions of pore pressure and stress. Due to inhomogeneous pore pressure stress coupling this effect on the stress components is investigated for different spatial directions; b) to analyse the poroelastic part of the effect of fluid injection on the rock stability in terms of change in maximum shear stress $\Delta\tau_{max}$; c) to investigate the influence of the tectonic regime on the distribution of $\Delta\tau_{max}$, and thus on rock stability.

5.5.3 Results

Pore pressure and stress

Pore pressure distributions after 3, 23 and 259 days of continuous fluid injection are shown in Figure 5-25 as vertical cross sections through the injection point. In Figures 5-26 – 5-28 the distributions in stress change of the three normal stresses σ_{ii} are plotted, induced by continuous fluid injection of 23 and 259 days. The results are mapped on three planes, rectangularly orientated along the axes of the rectangular coordinate system of Figure 5-24. The cutting point of the three planes is the injection source. The pore pressure and stress results shown here are calculated for a normal faulting regime.

The stress distributions $\Delta\sigma_{xx}$ (Figure 5-26), $\Delta\sigma_{yy}$ (Figure 5-27) and $\Delta\sigma_{zz}$ (Figure 5-28) show all a similar pattern, which differs only with the orientation of the stress component. In all cases, $\Delta\sigma_{ii}$ is largest at the injection point and then decreases with distance to the point source. The distributions of the normal stresses are elongated in the direction of their stress components, e.g. σ_{xx} in x-direction. These are also the directions, in which normal stresses are radial stresses.

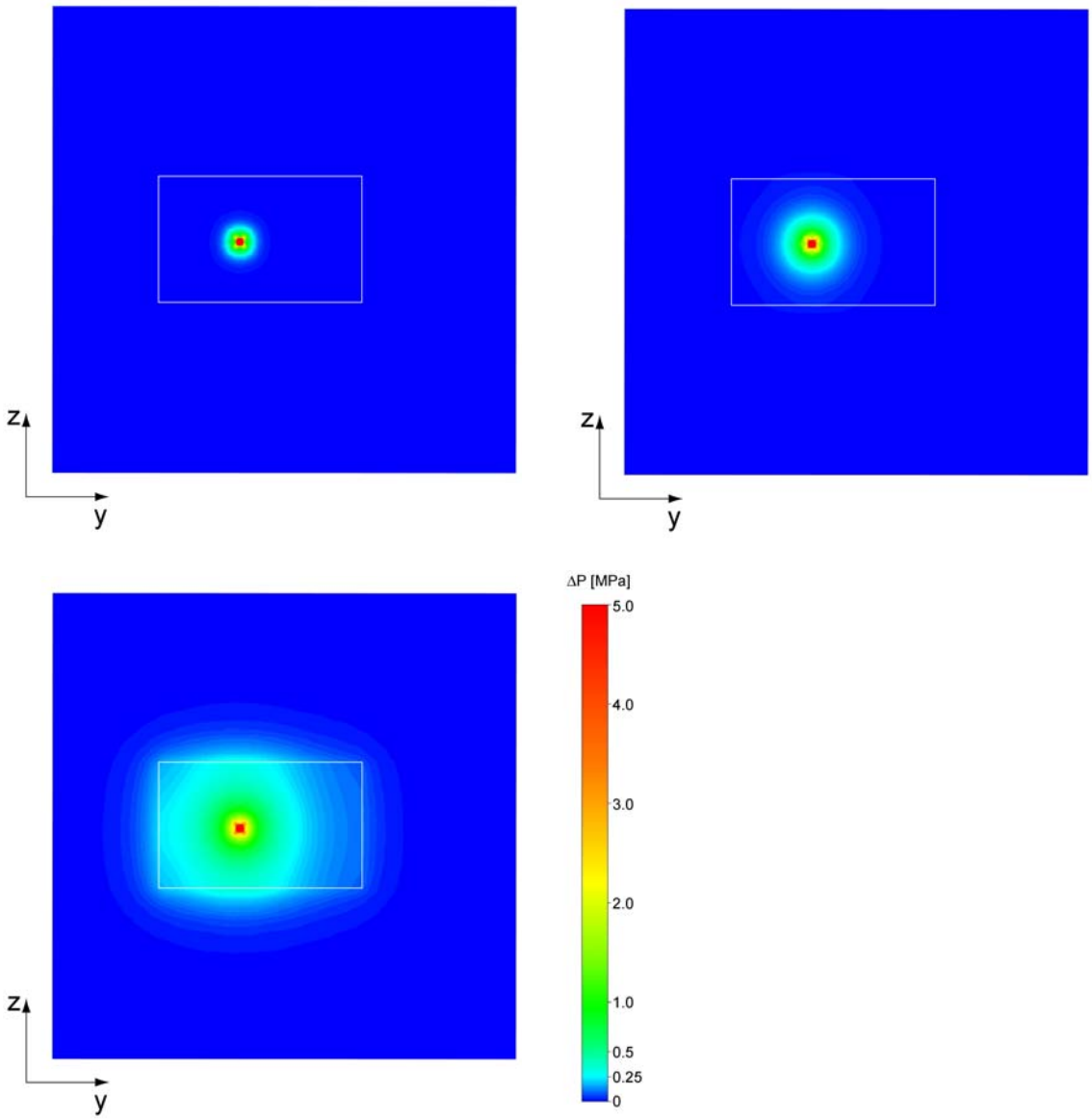

Figure 5-25. Δ*P* distribution after 3 (top, left), 23 (top, right) and 259 days (bottom) of continuous fluid injection. White rectangles show the boundary between the inner reservoir and the surroundings.

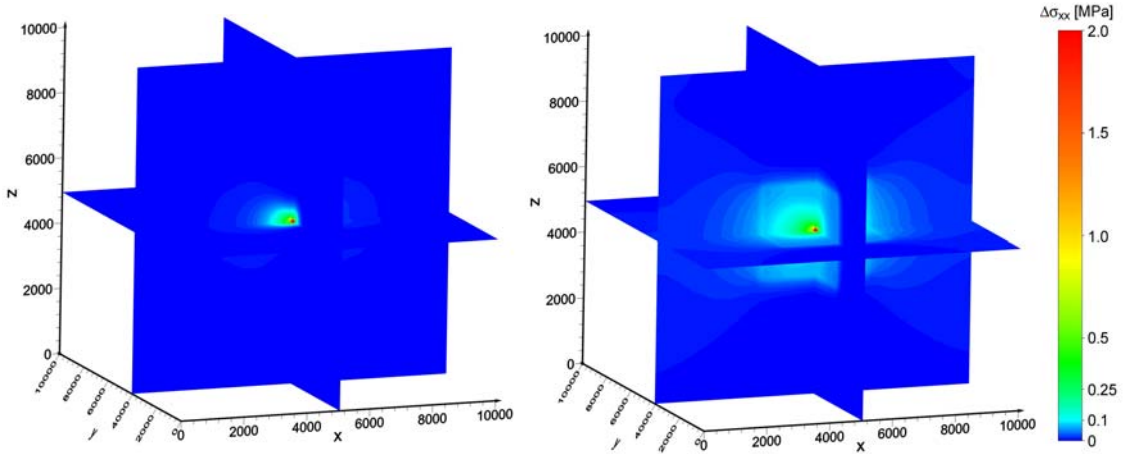

Figure 5-26. $\Delta\sigma_{xx}$ distribution after 23 days (left) and 259 days (right) of continuous fluid injection. At the same distance to the injection point, $\Delta\sigma_{xx}$ is larger in *x*-direction than in *y*- and *z*-directions.

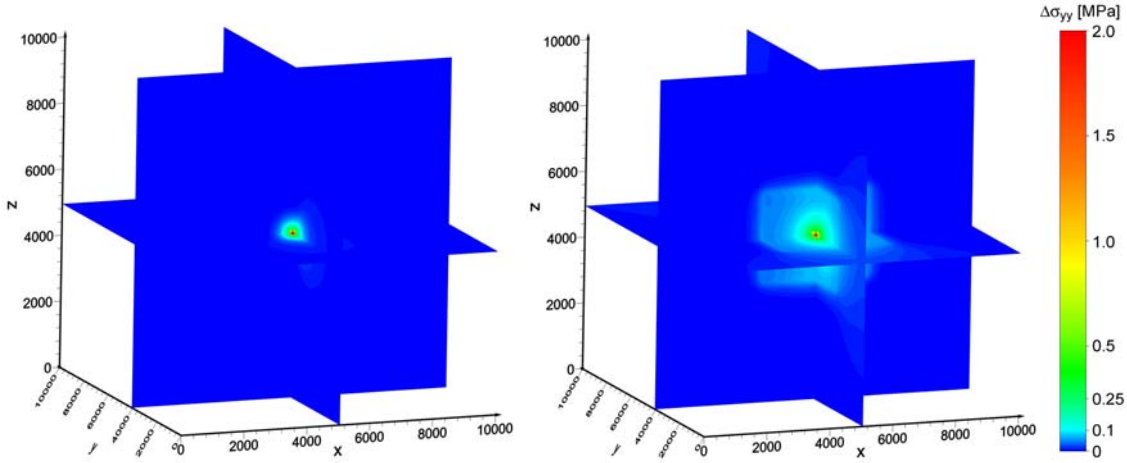

Figure 5-27. $\Delta\sigma_{yy}$ distribution after 23 days (left) and 259 days (right) of continuous fluid injection. At the same distance to the injection point, $\Delta\sigma_{yy}$ is larger in *y*-direction than in *x*- and *z*-directions.

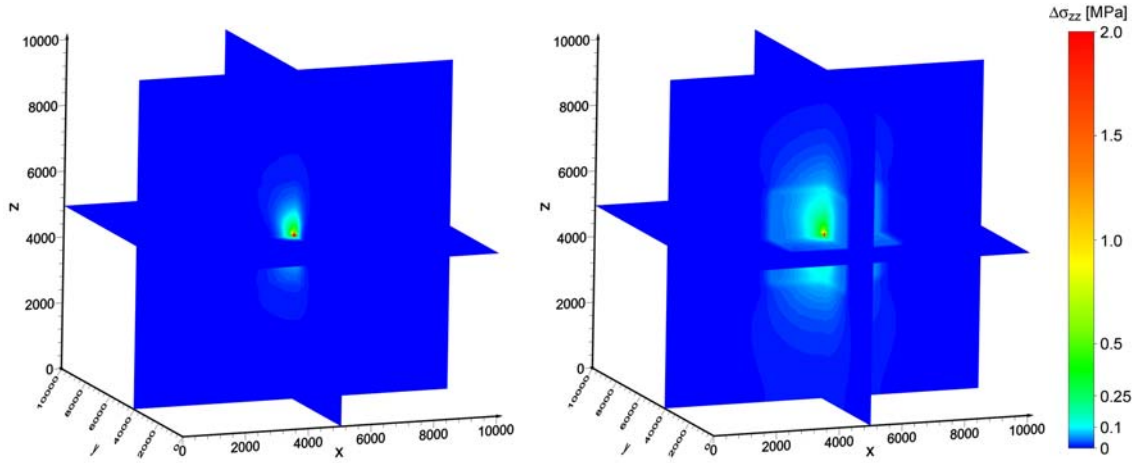

Figure 5-28. $\Delta\sigma_{zz}$ distribution after 23 (left) days and 259 days (right) of continuous fluid injection. At the same distance to the injection point, $\Delta\sigma_{zz}$ is larger in *z*-direction than in *x*- and *y*-directions.

Change in maximum shear stress

To analyse the anisotropic pore pressure stress coupling, the change in maximum shear stress $\Delta\tau_{max}$ is investigated. $\Delta\tau_{max}$ is also a measure whether rock is brought closer to failure ($\Delta\tau_{max} > 0$) or is stabilized ($\Delta\tau_{max} > 0$). Figure 5-29 shows the spatial $\Delta\tau_{max}$ distribution in a normal faulting regime after 23 days of continuous fluid injection on three cross-sections, each through the injection point.

Along the *z*-direction, the direction of σ_V, $\Delta\tau_{max}$ is positive, what is equal to an increased differential stress and a larger Mohr circle. In those areas the poroelastic coupling would have brought rock closer to failure. Along the *y*-direction or the σ_h-direction $\Delta\tau_{max}$ is negative. This means, smaller differential stresses and smaller Mohr circles in this direction. In *x*-direction or σ_H-direction no change in maximum shear stress can be observed.

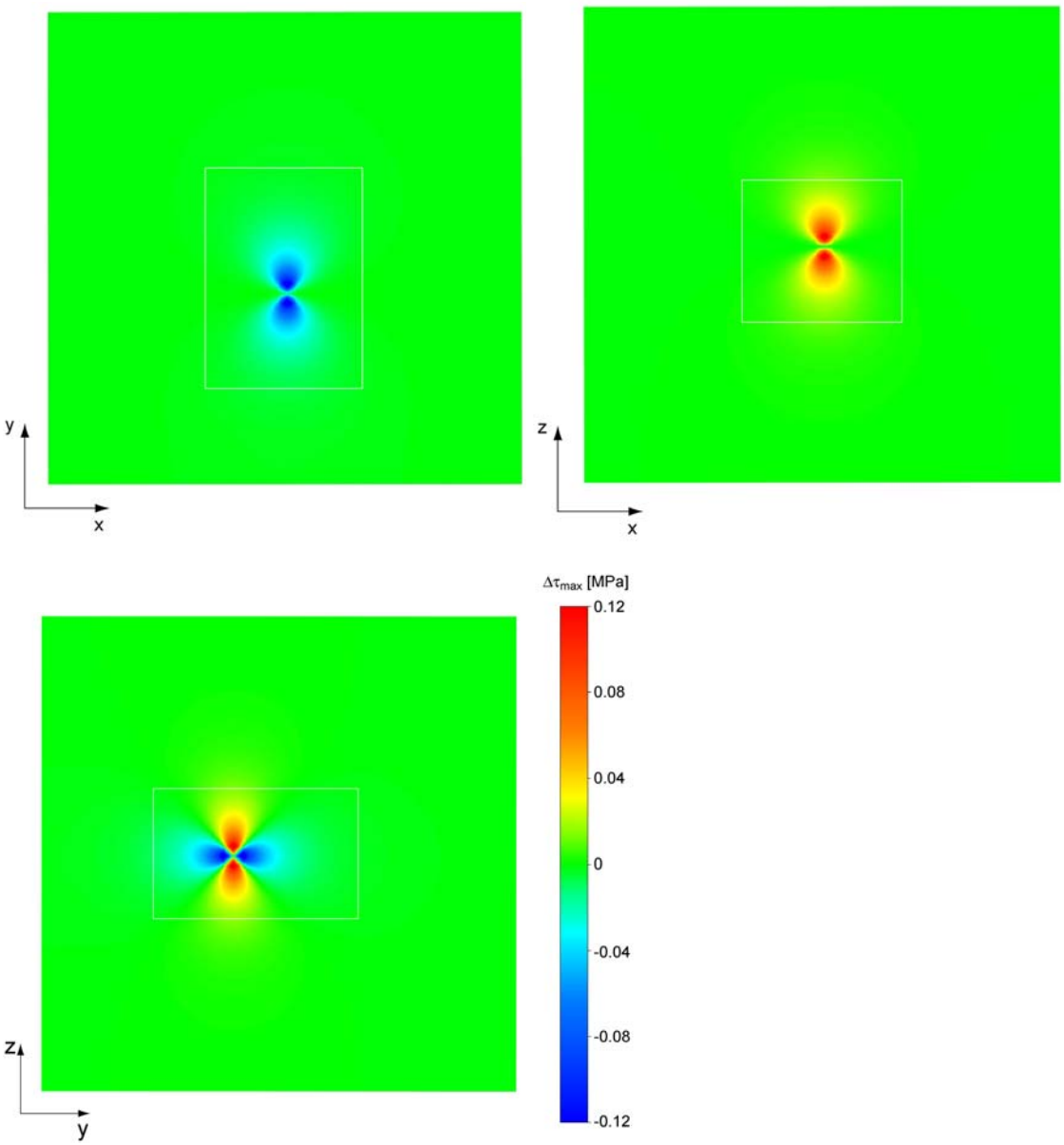

Figure 5-29. Spatial distribution of maximum shear stress in a normal faulting regime after 23 days of continuous fluid injection plotted on three different cross-sections. Note the different orientations of the cross-sections.

The temporal evolution of $\Delta\tau_{max}$ in a normal faulting regime is shown in three plots after 3, 23 and 259 days of continuous fluid injection (Figure 5-30). The results are plotted on a cross-section through the injection point. The second subfigure in Figure 5-30 is equivalent with the third subfigure of Figure 5-29.

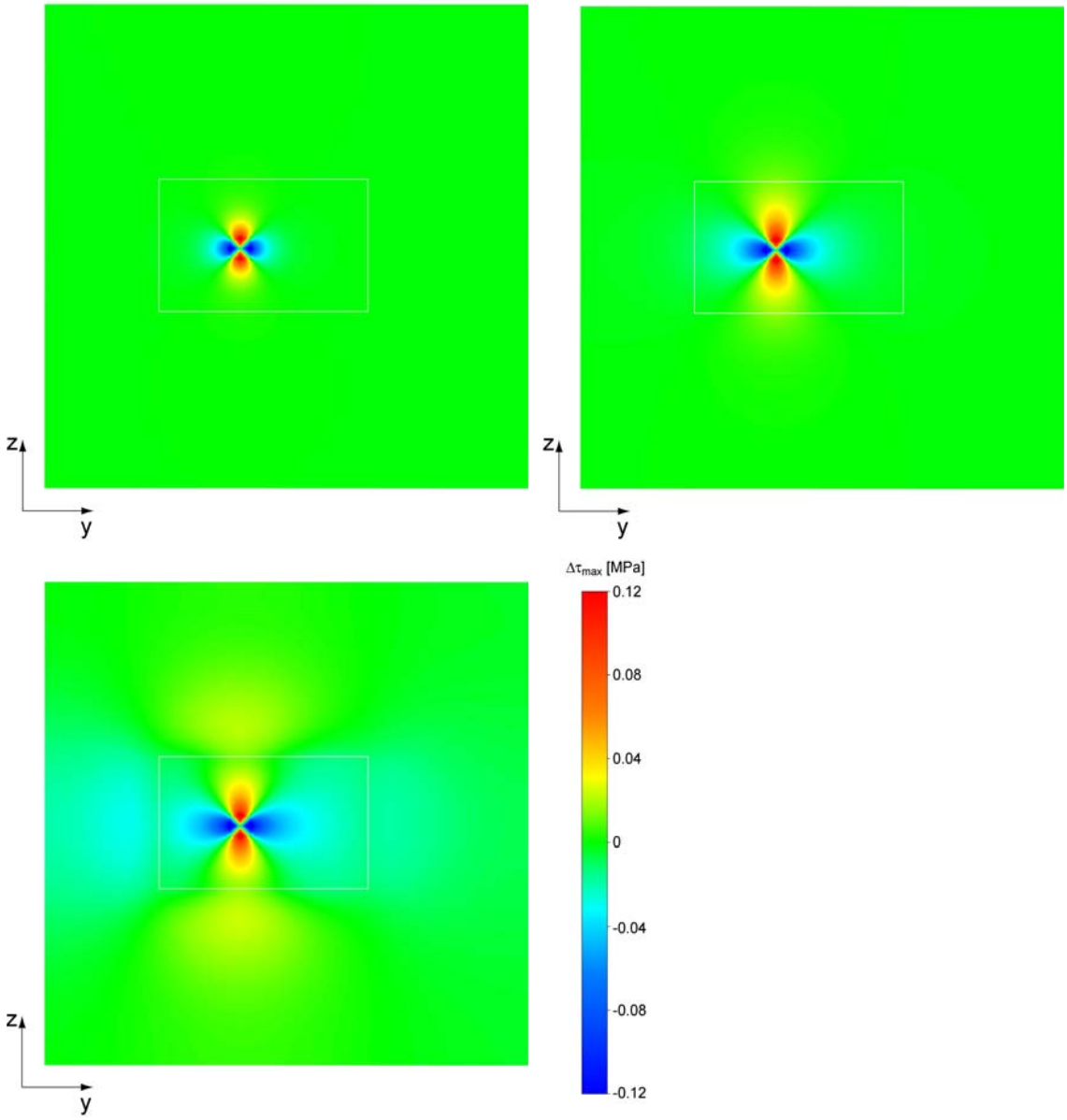

Figure 5-30. Temporal evolution of maximum shear stress in a normal faulting regime displayed on vertical cross-sections through the injection point after 3, 23 and 259 days of continuous fluid injection.

Looking at the maximal magnitude of $\Delta\tau_{max}$, one will notice that already after 3 days of injection, $\Delta\tau_{max}$ has reached almost its maximum values. With increasing injection time, $\Delta\tau_{max}$ is spreading out, without increasing its magnitude.

Influence of tectonic stress regime on maximum shear stress change

To investigate the effect of different tectonic stress regimes on the poroelastic coupling and therefore on the change in maximum shear stress, continuous fluid injection in a strike-slip regime is modelled and the results are shown here. These results can be compared to those of the previous section, where poroelastic coupling was investigated in a normal faulting regime. The results of $\Delta\tau_{max}$ in a strike-slip regime, induced by continuous fluid injection are illustrated in Figure 5-31. The plots show three different

cross-sections, each through the injection point, of $\Delta\tau_{max}$ distributions after 23 days of fluid injection.

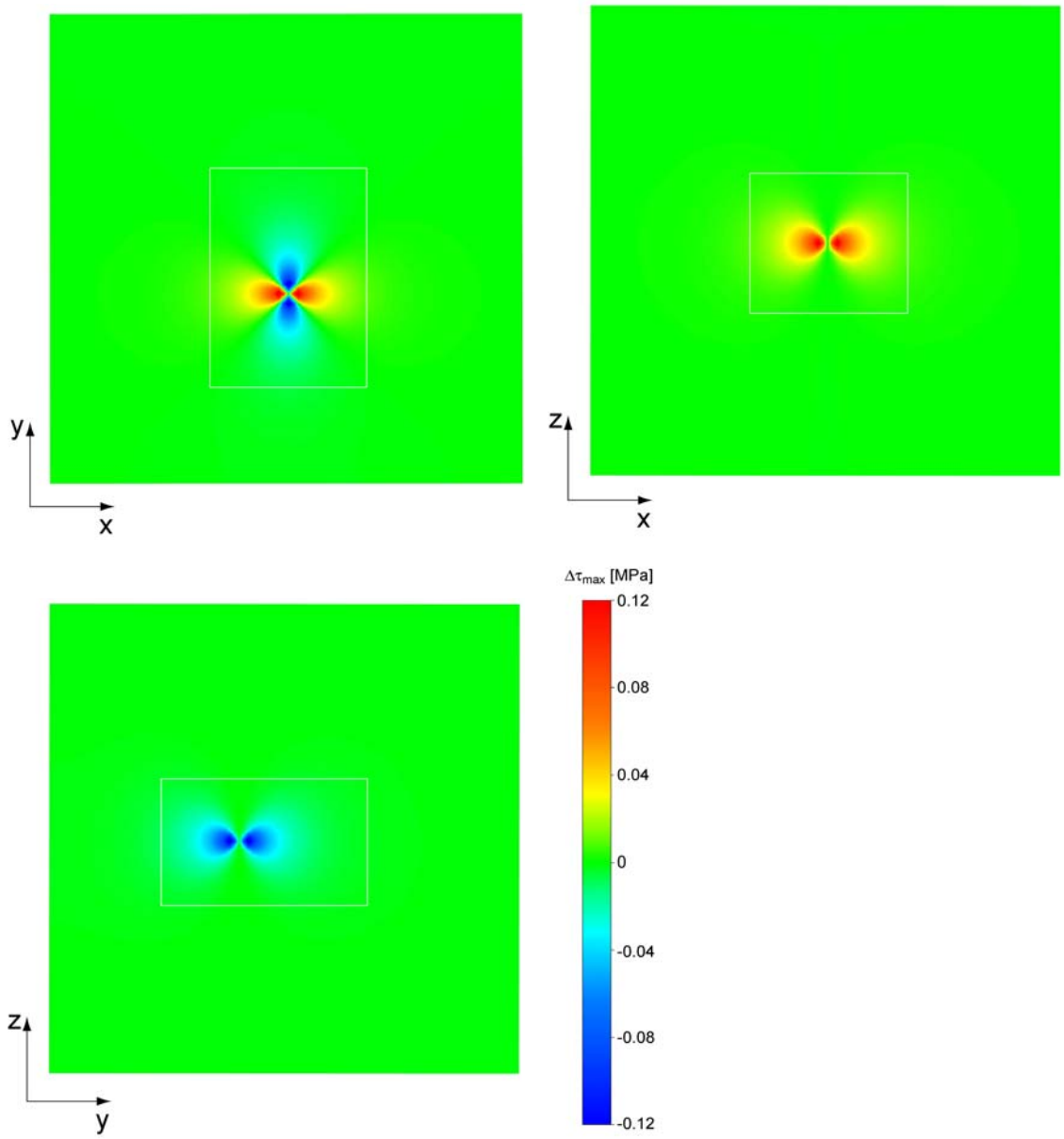

Figure 5-31. Spatial distribution of maximum shear stress in a strike-slip regime on three different cross-sections trough the injection point after 23 days of continuous fluid injection. Note the different orientations of the cross-sections.

The distributions are similar to those of the normal faulting regime (Figure 5-29). There is no difference in the maximal magnitude of $\Delta\tau_{max}$. Different are the directions, in which positive maximum shear stress changes occur. $\Delta\tau_{max}$ is positive in x-direction or σ_H-direction, negative in y-direction or σ_h-direction, and zero in z-direction or σ_V-direction. In comparison with the normal faulting regime results, the directions of positive and zero maximum shear stress change have exchanged. Again, this means that the spatial occurrence of induced seismicity is a function of the tectonic stress regime.

5.5.4 Interpretation

Pore pressure and stress

ΔP (Figure 5-25) shows a spherical distribution inside the reservoir as long as the boundary is not reached, while ΔP is decreasing with distance from the injection point. The shape of the reservoir has only small impact on the ΔP distribution compared to the inhomogeneous axis-symmetric model (Figure 5-6). The reason is that the cuboidal shape of the reservoir is less striking and more similar to a sphere than the ellipsoidal reservoir of the axis-symmetric model. Because ΔP is diffusing spherically in homogeneous media, the ΔP distribution is weakly influenced by the cuboidal sphere-similar shape. Nevertheless, the permeability contrast between reservoir and surroundings affects the ΔP distribution locally. The larger permeability of the reservoir leads P to diffuse faster inside the reservoir, the lower permeability of the surroundings slows down the pore pressure diffusion process into and in the surroundings, leading ΔP to decrease strongly within short distance around the reservoir boundary. This can be seen at the boundaries in vertical direction of the injection point. These boundaries are closer than the other ones, so that pore pressure perturbation arrives these boundaries first, and pore pressure change there is larger than at the other boundaries after the same injection time. As pore pressure diffusion is slowed down in the surroundings, fluid is accumulating inside the reservoir, what leads to a pore pressure build-up inside the reservoir with duration of injection. The higher permeability of the reservoir causes pore pressure changes to spread out faster inside the reservoir than inside the surroundings. After 259 days of fluid injection, pore pressure is diffused wider in y-direction than in z-direction.

At the injection point stress changes are maximal and decline with increasing distance to the point source, for constant time. With duration of injection stress changes spread out and increase at constant location. The normal stress changes show a preferential direction of propagation depending on the direction of the normal stress component, e.g. $\Delta\sigma_{xx}$ in x-direction. These are also the directions, in which normal stresses are radial stresses. σ_{xx} is radial stress in x-direction and tangential stress in y- and z-directions. Therefore, this propagation behaviour can be explained by pore pressure stress coupling. As the coupling is strongest in radial direction and weakest in tangential direction, the radial stress changes, e.g. $\Delta\sigma_{zz}$ in z-direction with respect to the injection point, are larger than the tangential stress changes, e.g. $\Delta\sigma_{zz}$ in x- or in y-direction with respect to the injection point. Therefore, at the same distance to the injection point, radial stress changes are higher than tangential stress changes. This can be seen clearly after longer injection times, when the stress changes have spread out wider. The influence of the reservoir shape, i.e. of the permeability contrast between reservoir and surroundings, can still be observed, but it is superposed by the effect that the stress components are affected differently strong in different directions.

Change in maximum shear stress $\Delta\tau_{max}$

Fluid injection induced maximum shear stress changes in a normal faulting regime show that $\Delta\tau_{max}$ has its positive maximum in the direction of the maximum principal stress σ_V. In the direction of σ_H (x-direction) no $\Delta\tau_{max}$ changes occur. In σ_h-direction (y-direction) $\Delta\tau_{max}$ shows its negative maximum. This is consistent with the results of the analytical investigation (chapter 4.2). They show that fluid injection induced stress changes lead to increasing differential stresses in direction of the maximum principal stress (σ_V in a normal faulting regime), to zero differential stress changes in direction of the intermediate principal stress (σ_H in a normal faulting regime), and to negative differential stresses in direction of the minimum principal stress (σ_h in a normal faulting regime).

The temporal evolution of the $\Delta\tau_{max}$ distribution shows that already after short injection time $\Delta\tau_{max}$ is almost maximal. With duration of injection $\Delta\tau_{max}$ spreads out from the injection point, increasing its maximal magnitude only slightly. This also is in agreement with the analytical results (chapter 4.2), where it is shown that for short injection times the differential stress changes are strongest. On the contrary, pore pressure change is smallest for short injection times. Therefore, shortly after start of injection, the difference in the coupling between P and the stress components have the biggest influence on the rock stability. After 3 days of injection $\Delta\tau_{max}$ and ΔP are in the same order of magnitude in the area of maximal $\Delta\tau_{max}$. For longer injection times ΔP increases much more than $\Delta\tau_{max}$, thus the inhomogeneous pore pressure stress coupling effect becomes less important compared to the effect of ΔP on the effective stresses.

Influence of tectonic regime on $\Delta\tau_{max}$

Fluid injection into a strike-slip regime shows that the direction, in which maximal and minimal $\Delta\tau_{max}$ occur, exchanges. $\Delta\tau_{max}$ now is maximal in x- or σ_H-direction and zero maximum shear stress change is observed in z- or σ_V-direction. This exchange happens due to the change in tectonic regime. According to the theory, $\Delta\underline{\tau}_{max}$ is maximal in maximum principal stress direction, and zero in intermediate principal stress direction. Therefore, the directions has to exchange with a change from normal faulting regime to strike-slip regime. Thus, the modelling results validate the theory.

Summing up, pore pressure stress coupling generates fluid injection induced stress changes, which lead to areas of increased and decreased differential stress changes and therefore maximum shear stress changes. The orientation, maximal and minimal shear stress changes occur, depends on the tectonic stress regime. In a normal faulting regime, the area, where poroelastic coupling has the biggest influence on the rock stability is above and below the injection point (σ_V-direction), in strike-slip or thrust faulting regimes horizontally of the injection point in σ_H-direction.

6 Application to real reservoir geometry

So far, the analytical and numerical investigations of pore pressure stress coupling show that numerical results match the analytical solutions, and numerical and analytical results are consistent. Therefore, in the next step poroelasticity is applied to a model with more complex geometry representing the structure of an reservoir. Under fluid extraction the poroelastic coupling between pore pressure and stress changes is modelled and analysed. Observed borehole breakout orientations derived from logging data along nine boreholes within the model volume are used to calibrate the numerical model. This is done by comparison of modelled and measured borehole breakout orientations at the locations the borehole breakouts were observed in the field.

6.1 Borehole breakouts

6.1.1 Definition

Drilling of a borehole means removing material from the subsurface which cannot support the surrounding rock anymore longer. In a consequence the state of stress is changing in the surroundings of the wellbore and concentrating at the borehole wall. When the circumferential stress around the wellbore wall exceeds the compressive strength of the rock, shear failure occurs on conjugate failure planes, which causes pieces of the borehole wall to spall off (Zoback et al., 1985; Bell, 1990). These stress-induced enlargements of the wellbore cross section are called borehole breakouts (Bell and Gough, 1979; Tingay et al., 2005). Figure 6-1 shows the result of a lab experiment simulating borehole breakouts around a hollow cylinder. The stress concentration around the cylinder wall leads to breakouts and an elongation in σ_h-direction.

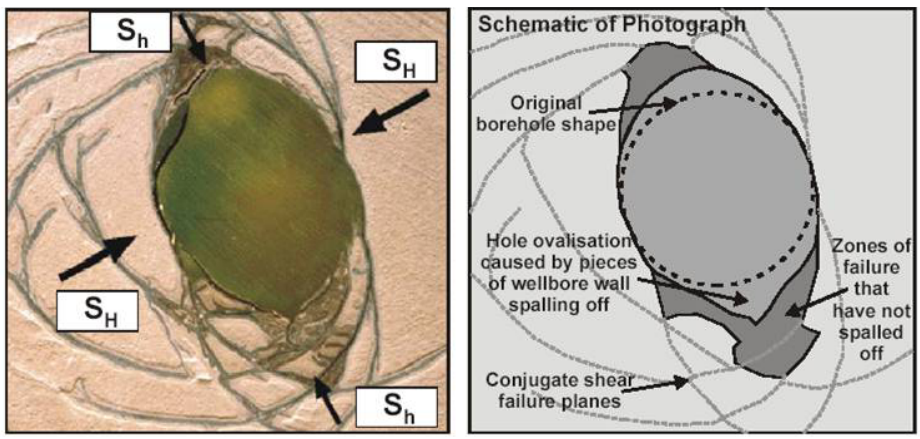

Figure 6-1. Borehole breakouts around a hollow cylinder, performed by CSIRO, Division of Geomechanics, in a lab test. Breakouts occur in σ_h-direction, perpendicular to σ_H.

Kirsch (1898) derived equations in polar coordinates for the stresses around a circular hole with radius a (Figure 6-2), depending on the principal stresses, σ_H, σ_h, that act

orthogonal to the axis of the hole, the azimuth ϑ with respect to the direction of σ_H, the distance r from the centre of the hole ($r \geq a$), and the fluid pressure p in the hole (Zheng et al., 1989). According to Jaeger et al. (2007), the circumferential stress around the wellbore $\sigma_{\vartheta\vartheta}$, which is responsible for the possible occurrence of borehole breakouts (Tingay et al., 2005), is given by

$$\sigma_{\vartheta\vartheta} = \frac{\sigma_H + \sigma_h}{2}\left(1 + \frac{a^2}{r^2}\right) - \frac{\sigma_H - \sigma_h}{2}\left(1 + 3\frac{a^4}{r^4}\right)\cos 2\vartheta - p\,. \qquad (6.1)$$

$\sigma_{\vartheta\vartheta}$ is varying with the azimuth ϑ around the hole according to $\cos 2\vartheta$. As the cosine is a function of 2ϑ, $\sigma_{\vartheta\vartheta}$ is π-periodic, i.e. $\sigma_{\vartheta\vartheta}$ has two maxima and two minima between $0 \leq \vartheta \leq 2\pi$. The minimum value of $\sigma_{\vartheta\vartheta}$ is given by $\sigma_{\vartheta\vartheta,min} = 3\sigma_h - \sigma_H - p$ for $\vartheta = 0$ and $\vartheta = 2\pi$. The maximum value of $\sigma_{\vartheta\vartheta}$ is given by $\sigma_{\vartheta\vartheta,max} = 3\sigma_H - \sigma_h - p$ for $\vartheta = p/2$ and $\vartheta = 3\pi/2$ (Zheng et al., 1989).

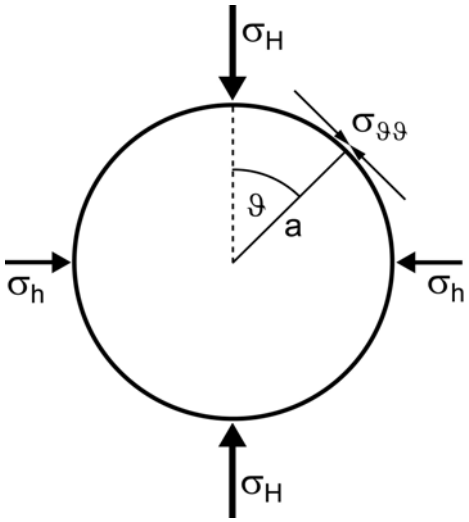

Figure 6-2. Circumferential stress $\sigma_{\vartheta\vartheta}$ at the wall of a circular hole with the radius a, induced by the horizontal principle stresses σ_H and σ_h acting orthogonal to the wall of the hole. The angle ϑ gives the direction of $\sigma_{\vartheta\vartheta}$ at the wall of the hole with respect to the direction of σ_H.

A borehole breakout will occur if $\sigma_{\vartheta\vartheta}$ exceeds the compressive strength of the rock. According to the equations of $\sigma_{\vartheta\vartheta,max}$ and $\sigma_{\vartheta\vartheta,min}$ above, $\sigma_{\vartheta\vartheta}$ is maximal in σ_h-direction and minimal in σ_H-direction. Therefore, borehole breakouts will occur in σ_h-direction, if $\sigma_{\vartheta\vartheta}$ exceeds the compressive strength of the rock.

Figure 6-3 illustrates the variation of $\sigma_{\vartheta\vartheta}$ with the azimuth ϑ around a circular hole, and thus the angular range in which borehole breakouts would occur, under the assumption of principal stresses $\hat{\sigma}_H$ and $\hat{\sigma}_h$ normalized to σ_h, with $\hat{\sigma}_H = 1.6$ and $\hat{\sigma}_h = 1.0$. Then, for zero fluid pressure p, the variation of $\sigma_{\vartheta\vartheta}$ with ϑ is calculated by Eq. 6.1. Under this constellation, $\sigma_{\vartheta\vartheta,max} = 3.8$ for $\vartheta = \pm 90°$, i.e. in direction of σ_h, and $\sigma_{\vartheta\vartheta,min} = 1.4$ for $\vartheta = 0°$, i.e. in σ_H-direction. To define a criterion for the occurrence of borehole breakouts, the compressive strength of the rock, normalized to σ_h, is set to 3.4. Then, $\sigma_{\vartheta\vartheta}$ exceeds the compressive rock strength in σ_h-direction ±25°.

This example points out the stress concentration at the wall of a circular hole. For the considered case, $\sigma_{\vartheta\vartheta,min}$ is by a factor of 1.4 larger than σ_h, and $\sigma_{\vartheta\vartheta,max}$ even is by a factor of 2.375 larger than σ_H. The ratio σ_H/σ_h is the key parameter for the stress concentration around a circular hole. For an isotropic stress state, i.e. $\sigma_H/\sigma_h = 1$, $\sigma_{\vartheta\vartheta}$ is constant around the hole and has twice the magnitude of the far field stress. The larger σ_H/σ_h the larger the difference between $\sigma_{\vartheta\vartheta,max}$ and $\sigma_{\vartheta\vartheta,min}$ and the larger the magnitude of the maximum circumferential stress, and therefore the likelihood for borehole breakouts to occur.

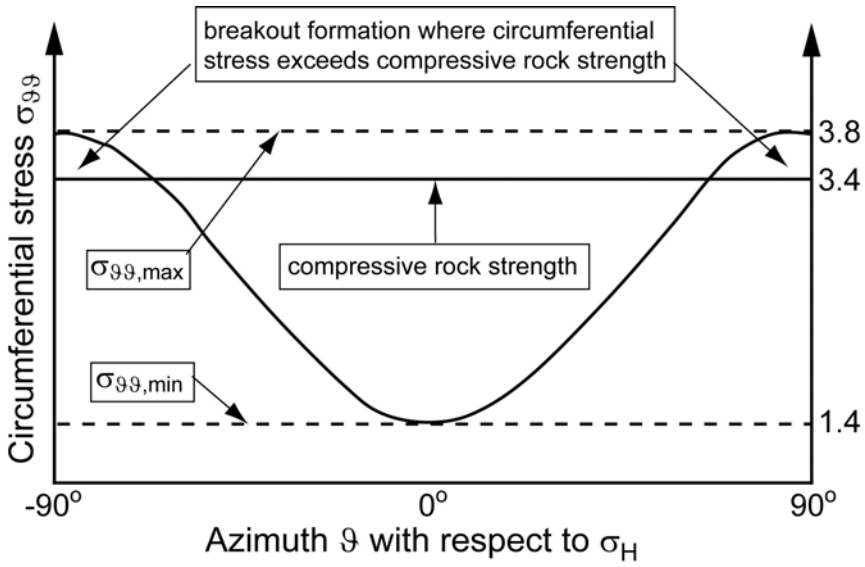

Figure 6-3. $\sigma_{\vartheta\vartheta}$ at the wall of a circular hole, depending on azimuth ϑ. Principal stresses σ_H and σ_h are acting at the wall of the hole. In this example, stresses normalized to σ_h were chosen with σ_H/σ_h = 1.6 and σ_h/σ_h = 1.0. Then, $\sigma_{\vartheta\vartheta,min}$ = 1.4 and $\sigma_{\vartheta\vartheta,max}$ = 3.8, according to Eq. 6.1. Figure is modified after Hillis and Reynolds (2000).

6.1.2 Application to reservoir model

A stress field, represented by the principal stresses σ_H and σ_h, generates a circumferential stress at the wall of a circular hole with a wide range of variation depending on the ratio σ_H/σ_h. (Figure 6-3). Theory (Kirsch, 1898) shows that borehole breakouts occur in the direction of σ_h. This means, that the direction in which borehole breakouts occur, and the direction of the horizontal principal stresses are connected to each other. Therefore, measuring stress-induced borehole breakouts are an important indicator for the direction of the principal stresses (Bell and Gough, 1979; Hickman et al., 1985; Plumb and Cox, 1987; Barton et al., 1988). Zoback and Zoback (1988) show that breakout orientations observed in the upper crust and independent stress measurements correlate to each other, and conclude that borehole breakouts give reliable stress orientations (Barton et al., 1988).

Hence, borehole breakouts and the determination of the directions of the maximum and minimum horizontal stresses can be used as a parameter to calibrate the state of stress of a geomechanical model. The state of stress in a geomechanical model, which is a superposition of gravitational stress and tectonic stress, can be calculated at locations in the model, where borehole breakouts are observed in reality. Using the modelled state of stress, the orientation of the horizontal principal stresses can be calculated and compared to the directions of observed borehole breakouts.

In this case here, the geometries themselves of the boreholes are not included in the geomechanical reservoir model. This means that the local influence of the borehole on the surrounding stress field cannot be determined. Element nodes nearest to the wellbore trajectories were projected onto those paths. Hence, virtual wellbore trajectories exist in the model, with distinct points (element nodes) describing the paths of the trajectories. At those element nodes the state of stress is analysed in order to calculate the directions of the minimum horizontal stress. Because the magnitudes of the circumferential stresses are not compared to the compressive rock strength, the directions of the minimum horizontal stresses give the orientation of potential borehole breakouts. This means, if the circumferential stress would exceed the compressive rock strength at the analysis points, then the direction of a borehole breakout would be given by the calculated direction of the minimum horizontal stress.

In the end, by modification of boundary conditions applied to the geomechanical reservoir model, the state of stress changes and the modelled stress orientations can be adjusted to the observed breakout orientations. This procedure is used to calibrate the given geomechanical reservoir model.

6.1.3 Borehole breakouts along inclined wellbores

So far, a planar circular hole was considered, so that Kirsch's (1898) equation to calculate the stress concentration around it could be applied. But the equation of Kirsch (1898) is also valid for a vertical hollow cylinder, what is nothing else than a circular hole extended in vertical direction, which can represent a vertical borehole. Therefore, Kirsch's equation can be used to calculate the stress concentration and thus the potential breakout orientation around a vertical borehole.

In general, boreholes are not always drilled vertically, but more or less deviated from the vertical and with changing directions, in order to drill around obstructions to reach oil and gas reservoirs. Hydrocarbon industry uses directional drilling, because it is more efficient and more economic (Cooper, 1994). In deviated wells with complex trajectories, the principal stresses are not aligned with the wellbore axis. Thus, it is necessary to have techniques to determine the stresses along such wellbores (Zoback et al., 2003).

Peska and Zoback (1995) have investigated breakout directions in inclined wellbores for different tectonic regimes, i.e. under different stress states. They show that the breakout orientation is strongly dependent on the current state of stress and the inclination and orientation of the wellbore. In consequence, Peska and Zoback (1995) and Zoback et al. (2003) derived a mathematical description to transform the state of stress given from a global geographical coordinate system into a local coordinate system orientated along the however changing wellbore trajectory. Figure 6-4 shows the local wellbore coordinate system, x_b, y_b, z_b, which is aligned along the wellbore and rotated by the angles α an φ from the global geographical coordinate system, X (north), Y (east), Z (down).

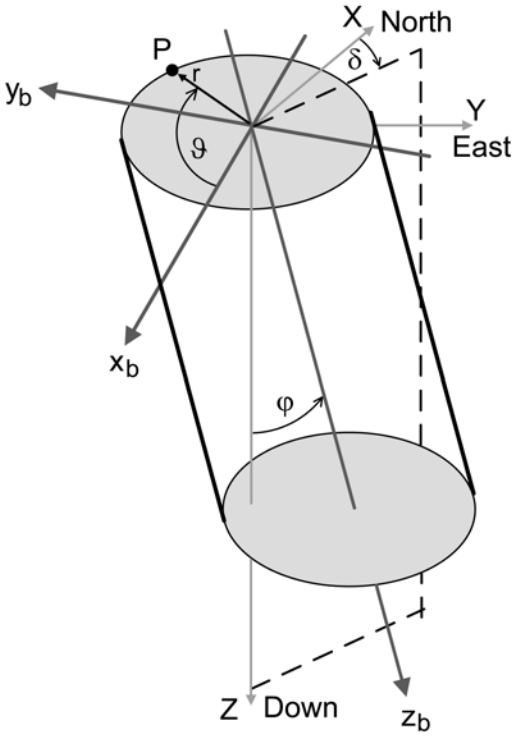

Figure 6-4. Local rectangular borehole coordinate system, x_b, y_b, z_b, for an inclined wellbore with respect to a global geographical coordinate system, X, Y, Z. The position of a point P at the borehole wall can be expressed in terms of the local wellbore coordinate system, rotated by δ and φ with respect to the global coordinate system. Figure modified after Peska and Zoback (1995).

Peska and Zoback (1995) describe the transformation of a principal stress tensor (σ_1, σ_2, σ_3) from a geographical coordinate system (X, Y, Z) into a local wellbore coordinate system (x_b, y_b, z_b). The transformation is done by multiplication of the principal stress tensor with rotation matrices:

$$\sigma = R_b R_S^T \sigma_S R_S R_b^T \tag{6.2}$$

σ is the stress tensor in the wellbore coordinate system, σ_S is the principal stress tensor, R_b and R_S are rotation matrices, the superscript T indicates the transpose of a matrix. According to Peska and Zoback (1995) R_b and R_S are given as:

$$R_b = \begin{pmatrix} -\cos\delta\cos\varphi & -\sin\delta\cos\varphi & \sin\varphi \\ \sin\delta & -\cos\delta & 0 \\ \cos\delta\sin\varphi & \sin\delta\sin\varphi & \cos\varphi \end{pmatrix} \tag{6.3}$$

$$R_S = \begin{pmatrix} \cos\alpha\cos\beta & \sin\alpha\cos\beta & -\sin\beta \\ \cos\alpha\sin\beta\sin\gamma - \sin\alpha\cos\gamma & \sin\alpha\sin\beta\sin\gamma + \cos\alpha\cos\gamma & \cos\beta\sin\gamma \\ \cos\alpha\sin\beta\cos\gamma + \sin\alpha\sin\gamma & \sin\alpha\sin\beta\cos\gamma - \cos\alpha\sin\gamma & \cos\beta\cos\gamma \end{pmatrix} \tag{6.4}$$

δ is the azimuth of the horizontal projection of the wellbore measured clockwise from geographic north (X) and φ is the angle between the borehole axis and the vertical (Figure 6-4). α, β, γ are rotation angles to transform the geographic coordinate system (X, Y, Z) via the systems (X', Y', Z') and (X'', Y'', Z'') into a system aligned to the principal stresses σ_1, σ_2, σ_3. In particular, α describes a positive rotation about the Z-axis, β a positive rotation about the Y'-axis and γ a positive rotation about the X''-axis.

Based on this transformation (Eq. 6.2), the stresses around an arbitrarily inclined and orientated wellbore can be calculated by Kirsch's (1898) equations. Knowing the circumferential stress $\sigma_{\vartheta\vartheta}$ along the wellbore trajectory, the direction of potential borehole breakouts, which is equal to the direction of maximum circumferential stress, can be determined and compared to observed breakout orientations. This procedure is used in this thesis to calibrate the geomechanical model.

For this purpose, a matlab program was written, transforming the stress tensor given in a geographic coordinate system into a local wellbore coordinate system. This program uses a transformation based on Eq. 6.2, determines the circumferential stress $\sigma_{\vartheta\vartheta}$ in the local wellbore coordinate system, the direction of maximum $\sigma_{\vartheta\vartheta}$, and compares this direction with the orientation of observed borehole breakouts. For a more detailed description of the structure of the matlab program, see Appendix C.

6.2 FE model

A 3D finite element reservoir model was set up, and two different rheologies applied to the model in two steps. At first, a linear elastic rheology was used to model the static state of stress in the model area, and calculate potential borehole breakout orientations caused along wellbores inside the model volume by the acting stress state. These modelled potential borehole breakout orientations are used to calibrate the model by comparison with observed borehole breakout orientations. In a second step, poroelastic rheology was applied to the model to simulate reservoir depletion induced coupled pore pressure and stress changes and their influence a reorientation of the stress field. For both rheologies the same model geometry and same mesh was used.

6.2.1 Model generation

To set up a finite element model, a few step are required. Here, I give a brief description of the softwares I have used during the model generation process, and for what kind of purpose they were used.

The model was built up by the use of different software packages. The stratigraphic layers, and therefore the structure of the reservoir was given in Gocad. This software was used to define the model volume and to generate the final geometry of the model. The geometry was exported as surfaces and imported into HyperMesh. With this tool the model volume was discretised by finite elements. Also nodes and elements were defined, boundary conditions later are applied on. Finally, the finite element model was exported as a text file, the so-called Abaqus input file, with all information about the geometry of the model. Then, this text file was edited in order to assign the correct element type to the elements, to define material properties, to apply boundary conditions and initial conditions to the model, and to generate the calculation step. Then Abaqus was used as solver for the numerical problem.

6.2.2 Model setup

The reservoir model consists of ten anticlinal layers with decreasing flexure from the bottom to the top (Figure 6-5). Eleven wellbores are located in the model area (Figure 6-6). The wellbores themselves are not included as part of the model. Only the wellbore trajectories are imported into the model, to project element nodes onto the trajectories in order to calculate results at exact wellbore path locations. This is necessary, as the only parameter to calibrate the model, are orientations of borehole breakouts, which occurred along those wellbores paths.

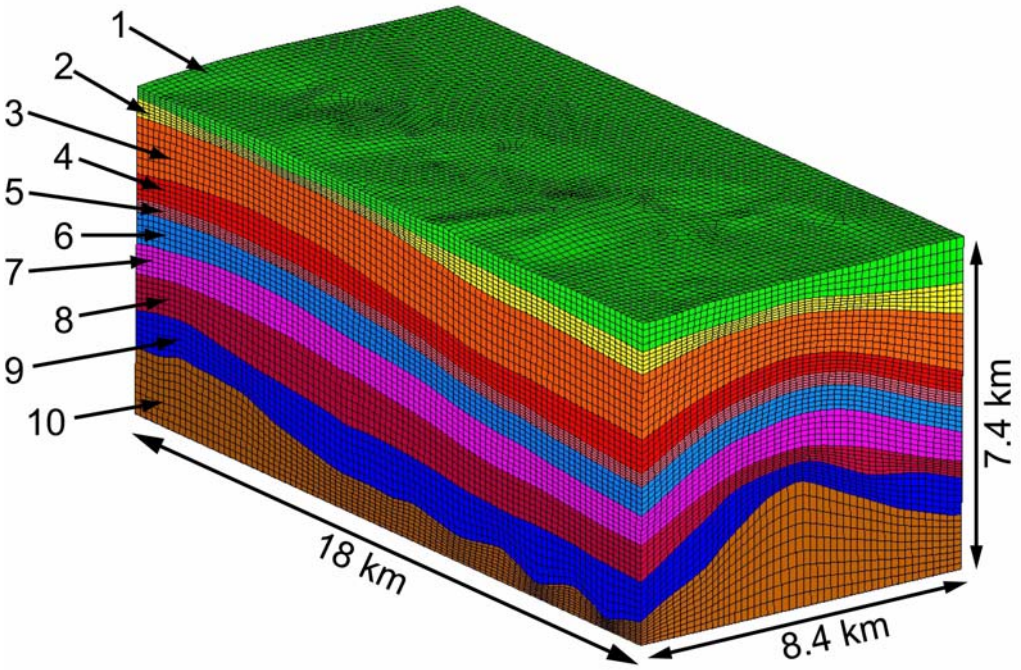

Figure 6-5. Setup of the 3D finite element model of an oil reservoir, consisting of ten layers, which are named from the top to the bottom by the numbers 1 to 10. The productive series are located in layer 6, in depths between of ca. 2.4 and 3.8 km. This model setup is used for both, elastic and poroelastic rheology with changing material parameters between the layers. The entire model volume is meshed by 263088 hexahedral elements with an average resolution of 120 m in vertical direction and of 200 m in horizontal direction.

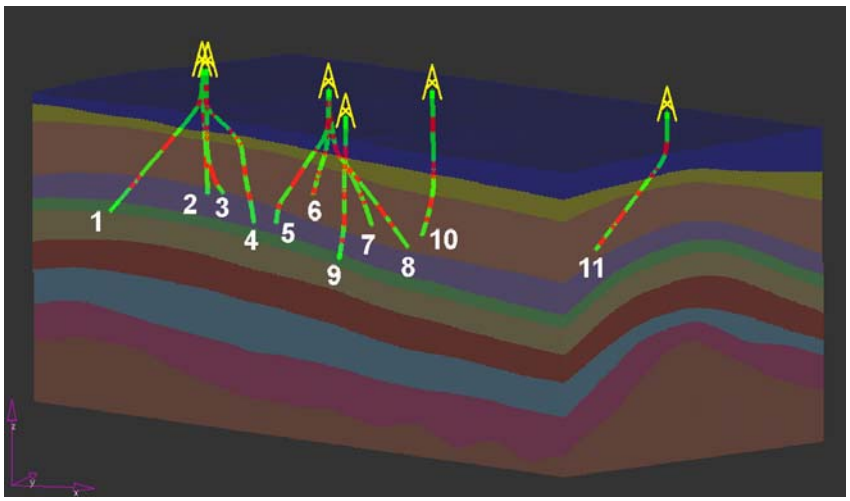

Figure 6-6. Wellbore trajectories inside the model area. The wellbores themselves are not included in the model geometry. Element nodes are projected onto the wellbore trajectories, and thus are describing the wellpaths of the eleven wellbores in the model volume. Results are then calculated at those wellpaths element nodes.

6.3 Elastic material properties

At first, a linear elastic material properties were used to model the static elastic field of stress, and to calculate potential borehole breakout orientations along the wellbore trajectories generated by the stress field. The modelled borehole breakout orientations are compared to observed ones, in order to calibrate the numerical model.

6.3.1 Material parameters

The linear elastic rheology is fully described by a set of two material parameters. Most common, the pairs Young's modulus E and Poisson's ratio ν, or first and second Lamé parameters λ and μ, respectively, are used. The Lamé parameters can be calculated from the wave velocities and the mass density. According to Mavko et al. (2009), the P-wave and S-wave velocities can be expressed by:

$$v_S = \sqrt{\frac{\mu}{\rho}} \qquad v_P = \sqrt{\frac{\lambda + 2\mu}{\rho}} \tag{6.5}$$

Knowing the wave velocities and the density, the Lamé parameters are determined. Velocity logs and density logs of eleven wellbores inside the model volume are provided (Figure 6-7). Then the two Lamé parameters can be determined by Eqs. 6.5. E and ν, which are required as Abaqus input for the numerical modelling, can be expressed by λ and μ (Birch, 1961):

$$E = \mu \frac{3\lambda + 2\mu}{\lambda + \mu} \qquad \nu = \frac{\lambda}{2(\lambda + \mu)} \tag{6.6}$$

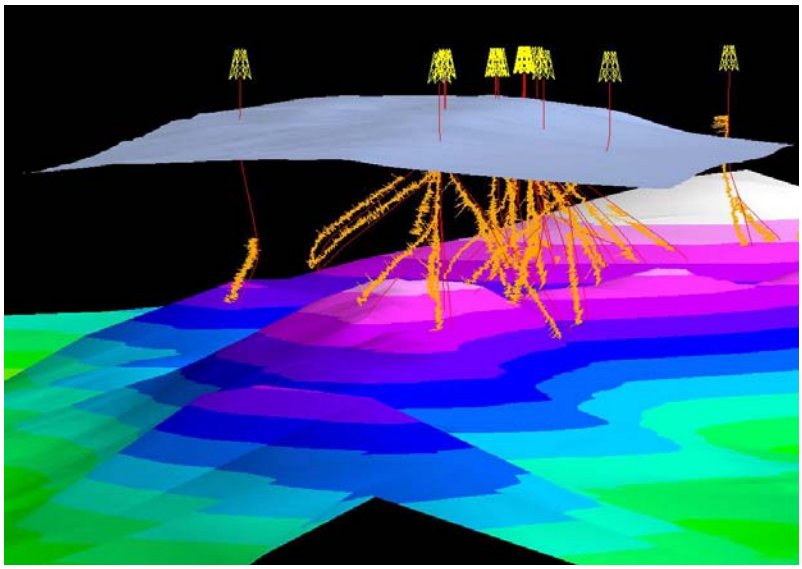

Figure 6-7. Velocity and density logs of the eleven boreholes inside the model volume are were provided to calculate Young's moduli and Poisson's ratios.

No well-log data are available for the uppermost Layer 1, and well-log data of only one wellbore for Layer 2. All eleven wellbores end in layer 6, this means that only for Layer

2 to Layer 6 E and ν values can be derived from the velocity and density logs. The elastic material parameters of the four deepest layers are estimated by extrapolating the values of the upper layers. E and ν are calculated from the velocity and density logs by combining Eqs. 6.5 and 6.6. Figure 6-8 shows the variation of E and ν with depth along one of the eleven wellbores. E increases and ν decreases with depth. Therefore, both values are not constant within the each layers, but increase or decrease, respectively, more or less strongly.

On the one hand it is helpful to have detailed information of material parameters and their spatial variation inside the model area; on the other hand one has to decide how this information can be included into a numerical model. Three facts have led to the decision to include E and ν as constants of each layer:

1) Young's modulus as well as Poisson's ratio vary not with constant gradient with depth, but show a zigzag curve with extending range in deeper layers. E, for example, is oscillating by ± 1 MPa in Layer 2, and by ± 3 MPa in Layer 6, i.e. ± 25%, around the average.

2) E and ν vary differently with depth along different wellbores. Figure 6-9 shows the variation of E and ν with depth of another wellbore, where the layers are deeper than in the case of Figure 6-8. Then, for the same layer E is larger and ν is smaller in the case of Figure 6-9. This means that the depth is influencing the E and ν distribution strongly.

3) Information about E and ν distribution inside the model volume is available only along the wellbores, i.e. in a very distinct area. For the rest of the model volume, no information about the E and ν distribution is available.

Due to the lack of information about Young's modulus and Poisson's ratio in a large part of the model volume, and the fact that both parameters change differently along different wellbores, the decision was made to use constant values for E and ν for each layer, which increase and decrease with depth, respectively, and represent an average of all values of the same layer.

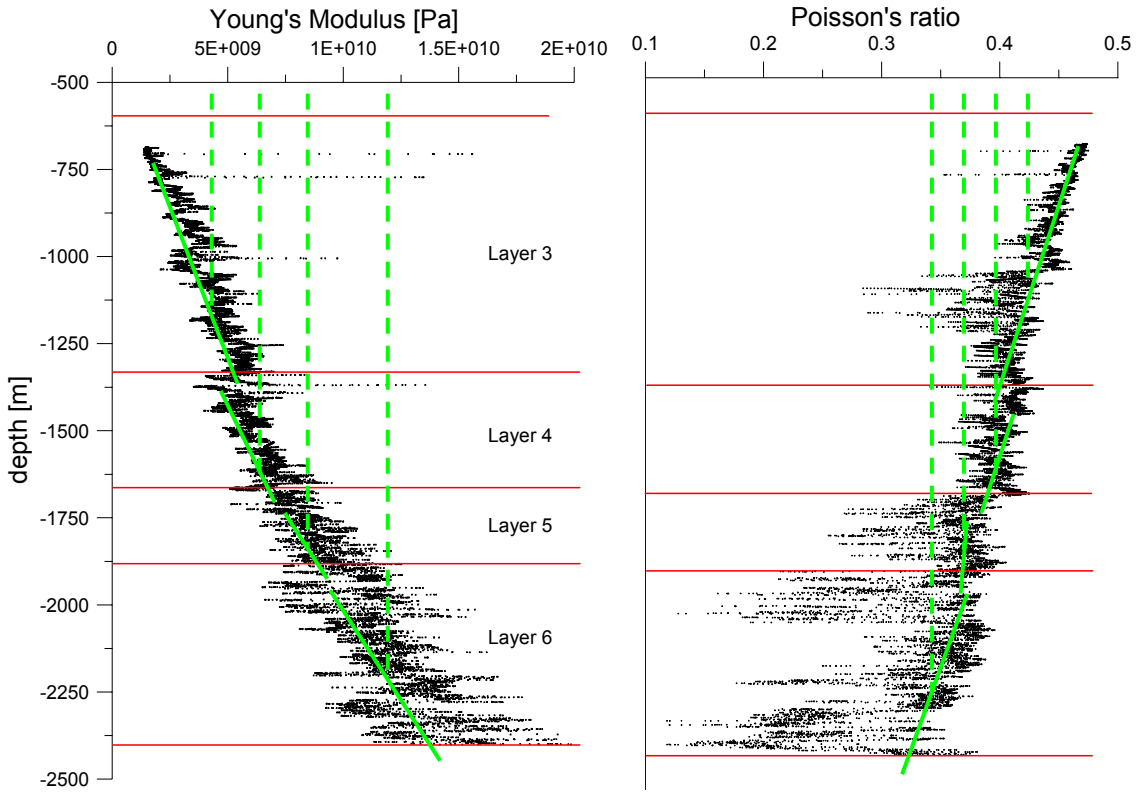

Figure 6-8. Young's modulus (left) and Poisson's ratio (right) versus depth, derived from velocity- and density-log data of one of the eleven wellbores inside the model area. Both parameters vary with depth and within each layer. To find proper E and ν values for each layer, straight lines (green solid lines) are drawn and the average values of these lines (green dashed lines) are taken as representative values of these layers.

Table 12 shows an overview of the density, the Young's modulus and the Poisson's ratio calculated from the density and velocity logs along the eleven wellbores inside the model volume. In the last column the values used for the numerical model are listed. The density and the Young's modulus increase continuously with depth, whereas the Poisson's ratio decreases. The values of the densities and the elastic properties are typical for mud and shales which are most present in the reservoir area. Schmitt et al. (1989) measure Young's moduli and Poisson's ratios of oil shales with a density between 2240 kg/m^3 and 2310 kg/m^3 in both laboratory tests and field experiments, and determine $E \approx 17$ GPa, $0.25 < \nu < 0.35$ in the laboratory, and 27 GPa $< E <$ 34 GPa in the field. Eseme et al. (2007) give values for the Young's modulus and the Poisson's ratio of oil shale as $E \approx 16$ GPa and $0.2 < \nu < 0.35$. Lonardelli et al. (2007) consider for the investigation of anisotropy in shales soft shale and hard shale with densities of 2210 kg/m^3 and 2510 kg/m^3, respectively. Ahmadov et al. (2009) analyse kerogen as part of shales with a density between 2320 and 2570 kg/m^3, and determine 10 GPa $< E <$ 15 GPa.

As the wellbores of the model area penetrate only the upper six layers, where density and velocity logs were recorded for layers 2 to 6, ρ, E and ν are unknown for layer 1

and layers 7-10. Therefore, the densities, Young's moduli and Poisson's ratios of layers 1 and 7-10 are extrapolated based on the measurements in layers 2-6 (Table 12). Table 13 gives the densities and elastic properties of those five layers.

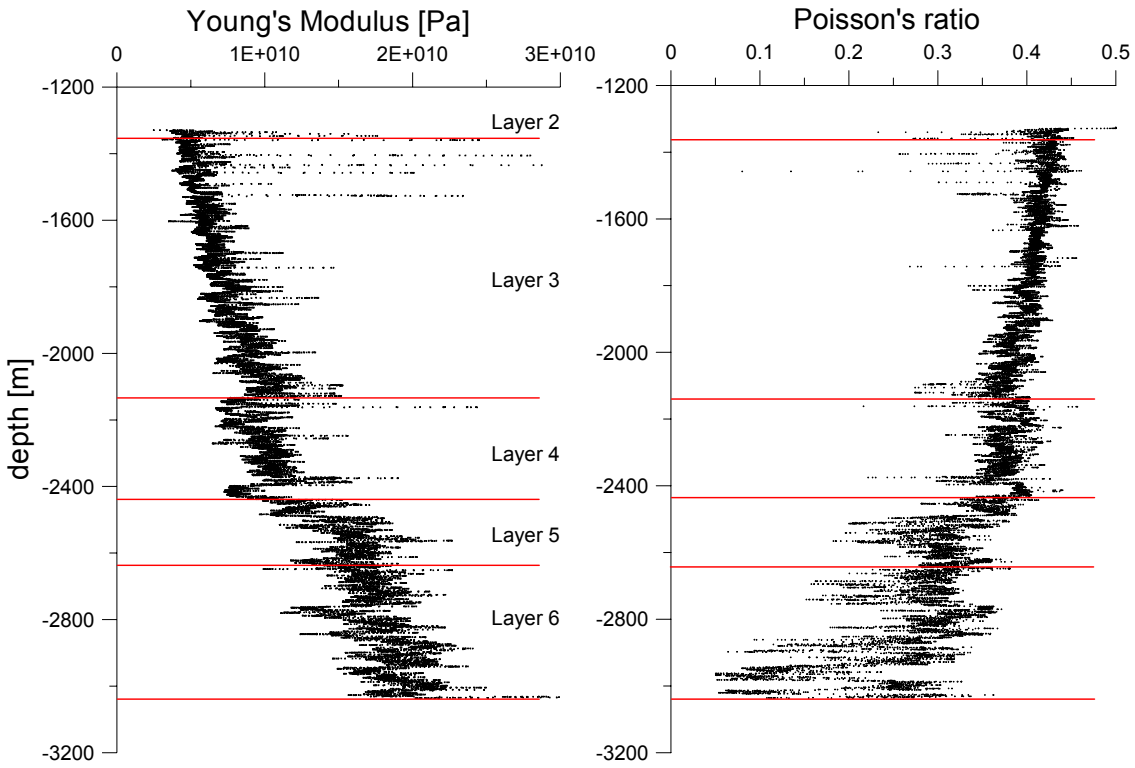

Figure 6-9. Distribution of Young's modulus (left) and Poisson's ratio (right) with depth along another wellbore. *E* is increasing, *ν* decreasing with depth, similar to Figure 6-8. Note the higher Young's modulus values here, which result from the greater depth of the layers along the wellbore here.

Table 12. Elastic material properties (E and ν) of Layers 2 to 6 calculated from velocity and density logs along eleven boreholes (BH). The last column contains the values of each layer used in the numerical model.

		BH1	BH2	BH3	BH4	BH5	BH6	BH7	BH8	BH9	BH10	BH11	Model
Layer 2	ρ [kg/m^3]									2250			2250
	E [GPa]									4.0			4.0
	ν									0.43			0.43
Layer 3	ρ [kg/m^3]	2280	2270			2300	2280			2310			2290
	E [GPa]	4.5	5.5			7.0	8.0			6.5			6.36
	ν	0.41	0.40			0.38	0.38			0.40			0.40
Layer 4	ρ [kg/m^3]	2320	2310	2330	2310	2350	2330	2380	2340	2400	2300		2340
	E [GPa]	6.0	10.0	14.0	5.0	9.5	11.0	16.0	7.5	9.0	10.0		9.78
	ν	0.39	0.35	0.23	0.41	0.36	0.36	0.33	0.40	0.37	0.40		0.36
Layer 5	ρ [kg/m^3]	2350	2370	2380	2330	2370	2340	2390	2380	2400	2350	2320	2360
	E [GPa]	8.0	14.5	16.0	10.0	14.0	15.5	19.0	11.0	15.0	15.0	14.0	13.58
	ν	0.38	0.28	0.24	0.38	0.32	0.30	0.32	0.36	0.32	0.36	0.35	0.32
Layer 6	ρ [kg/m^3]	2370	2380	2400	2350	2390	2360	2410	2410	2420	2370	2350	2370
	E [GPa]	11.5	21.0	18.0	14.0	18.0	19.0	22.5	20.0	18.0	16.0	18.0	17.93
	ν	0.31	0.23	0.27	0.32	0.24	0.28	0.31	0.28	0.27	0.33	0.33	0.28

Table 13. Elastic material properties of Layer 1 and 7-10. The values are extrapolated from Layers 2-6 (Table 12).

Layer	ρ [kg/m^3]	E [GPa]	ν
1	2200	2.0	0.45
7	2400	21.0	0.26
8	2450	28.0	0.24
9	2480	35.0	0.24
10	2550	50.0	0.24

6.3.2 Initial state of stress

Applying the elastic material properties (Tables 12 and 13) to the numerical model, the first modelling step has the goal to receive an initial state of stress. In the following, I describe the procedures and boundary conditions, which were used to obtain the initial state of stress.

The initial state of stress is obtained by applying gravity to the entire model volume. At the beginning no other constraints are applied to the model surface. The other model

boundaries are constrained in normal direction by zero displacement; no constraints are applied to the other degree of freedoms. The gravity leads to a compaction of the model volume in vertical direction due to the weight of the overburden. To avoid this compaction in the order of hundreds of meters, the model is pre-stressed with the state of stress the gravity generates. For this purpose, two calculations are required. In the first model run, the state of stress of the model volume is calculated after applying gravity and generating compaction. Then, this state of stress is exported in a file, and when starting the second model run, it is read in before gravity is applied. Thus, the model is pre-stressed by the state of stress the gravity is generating. In an idealized case, the pre-stressing would lead to zero compaction after the second model run. In reality, the compaction is not zero, because a numerical method includes approximations to obtain a state of equilibrium. Secondly, the state of stress is calculated at the integration points of the model elements, but then for the process of pre-stressing extrapolated to the element nodes. Anyway, in my case the pre-stressing reduced the compaction to the order of ~1 cm, what is sufficiently exact if compared to the model size of 7.4 km in vertical direction.

This is the procedure used to obtain the initial state of stress. With only gravity acting, the vertical stress σ_V represents the load given by the weight of the overburden. As the model sides are fixed in normal direction, the horizontal stresses σ_H and σ_h can be calculated under uniaxial strain conditions by (Turcotte and Schubert, 2002)

$$\sigma_H = \sigma_h = \frac{\nu}{1-\nu}\sigma_V \,. \tag{6.7}$$

With a Poisson's ratio of 0.25, σ_H and σ_h result in $1/3 \cdot \sigma_V$ for a representative number of a crustal rock (Turcotte and Schubert, 2002). Even for Poisson's ratios higher than 0.25, the horizontal stresses are smaller than the vertical stress. This means, the modelled initial state of stress will always represent an normal faulting regime ($\sigma_V > \sigma_H > \sigma_h$), what is not consistent with world-wide observed crustal stress regimes as displayed in the World Stress Map (Heidbach et al., 2008). Calculating the ratio of mean horizontal stress to vertical stress expressed by the k-value

$$k = \frac{\frac{1}{2}\left(\sigma_h + \sigma_H\right)}{\sigma_V}, \tag{6.8}$$

k results in 1/3 for $\nu = 0.25$. Measurements at the drilling sites KTB (Brudy et al., 1997) and SAFOD (Hickman and Zoback, 2004) show that the k-value is much larger than 1/3, approximately 1.0 at a depth of ~ 8 km and increases towards shallower depths. This means that the magnitudes of the horizontal stresses are not only made by the Poisson's ratio effect, but must also be made by an additional effect.

Sheorey (1994) presents an one-dimensional elasto-static thermal earth model to estimate stresses in the earth's crust. In his earth model, Sheorey (1994) considers the

crust, the upper and lower mantle, which he subdivides in several slices. He parameterised his earth model's structure in terms of thermal gradient, thermal expansion coefficient varying with temperature and depth, gravity and elastic constants varying with depth. Sheorey (1994) considers the effects of thermal expansion and gravitational compaction, and empirically derives an expression for the *k*-value for the uppermost kilometres of the crust

$$k = 0.25 + 7E\left(0.001 + \frac{1}{H}\right) \tag{6.9}$$

where E is the Young's modulus [GPa] and H depth [m]. This leads to higher k-values, and thus to higher horizontal stresses close to the surface, as observed (Brudy et al., 1997; Hickman and Zoback et al., 2004; Heidbach et al., 2008). Sheorey (1994) concludes that the curvature of the earth plays the main role for creating higher horizontal crustal stresses close to the surface.

The results of Sheorey's model and the outcome that the curvature of the earth is not negligible concerning horizontal surface-near stresses, can be applied in geomechanical modelling to simulate an initial state of stress. For this purpose, a modelling method was developed at the Geophysical Institute of the University of Karlsruhe, which generates higher horizontal stresses during the calculation of the initial state of stress. The main contributors of this work are Thies Buchmann, Andreas Eckert, Tobias Hergert and Oliver Heidbach. As I did not take part in the development of the method, but only did use it for my modelling applications here, I will briefly describe the method according to Eckert (2007) and Hergert (2009), where a more detailed description can be found. The idea of the method is that a geomechanical model which is the uppermost part of the earth's crust is part of a circle's segment, where the entire circle represents the earth. In general, a geomechanical model has vertical model boundaries, though the borders of such a circle's segments are inclined. To apply the inclined borders to the geomechanical model, a load frame is built around the model and a compaction layer as vertical ending (Figure 6-10). Load frame and compaction layer are a simplification of Sheorey's (1994) spherical layered spherical earth model, in which the equilibrium of thermal expansion and compaction is taking place.

The procedure to find an initial state of stress is to vary the Young's modulus E of the compaction layer, and thus fit the *k*-value depending on depth with the empirical relation of Sheorey (1994) (Eq. 6.9). For the best-fit model, the state of stress is exported and then imported again as initial stress state of the geomechanical model, now without load frame and compaction layer. Starting with this initial stress state, additional modelling steps can be applied to the model volume.

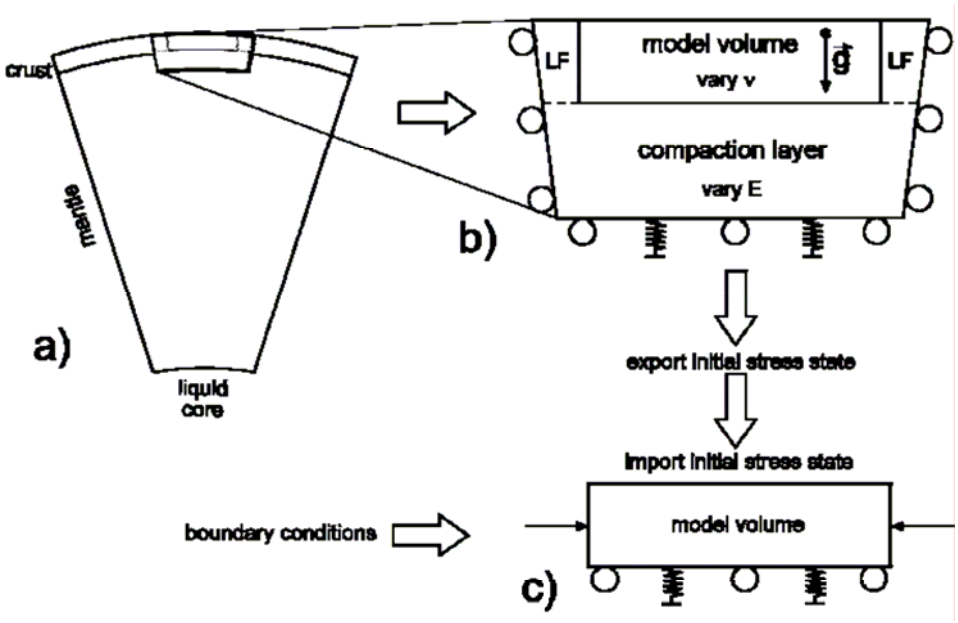

Figure 6-10. Modelling procedure. a) The geomechanical model is the uppermost part of a spherical earth model according to Sheorey (1994). b) Load frame LF and compaction layer around the geomechanical model volume to realize a simplified layered model after Sheorey (1994). By variation of Young's modulus *E* of the compaction layer and Poissons's ratio ν of the load frame the *k*-value can be fitted to the empirical trend (Eq. 6.9). Then the initial state of stress is modelled and exported. c) The initial state of stress can now be imported into the geomechanical model without load frame and compaction layer for further modelling steps. Figure from Eckert (2007).

6.3.3 Model calibration, initial state of stress

Figure 6-11 shows *k*-values of the initial state of stress on a vertical profile of the model volume. Dark grey crosses show the modelling result calculated by taking into account Sheorey's concept, light grey diamonds show the k-values of the initial state of stress of the same model volume calculated conventionally without load frame and compaction layer. The black solid line gives the theoretical *k*-value trend according to Eq. 6.9. The inclusion of a so-called Sheorey-Box (load frame plus compaction layer) to model the initial stress state leads the *k*-values to increase from 0.35 to 0.75 between 3 km and 7 km depth. Furthermore, the *k*-value increases strongly close to the surface, and thus follows the theoretical trend. Therefore, the modelling of the initial state of stress with Sheorey-Box has two advantages concerning the *k*-value, a) it is shifted to the right towards higher values in the diagram and b) it strongly increases approaching the surface.

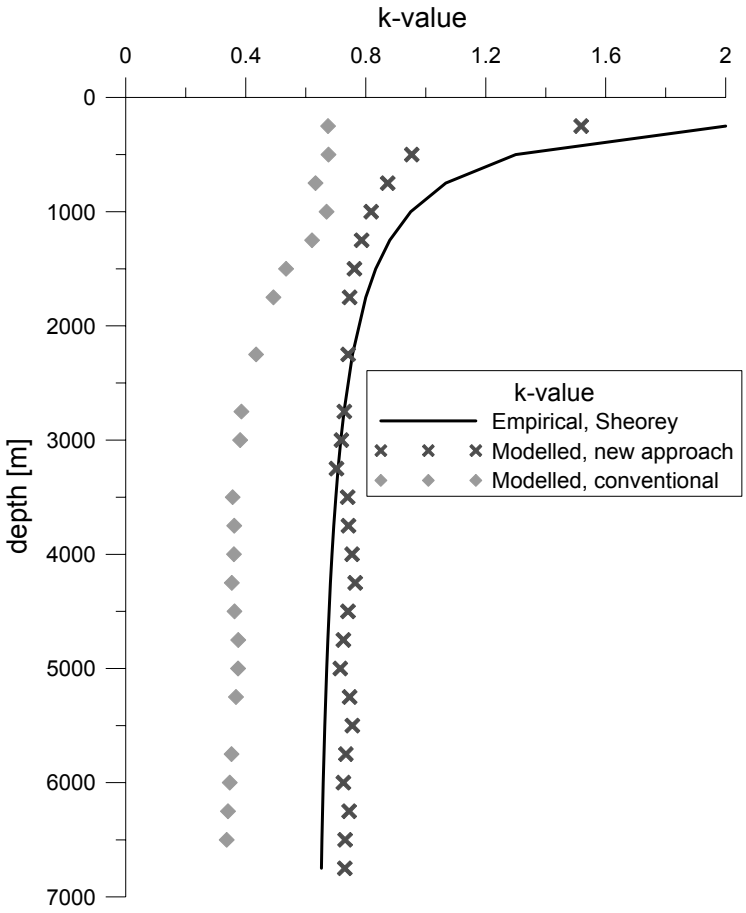

Figure 6-11. Comparison of theoretical (empirical) and modelled k-values. The solid line shows the trend of Sheorey's empirical *k*-values (Eq. 6.9) for *E* = 50 GPa, the dark grey crosses show the results received by the new modelling approach of a load frame and a compaction layer around the model volume, the light grey diamonds represent *k*-values modelled conventionally without load frame and compaction layer.

6.3.4 Model calibration, boundary conditions

In addition to the initial state of stress, displacement boundary conditions, which represent the existence of tectonic stresses, are applied to the geomechanical model. Those boundary conditions modify the state of stress of the model volume, and thus the model can be calibrated by variation of magnitude and direction of the displacement boundary condition, and by comparison of modelled potential breakout orientations and measured borehole breakout orientations. Different magnitudes of displacements acting on different model sides were tested. Figure 6-12 shows the boundary condition which leads to the best analysed match of modelled potential and measured borehole breakout orientations.

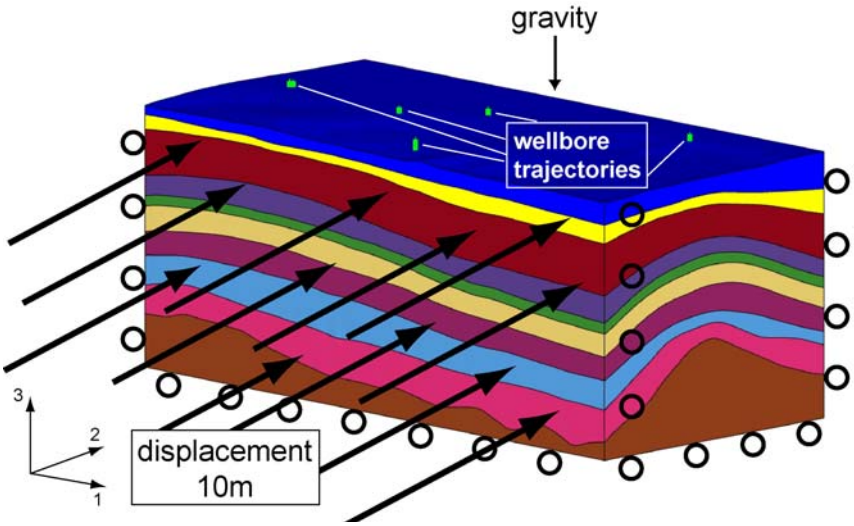

Figure 6-12. On one model side a uniform displacement of 10 m is applied in 2-direction in addition to gravity. The other three model sides and the bottom are fixed in normal direction, no constraints are applied to the surface. The green dots on the surface show the locations of the top end of the wellbore trajectories.

6.3.5 Results

Along two (boreholes 7 and 10) out of eleven boreholes that are implemented in the model as virtual borehole trajectories no borehole breakouts are observed. Measured borehole breakout orientations along borehole 5 show such strong variations, that this borehole is excluded from the comparison of modelling results with measured data.

To define a criterion for the quality of the fit of modelled with measured orientations, at first the mean azimuths and the standard deviations of the measured orientations are calculated. With the number of observed borehole breakouts and the combined length of the breakouts along a single borehole, qualities ranging from A (best) to E (worst) are assigned to the measured orientations, according to the World Stress Map quality ranking system (Heidbach et al., 2008). Depending on the quality, this ranking system gives ranges for the σ_H-orientation or the breakout orientation, in which the σ_H-orientation is believed to be within. The ranges are for quality A: ± 15°, B: ± 15-20°, C: ± 20-25°, D: ± 25-40°, E: > ± 40°. In the following, these ranges are used as criterion for the quality of the match between modelled and measured borehole breakout orientations.

The best match results of modelled and measured borehole breakout orientations are shown in Fig. 6-13. The modelling results along wellbores 1, 6 and 7 fit the measured data quite good. A reasonable match can be found along trajectory 3 for the deeper breakouts and along trajectory 5 for the shallow breakouts. The modelled breakout orientation of trajectory 8 is only a few degrees out of the window given by the WSM criterion. Along trajectories 2 and 4 the modelled potential breakout orientations do not

fit the observed borehole breakout orientations at all. The modelling results differ between 55° and 70° from the measurements.

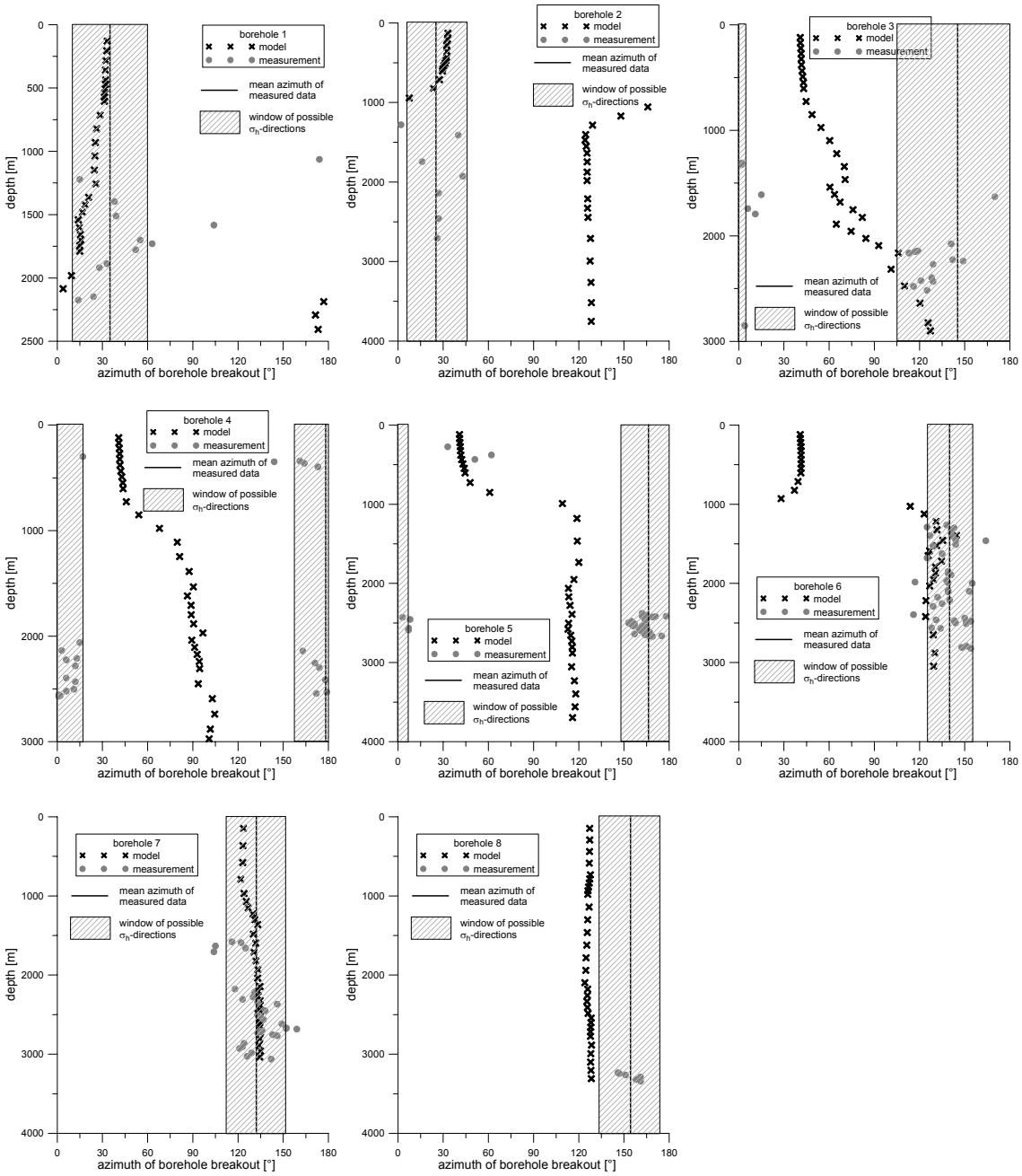

Figure 6-13. Results of the best match of modelled and measured breakout orientations obtained by model setup and boundary conditions as shown in Fig. 6-12. Modelled and measured data are compared for eight wellbores. The solid vertical lines display the mean azimuths of the measured orientations. The grey shaded are shows the range of breakout or σ_h-orientations according to the World Stress Map quality ranking system (Heidbach et al., 2008).

One reason that modelling results and measured data on the one hand along some wellbores show a good match, on the other hand along other wellbores differ enormously, could be the fact that the model exists only of stratigraphic layers. In

reality, the reservoir is also interspersed with fault zones. Faults change the stress orientation, what leads to a different result. The lack of information about the elastic material parameters of several the layers, which had to be extrapolated from other layers, can have an influence on the results. If a layer, for example has a higher Young's modulus than assumed, the applied displacement of 10 m would lead to higher stresses inside this layer and may affect the potential breakout orientation. As under the given circumstances, this is the best result that could be achieved, in the following the stress field of the best fit model is used as initial state of stress in a poroelastic approach.

6.4 Poroelastic rheology

To investigate the influence of reservoir depletion on pore pressure distribution and coupled stress changes, poroelastic material properties are applied to the reservoir model.

6.4.1 Material parameters

As I was not provided any information about poroelastic material parameters for the reservoir model, I have chosen values found in literature. The only value of the logarithmic bulk modulus κ was derived by the Young's moduli and Poisson's ratios that are chosen already for the elastic modelling. Because κ is reciprocal proportional to the drained bulk modulus K_d, that can be calculated by $K_d = E/3(1-2\nu)$, κ was determined under the assumption of an initial void ratio e_0. According to Eq. 5.4, κ also depends on P and the elastic tensile limit p_t^{el}. To avoid changes of κ during the modelling process, where pore pressure will change, the elastic tensile limit was chosen very high, so that is much larger than the pore pressure. p_t^{el} itself does not have any influence on the results. So, an arbitrary value can be chosen for it.

For the grain bulk modulus an average value was chosen. The standard value of the fluid bulk modulus of water is 2.2 GPa. This value increases with salinity of water. K_f for oil ranges around 1.5 GPa. Therefore, I have assumed a fluid bulk modulus of 2 GPa. Stoll (1995), Li (2009) or Mavko et al. (2009) provide some information about the bulk moduli of grains and fluid.

Permeability is a parameter that can vary over a wide range depending on the kind of rock or stone. In granite or shales, for example, the permeability can be as low as tens of micro Darcy, in sand or sandstone as high as one Darcy. Information about permeability values can be found in Bear (1972), or in Buryakovsky et al. (1995) and Bagirov et al. (1999) who provide permeability and porosity data of onshore and offshore oilfields in the South Caspian basin. Additional information about porosity of reservoir rock is given in D'Heur (1984), Santoso et al. (1995), Lucia (1999), Moore (2001), or Ehrenberg and Nadeau (2005). For the porosity I have chosen a constant value for all layers, which ranges at the upper limit of porosities of reservoirs in the South Caspian

basin (Bagirov et a., 1999). Besides the aspect to chose realistic values for the permeability in the model, also the permeability contrast between the layer which is produced of and the surrounding layers is important. Because no faults are included in the model, which could border the producing layer, I have chosen the permeability as parameter to seal the producing layer. Therefore, I have chosen a permeability contrast between producing layer and surrounding layers of ~1000. According to Buryakovsky et al. (1995) and Bagirov et al. (1999), I set the permeability of the producing layer to 110 mD, whereby for the other layers follows a permeability of ~0.1 mD.

Table 14 lists all material properties applied to the reservoir model, as defined in the Abaqus input file. Note, the permeability is given by the hydraulic conductivity [m/s]. The conversion factor between hydraulic conductivity and permeability [m^2] is 10^{-7}. 1 mD is equal to 10^{-15} m^2.

Table 14. Material property values for all ten layers of the poroelastic model. The change in ρ, κ and ν result from the density and velocity logs. The conversion factor between hydraulic conductivity [m/s] and permeability [m^2] is 10^{-7}. 1 mD is equal to 10^{-15} m^2.

Layer	ρ [kg/m^3]	K_g [GPa]	K_f [GPa]	κ	ν	p_t^{el} [GPa]	e	k_f [10^{-9} m/s]	ρ_f [kg/m^3]
1	2200	40	2	0.252	0.45	1.2	0.4	4.0	1000
2	2250	40	2	0.235	0.43	1.6	0.4	1.9	1000
3	2290	40	2	0.239	0.40	1.8	0.4	1.3	1000
4	2340	40	2	0.228	0.36	1.9	0.4	1.0	1000
5	2360	40	2	0.211	0.32	1.9	0.4	0.97	1000
6	2370	40	2	0.206	0.28	2.0	0.4	1100	1000
7	2400	40	2	0.192	0.26	2.0	0.4	1.4	1000
8	2450	40	2	0.156	0.24	2.0	0.4	2.7	1000
9	2480	40	2	0.136	0.24	2.2	0.4	8.0	1000
10	2550	40	2	0.110	0.24	2.5	0.4	4.0	1000

6.4.2 Boundary conditions and model scenario

The model scenario consists of three main parts. First gravity to the model that is pre-stressed with the initial state of stress of the elastic modelling. For this, the model sides and bottom are fixed in normal direction, and undrained boundary conditions, i.e. no fluid exchange over these boundaries, are applied. The free surface is not constraint and pore pressure is set to zero there. This means, no pore pressure changes can occur at the surface, what is equal to a drained boundary. Then in the next modelling step, at one model side the boundary condition is changed. Instead of fixed in normal direction a displacement of 10 m is applied to it, according to the elastic modelling. In the final modelling step, a production scenario is simulated to model fluid depletion induced pore

pressure and stress changes. For this, production boundary conditions (volume per time) are applied to one point of the wellpaths 1-8 and 11, which is located in the producing layer 6. The entire production scenario lasts 15 years 323 days and is subdivided into three steps:

a) Production at wells 5-8, with 50 l/s each for 325 days

b) Increase of production rate at wells 5-8 to 110 l/s each, and start of production at wells 1-4 with 60 l/s each. Production for 313 days.

c) Increase of production rates at well 5-8 to 125 l/s each and at wells 1-4 to 90 l/s. Start of production at well 11 with 55 l/s. Production for 14 years and 50 days.

Due to the anticlinal structure of the stratigraphic layers, the productive layer 6 varies with depth. At the crest, layer 6 in a depth between ~2250 m and ~2800 m, which increases at the flanks to maximal between ~3000 m and ~4000 m. Because the production points are spread out over the entire reservoir area, they also vary in depth. The production points range between 2300 m depth (well 6) at the crest to 3550 m (well 4 and 8) at the flank of the reservoir.

6.4.3 Results

Pore pressure

Pore pressure changes of the entire model are shown in Figure 6-14. After 2 years 168 days of production (a) the pore pressure change is spread out inside the productive layer 6, and declines to zero at the boundaries to the surrounding layers. After 15 years 323 days of production (b), pore pressure change has further increased inside the productive layer 6, but also in the neighbouring layers, because of the longer production time.

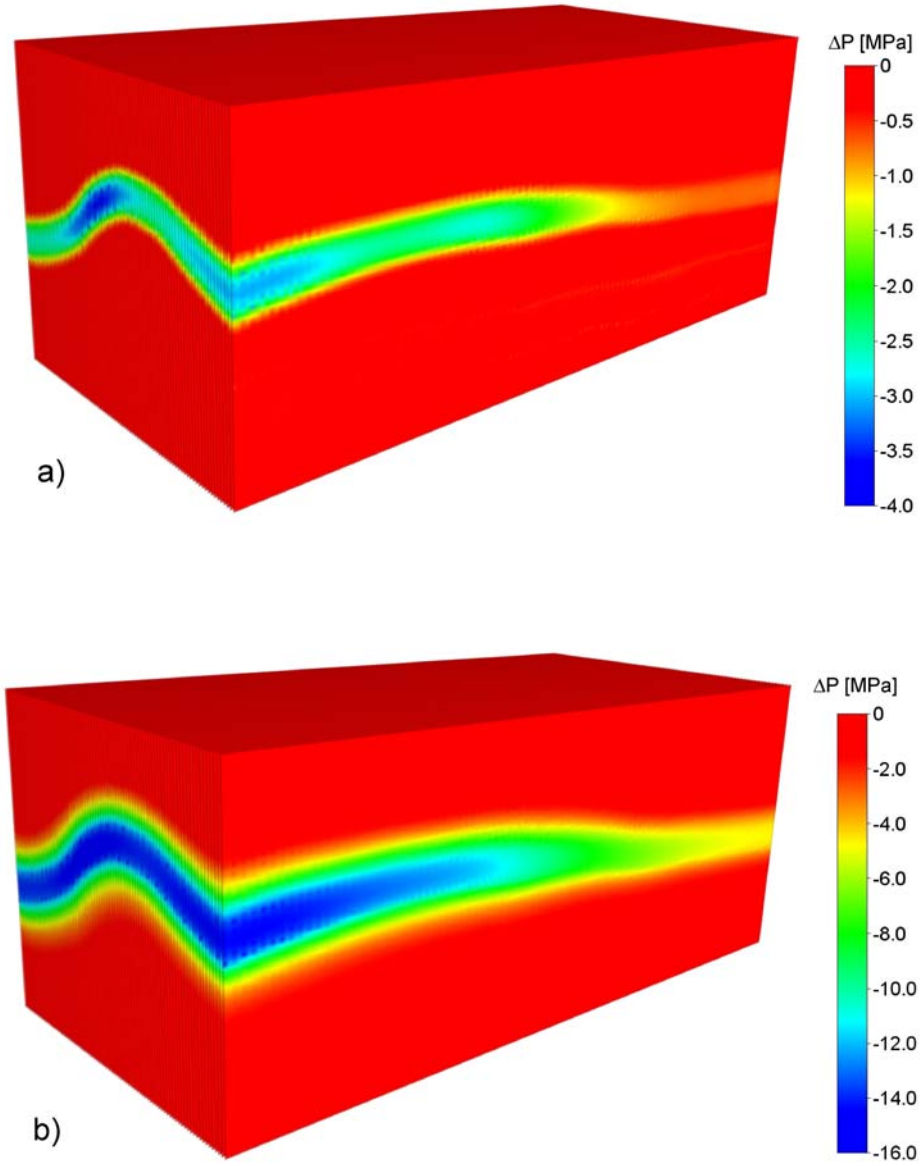

Figure 6-14. Pore pressure change after production of 2 years 168 days (a) and 15 years 323 days (b). Note the different colour scales.

Maximum shear stress

The change in maximum shear stress for different depths after 348 days of production is shown in Figure 6-15. Depending on depth, one can see different pattern of increased and decreased maximum shear stress changes. Because close to the production points the highest pore pressure and stress changes occur, those patterns develop around these areas. Negative as well as maximum shear stress changes occur and the magnitudes and distribution changes with depth.

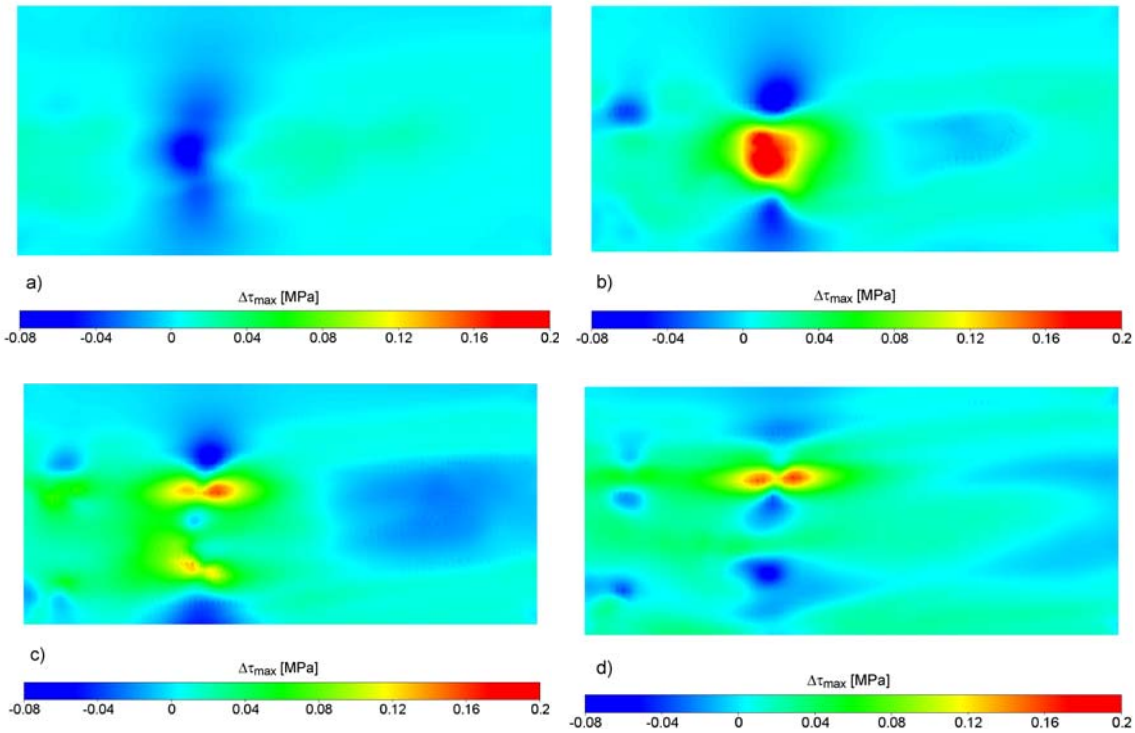

Figure 6-15. Change in maximum shear stress after production of 348 days in depths of 1500 m (a), 2200 m (b), 2700 m (c), 3200 m (d).

After a longer production times of 2 years 168 days (Figure 6-16) and 15 years 323 days (Figure 6-17) the distribution in maximum shear stress change is spreading out, in horizontal direction as well as in vertical direction. All subfigures (b) of the different production times show $\Delta\tau_{max}$ distributions in a depth of 2200 m. It clearly can be seen, how the maximal change, first a spot (Figure 6-15), widens along the crest with increasing magnitude (Figures 6-16 and 6-17).

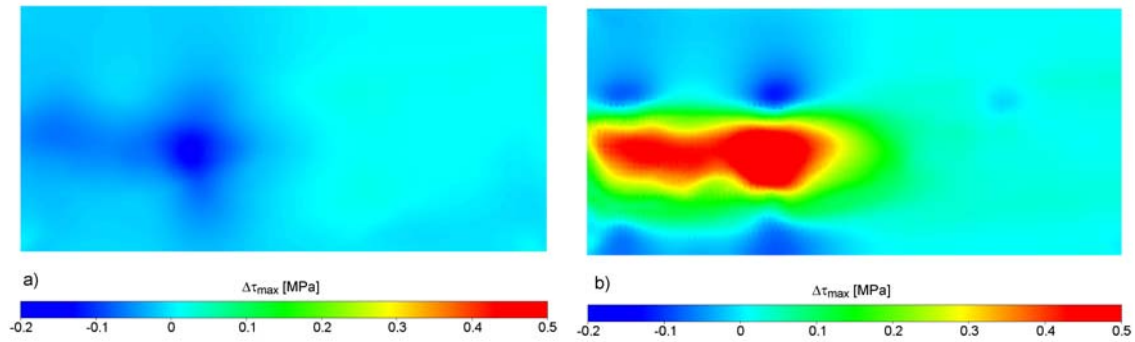

Figure 6-16. Change in maximum shear stress after production of 2 year 168 days in depths of 1300 m (a) and 2200 m (b).

For the negative blue spot in Figure 6-15 the same characteristics with duration of production is observed. After 348 days of production the maximum value is located in a depth of 1500 m (Figure 6-15a), after 2 years 168 days of production the maximum value is in a depth of 1300 m with increased magnitude and spread out wider (Figure

6-16). This development continuous for production time of 15 years 323 days (Figure 6-17).

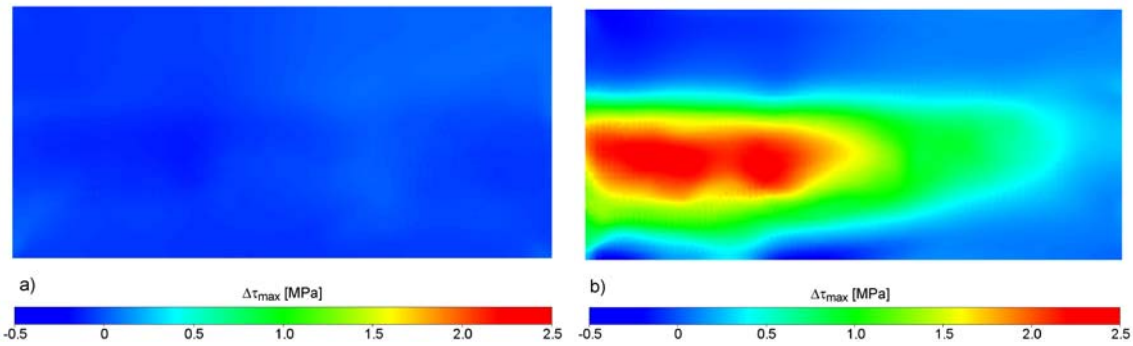

Figure 6-17. Change in maximum shear stress after production of 15 years 323 days in depths of 900 m (a) and 2200 m (b).

6.4.4 Interpretation

Pore pressure

After short production time, pore pressure changes are in the productive layer 6 (Figure 6-14a). With duration of production, maximum pore pressure change increases and diffuses inside layer 6 (Figure 6-14b). The adjacent layers are affected little by the pore pressure change. This is due to the permeability contrast of ~1000 between productive layer 6 and its neighbouring layers above and below. This inhibits the pore pressure to diffuse also into the surrounding layers. Anyway, after 15 years 323 days of production, pore pressure also has diffused into the surrounding layers of layer 6. Pore pressure change decreases strongly within short distance at the reservoir-surrounding boundary from over 16 MPa to 10 MPa.

Maximum shear stress

The maximum shear stress changes maximal close to the production points, where the pore pressure and stress changes are largest. Negative $\Delta\tau_{max}$ occurs above and below the production points, positive $\Delta\tau_{max}$ horizontally of the production points (Figure 6-15). The shallowest production point is at the crest of the reservoir in a depth of 2300 m. Figure 6-15a shows the $\Delta\tau_{max}$ distribution in a depth of 1500 m, i.e. above the production point, where $\Delta\tau_{max}$ is negative. In 2200 m depth (Figure 6-15b), approximately the depth of the production point at the crest, $\Delta\tau_{max}$ is positive. In the same plot two spots of negative $\Delta\tau_{max}$ can be observed, one above and the other below the red maximum, more in the flanks of the reservoir. These blue spots indicate production points in greater depth. In 2700 m depth the blue spots turned into red ones, and at the location of the red spot in 2200 m depth at the crest, there is a small blue spot (Figure 6-15c). With distance to the crest, production points are deeper. The blue spots

detected in 2200 m depth are above production points, which are in a depth of ~2700 m. This depth is below the production point depth at the crest. Therefore, $\Delta\tau_{max}$ is turning negative again at that location. These characteristics can be continued for greater depths. At 3200 m depth, $\Delta\tau_{max}$ becomes more negative at the location of the production point at the crest (Figure 6-15d). Also at the lower location of the two positive $\Delta\tau_{max}$ areas at 2700 m depth has turned to negative maximum shear stress changes. The other one shows still a positive $\Delta\tau_{max}$, indicating that there are further production points in this depth. With duration of production the maximum shear stress changes spread out, and then superpose with changes generated around other production points (Figures 6-16 and 6-17).

According to the analytical investigations (chapter 4), positive and negative maximum shear stress changes occur in certain directions depending on the tectonic stress regime. During fluid depletion, maximal positive shear stress changes occur in σ_3-direction, maximal negative shear stress changes in σ_1-direction, considering local rectangular coordinate systems with their origins at the production point. Measuring the maximal shear stress changes, one could conclude to the tectonic stress regime. For the case here, maximal negative maximum shear stress changes occur above and below the production points, thus in σ_V-direction. Therefore, σ_V has to be equal to σ_1. Then, the tectonic regime would be a normal faulting regime. In a normal faulting regime, the maximal positive shear stress changes occur in σ_h-direction. This is in agreement with the applied boundary condition of 10 m displacement at the lower boundary. This leads to higher horizontal stresses parallel to the applied displacement than perpendicular to it.

7 Summary and concluding discussion

This thesis investigates the changes of key parameters of reservoir geomechanics, namely fluid pressure in reservoir rocks and stress. Both are significant for the assessment of wellbore stability or failure of reservoir bounding faults or faults in the caprock of a reservoir. Furthermore, the orientation of the stress field determines the underground fluid flow orientations. In this chapter, I summarize how stress and pore pressure changes during injection into reservoirs or depletion from reservoirs.

The main questions addressed in this thesis consider the spatial and temporal evolution of pore pressure and stress, and are:

a) How strong is the coupling between pore pressure and stress components, and does this coupling develop with duration of injection/production and distance from the injection/production source?

b) Is there a difference in the coupling between pore pressure and individual stress tensor components? If yes, how is the temporal and spatial evolution of the coupling between pore pressure and different stress components?

c) How does the tectonic stress regime influence the coupling between pore pressure and stress?

7.1 Interaction of pore pressure and stress

The effective stress concept of Terzaghi (1943) allows to consider the influence of pore pressure changes on the stress state. In this concept, effective stresses result from the total stresses by subtraction of the pore pressure – and pore pressure and stress are uncoupled. Therefore, a modification of pore pressure does not lead to a modification of shear stress. However, this is in contrast to the observation of production indueced seismicity in numerous oil and gas fields world-wide (Simpson, 1986; Segall, 1989; Sze et al., 2005; van Eck et al., 2006; Bardainne et al., 2008).

Previous investigations (Engelder and Fischer, 1994; Addis, 1997; Hillis, 2000; Goulty, 2003) derived mathematical expressions to relate pore pressure change to change in minimum horizontal stress, under the assumption that the vertical stress is not affected by the pore pressure. Due to coupling between P and σ_h and no coupling between P and σ_V, in a normal faulting regime the differential stress increases for fluid depletion or pore pressure decrease. Therefore, considering coupling between P and σ_h, it is possible to explain production induced seismicity. However, time-lapse investigations (Sayers, 2004; 2006) and geomechanical modelling (Herwanger and Horne, 2005; Settari and Sen, 2007; Schutjens et al., 2010) shows that not only σ_h, but the entire stress tensor is affected by pore pressure changes.

Chen and Nur (1992) or Hillis (2000) find that in a normal faulting regime increase of pore pressure leads to stabilization and reduction in pore pressure to destabilizations of rock. For a thrust faulting regime, Chen and Nur (1992) state that pore pressure increase leads to destabilization and reduction in pore pressure to destabilization of rock. Soltanzadeh et al. (2009) show that stabilization and destabilization of rock depends on the stress direction occurring at an observation point. There is however no previous 3D investigation and analysis how poroelastic coupling develops in space and time.

7.2 Discussion of results

Based on the pore pressure and stress solutions for continuous fluid injection at one point into homogeneous full space (Rudnicki, 1986), I have derived the coupling ratios between pore pressure and the full stress tensor depending on both space and time, and found that the coupling differs for radial and tangential stress components. For time tending towards infinity, the coupling ratio equations provide static equations. The equation for the radial stress coupling results in Eq. (3.5). This coincides with the coupling coefficient between pore pressure and σ_h, which was derived by Engelder and Fischer (1994) under the assumption that the vertical stress is not affected by pore pressure changes. The equation of the tangential stress results in exact ½ of the result of the radial stress coupling equation. The equation for the long-term limit is only correct for long injection times or short distances to the injection source.

The spatio-temporal change of pore pressure stress coupling equations show that pore pressure stress coupling is not a constant and varies with distance to the injection point as well as with injection time. This could explain the range of some of the field data, which could not be interpreted previously; Addis (1997), Hillis (2000) or Goulty (2003) have problems to explain those field data by their static equations. This thesis and Altmann et al. (2010a) show that using the spatio-temporal pore pressure stress coupling, variations in the observed field data can be explained due to different distances between measurement locations and fluid injection/depletion locations, and due to different injection/depletion durations between begin of injection/production and measurement time.

Furthermore, I investigated pore pressure stress coupling along the principal stress axes and under consideration of different tectonic stress regimes, both for fluid injection as well as for fluid depletion. The results are discussed in terms of maximum shear stress change, which means half of the difference between maximum and minimum principal stress. For great changes in shear stress, either positive or negative, the coupling effect is maximal, for zero shear stress changes, the coupling effect diminishes.

Along the σ_1-axis the change in shear stress is maximal, negative for depletion and positive for injection. Along the σ_3-axis the shear stress change is also maximal but reverse of the change along the σ_1-axis, namely positive for depletion and negative for

injection. There is no shear stress change along the σ_2-axis. This means that for locations along the σ_1-axis the poroelastic coupling effect amplifies the direct effect of effective stress reduction (destabilization of rock) by pore pressure increase, or of effective stress increase (stabilization of rock) by pore pressure reduction.

Analogous, along the σ_3-axis the poroelastic effect is weakening the direct effect of pore pressure on the effective stress. Pore pressure increase leads to smaller effective stresses (destabilization of rock), but due to the coupling the shear stress change is reduced (stabilization of rock). Pore pressure reduction increases the effective stresses (stabilization of rock), but due to coupling leads to increased shear stress (destabilization of rock). For locations along the σ_2-axis, the coupling between pore pressure and maximum and minimum principal stress is the same, leading to effective stresses different from Terzaghi but the shear stress remains constant.

On locations along the σ_1-direction failure is most likely to occur during fluid injection, and least likely during fluid depletion. On the contrary, locations along the σ_3-axis are most stable under fluid injection, most unstable for fluid depletion. Hillis (2000) explains also fluid injection induced stabilization and fluid depletion induced destabilization of rock along the σ_3-axis in a normal faulting regime, with $\sigma_3 = \sigma_h$. As Hillis (2000) assumes coupling only between pore pressure and σ_h, differential stress decreases during fluid injection (pore pressure and σ_h increase), and increases during fluid depletion (pore pressure and σ_h reduction). Thus, my results are in agreement with those of Hillis (2000). However, my approach enables to study the process as a function of position within the reservoir and time. Because in my approach σ_V is also coupled to the pore pressure, I achieve a smaller coupling effect than Hillis (2000).

The time dependence of the coupling is of key importance especially for reservoir geomechanic cases where short scale loading variations occur such as during CO_2 sequestration of stimulation of geothermal reservoirs. To my knowledge this has not been addressed before. My results show that maximum shear stress changes have the strongest impact shortly after start of injection or production, because pore pressure changes are small in comparison to $\Delta\tau_{max}$. With duration of injection/depletion, ΔP is increasing faster than $\Delta\tau_{max}$, and the coupling effect becomes less important. During fluid injection the strong poroelastic coupling at the beginning of the injection can lead to stabilization instead of destabilization as in the classical Terzaghi approach. After longer injection time, the direct effect of ΔP is increasing and the coupling effect loses importance. This can have consequences on the onset of seismicity. Figure 7-1 shows the shortest distance between Mohr circle and failure envelope depending on depletion and injection time for a point on the σ_3-axis with a distance of 200 m to the depletion (injection) point. The original state of stress was assumed for a depth of 3000 m, namely $\sigma_1 = 80$ MPa and $\sigma_3 = 50$ MPa, or for a hydrostatic pore pressure profile $\sigma_{1,eff} = 50$ MPa and $\sigma_{3,eff} = 20$ MPa, and the injection (depletion) rate 50 l/s. The Mohr-Coulomb failure

criterion was defined with a cohesion of 4 MPa and a coefficient of friction of 0.36, what is equivalent to an angle of internal friction of 20°. Due to the effect of poroelastic coupling minima (maxima) occur during the first ten days of depletion (injection). During this time, depletion induced failure could occur (left) as well as stabilization during fluid injection (right). Afterwards, the direct effect of ΔP on the effective stress is primary, what leads to stabilization for fluid depletion (left), and to destabilization for fluid injection. In other words for the case of fluid injection the occurrence of seismic events along the minimum principal stress orientation should only start after ca. 10 days of injection for the given material parameters.

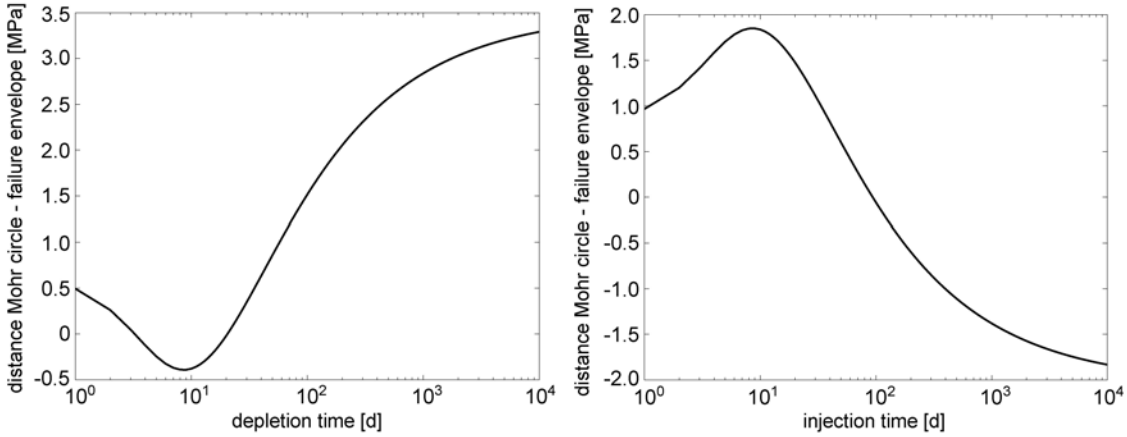

Figure 7-1. Shortest distance between failure envelope and Mohr circle for arbitrary failure planes, depending on depletion time (left) or injection time (right). Considered is a point on the σ_3-axis in distance of 200 m from the depletion (injection) point. Positive distance between failure envelope and Mohr circle means that the Mohr circle is below the failure envelope, i.e. there is no osculation point. Zero distance between failure envelope and Mohr circle means that the failure envelope is tangent to the Mohr circle. Negative distance between failure envelope and Mohr circle means that the failure envelope is cutting the Mohr circle. After start of depletion (left), distance becomes negative, the stress state becomes more unstable and failure will occur. After crossing a minimal distance at 10 days, distance increases with duration of depletion and the stress states stabilizes. Short injection times lead to a stabilization (increasing distance between failure envelope and Mohr circle) of the state of stress on a point on the σ_3-axis. With further duration of injection, the stress state becomes more unstable until failure occurs (negative distance between failure envelope and Mohr circle).

For comparison, Figure 7-2 shows shortest distance between Mohr circle and failure envelope depending on depletion and injection time for locations on the σ_1-axis. Along the orientation of the maximum principal stress, the poroelastic effect of the pore pressure change amplifies the effective stress change according to Terzaghi. In a normal faulting regime, this could be interpreted such that the reactivation of fractures during injection could occur mostly in vertical planes perpendicular to the minimum horizontal stress.

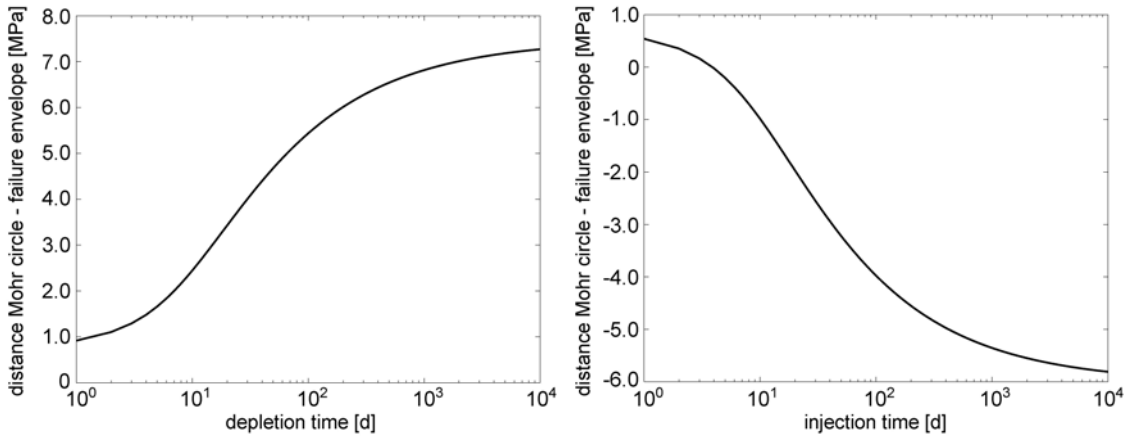

Figure 7-2. Shortest distance between failure envelope and Mohr circle for arbitrary failure planes, depending on depletion time (left) or injection time (right). Considered is a point on the σ_1-axis (in comparison to Figure 7-1, where a point on the σ_3-axis is considered) in distance of 200 m from the depletion (injection) point. Positive distance between failure envelope and Mohr circle means that the Mohr circle is below the failure envelope, i.e. there is no osculation point. Zero distance between failure envelope and Mohr circle means that the failure envelope is tangent to the Mohr circle. Negative distance between failure envelope and Mohr circle means that the failure envelope is cutting the Mohr circle. Depletion (left) leads to a stabilization, injection (right) to a destabilization of the stress state.

In realistic reservoir geometries, the numerically calculated $\Delta\tau_{max}$ varies throughout the reservoir horizon and changes with time. After a short production time, when the maximum shear stress changes have not spread out too far and have superposed with $\Delta\tau_{max}$ generated at other production points, clear patterns of $\Delta\tau_{max}$ can be observed around the production points. Analysing the $\Delta\tau_{max}$ depending on direction, one detects that $\Delta\tau_{max}$ has its negative maximum vertically above and beneath the production points, and its positive maximum horizontally around the production points.

7.3 Conclusion

In this thesis, the effect of pore pressure stress coupling was investigated under different aspects. With an analytical approach I have shown that pore pressure is coupled with all stress components, and that the location with respect to the injection (depletion) source as well as the tectonic regime influence the poroelastic coupling. Investigating numerically the temporal evolution of the coupling effect, it has the most influence directly after start of injection (production), and especially then is not negligible. The observation of maximal shear stress change patterns can be used to determine the tectonic stress regime. In summary, this thesis gives an overview of poroelastic coupling effects on the state of stress in space and time. Numerical modelling is a proper tool to calculate and analyse fluid flow induced stress changes, and to estimate their impact on rock stability, and important aspect in reservoir management.

7.4 Outlook

The future aspects of investigation can be analytical as well as numerical, especially if the loading scenario of a reservoir varies with time. The aspect of tectonic regime changes and stress orientation changes can be studied analytically to quantify the most important parameters. Altmann et al. (2010b) have investigated possible changes in the tectonic regime that may occur during fluid injection or depletion, and defined criteria, when a stress regime change can happen. For realistic geometries and realistic loading scenarios (fluid injection or depletion varying with time) numerical methods have to be used. One aspect is to analyse numerically the influence of pore pressure changes on the stress orientation, especially in the vicinity of faults or structures like diapers which affects the fluid flow in the reservoir and surroundings as well as the reservoir stability.

Acknowledgements

Ich danke Herrn Prof. Dr. Friedemann Wenzel für die Übernahme des Referats, und Herrn Prof. Dr. Serge Shapiro für die Übernahme des Korreferats dieser Arbeit, insbesondere für das in mich gesetzte Vertrauen und das Begutachten der Arbeit in letzter Minute.

Bei Birgit Müller bedanke ich mich für die Betreuung, sowie für ihre Unterstützung und ihr Interesse an meiner Arbeit.

Tobias Müller danke ich für interessante Diskussionen, die mir ermöglicht haben, neue Ideen zu entwickeln. Ganz besonders danke ich ihm für den einjährigen Aufenthalt bei CSIRO in Perth.

Ich danke der Heidelberger Akademie der Wissenschaften, die es mir ermöglicht hat im Rahmen des World Stress Map Projekts einen Großteil meiner Arbeit anzufertigen.

Bei Prof. Dr. Helmut Wilhelm bedanke ich mich für seine Unterstützung während der Endphase meiner Arbeit.

Furthermore, I thank Toby Harrold und Emma Nelson from BP for providing me the geometry of an oil reservoir, and their assistance during the process of model generation.

Ein Dankeschön geht an die ehemaligen Mitglieder der früheren tectonic stress group und rock physics group, die mir in der Anfangsphase meiner Doktorarbeit geholfen haben, und für eine angenehme Arbeitsatmosphäre gesorgt haben.

Ganz besonders bedanke ich mich bei meiner Familie, die mich auf jegliche Art und Weise unterstützt hat und immer für mich da war.

Appendix A

To derive the limiting value of the spatio-temporal pore pressure stress coupling ratio (Eq. 4.33) for infinite time, following limes has to be considered:

$$\lim_{t\to\infty}\frac{2g(\xi)}{\xi^2 erfc\left(\frac{1}{2}\xi\right)} \tag{A.1}$$

what, according to Eq. 4.27 is equal to:

$$\lim_{\xi\to 0}\frac{2g(\xi)}{\xi^2 erfc\left(\frac{1}{2}\xi\right)} \tag{A.2}$$

The function g(ξ) is given by

$$g(\xi)=\frac{1}{2\sqrt{\pi}}\int_0^{\xi} s^2\exp\left(-\frac{1}{4}s^2\right)ds = erf\left(\frac{1}{2}\xi\right)-\frac{\xi}{\sqrt{\pi}}\exp\left(-\frac{1}{4}\xi^2\right), \tag{A.3}$$

where the error function erf(z) and the complementary error function erfc(z) are

$$erf(z)=2\pi^{-1/2}\int_0^{z} e^{-t^2}dt \qquad \text{and} \qquad erfc(z)=1-erf(z). \tag{A.4}$$

Eqs. and substituted into Eq. A.2 leads to

$$\lim_{\xi\to 0}\frac{2\left(erf\left(\frac{1}{2}\xi\right)-\frac{\xi}{\sqrt{\pi}}\exp\left(-\frac{1}{4}\xi^2\right)\right)}{\xi^2\left(1-erf\left(\frac{1}{2}\xi\right)\right)} \tag{A.5}$$

As erf($\xi = 0$) = 0, Eq. gives

$$\lim_{\xi\to 0}\frac{2\left(erf\left(\frac{1}{2}\xi\right)-\frac{\xi}{\sqrt{\pi}}\exp\left(-\frac{1}{4}\xi^2\right)\right)}{\xi^2\left(1-erf\left(\frac{1}{2}\xi\right)\right)}=\frac{0}{0}. \tag{A.6}$$

Though to determine the result of Eq. A.6, the rule of L'Hospitales is applied: If

$$F(x)=\frac{\varphi(x)}{\psi(x)} \tag{A.7}$$

and the following limits hold

$$\lim_{x\to a}\varphi(x)=0 \qquad \text{and} \qquad \lim_{x\to a}\psi(x)=0\,, \tag{A.8}$$

then, it is also true that

$$\lim_{x\to a}F(x)=\lim_{x\to a}\frac{\varphi(x)}{\psi(x)}=\lim_{x\to a}\frac{\frac{d\varphi(x)}{dx}}{\frac{d\psi(x)}{dx}}. \tag{A.9}$$

Accordingly, in order to evaluate

$$\lim_{\xi \to 0} \frac{2g(\xi)}{h(\xi)} \tag{A.10}$$

where

$$g(\xi) = erf\left(\frac{1}{2}\xi\right) - \frac{\xi}{\sqrt{\pi}} \exp\left(-\frac{1}{4}\xi^2\right), \tag{A.11}$$

$$h(\xi) = \xi^2 erfc\left(\frac{1}{2}\xi\right) = \xi^2 - \xi^2 erf\left(\frac{1}{2}\xi\right), \tag{A.12}$$

the derivatives of g(x) and h(x) are built:

$$\frac{dg(\xi)}{d\xi} = \frac{\xi^2}{2\sqrt{\pi}} \exp\left(-\frac{1}{4}\xi^2\right), \tag{A.13}$$

$$\frac{dh(\xi)}{d\xi} = 2\xi erf\left(\frac{1}{2}\xi\right) - \frac{\xi^2}{\sqrt{\pi}} \exp\left(-\frac{1}{4}\xi^2\right) \tag{A.14}$$

Applying the rule of L'Hospitales (Eq. A.9) gives:

$$\lim_{\xi \to 0} \frac{\frac{dg(\xi)}{d\xi}}{\frac{dh(\xi)}{d\xi}} = \frac{0}{0} \tag{A.15}$$

Again, the result if zero divided by zero. Thus, the second derivatives of g(x) and h(x) are built, and then on these the rule of L'Hospitales applied.

$$\frac{d^2 g(\xi)}{d\xi^2} = \left(\frac{\xi}{\sqrt{\pi}} - \frac{\xi^3}{4\sqrt{\pi}}\right) \exp\left(-\frac{1}{4}\xi^2\right) \tag{A.16}$$

$$\frac{d^2 h(\xi)}{d\xi^2} = 2erfc\left(\frac{1}{2}\xi\right) + \left(\frac{\xi^3}{2\sqrt{\pi}} - \frac{4\xi}{\sqrt{\pi}}\right) \exp\left(-\frac{1}{4}\xi^2\right) \tag{A.17}$$

$$\rightarrow \lim_{\xi \to 0} \frac{\frac{d^2 g(\xi)}{d\xi^2}}{\frac{d^2 h(\xi)}{d\xi^2}} = \frac{0}{2} = 0 \tag{A.18}$$

Appendix B

The parameters required as input for numerical modelling with ABAQUS (parameter set A) and the parameters used in Eqs. 4.25 and 4.26 (Rudnicki, 1986) (parameter set B) are related to each other by the following transformations. Parameter set A consists of

- Mass density ρ_S
- Bulk modulus of solid grains K_g
- Bulk modulus of fluid K_f
- Specific weight of the wetting liquid $\rho_f g$
- Hydraulic conductivity k_f
- Void ratio e
- Initial void ratio e_0
- Logarithmic bulk modulus κ
- Elastic tensile limit p_t^{el}
- Poisson's ratio ν
- Injection rate V_{fl}

Parameter set B is given by:

- Injected fluid mass per time Φ
- Fluid density ρ_f
- Biot-Willis coefficient α
- First Lamé parameter λ
- Second Lamé parameter μ
- Undrained first Lamé parameter λ_u
- Diffusivity c

Parameter set B can be expressed in dependence of parameters of set A by:

$$\Phi = V_{fl}\rho_f \tag{B.1}$$

The fluid density ρ_f is indirectly given by the ABAQUS input variable of the specific weight of the wetting liquid $\rho_f g$. The Biot-Willis coefficient α can be expressed in dependence of K_d and K_g (Eq. 3.4). K_g is an ABAQUS input parameter, K_d can be expressed by means of the logarithmic bulk modulus κ which appears in Eq. 5.3 for the elastic part of the volume ratio between the current and a reference state J^{el}. According to ABAQUS Documentation (2008), the shear modulus G is defined as

$$G = \frac{3(1-2\nu)(1+e_0)}{2(1+\nu)\kappa}\left(p + p_t^{el}\right)\exp\left(\varepsilon_{vol}^{el}\right) \tag{B.2}$$

with Poisson's ratio ν, initial void ratio e_0, and logarithmic measure of the elastic volume change $\varepsilon_{vol}^{el} = \ln J^{el}$. Using this expression in Eq. B.2 and then substituting Eq. 5.3 into Eq. B.2, the drained bulk modulus K_d can be expressed by κ as

$$K_d = \frac{1+e_0}{\kappa}\left(p + p_t^{el}\right)\left[1 + \frac{\kappa}{1+e_0}\ln\left(\frac{p_0 + p_t^{el}}{p + p_t^{el}}\right)\right] \tag{B.3}$$

with the mean stress p, the initial mean stress p_0, and the elastic tensile limit p_t^{el}, and where

$$G = K_d \frac{3(1-2\nu)}{2(1+\nu)} \tag{B.4}$$

was used. Under the assumption that $p_t^{el} >> p_0$ and $p_t^{el} >> p$, Eq. B.3 simplifies to

$$K_d = \frac{1+e_0}{\kappa}\left(p + p_t^{el}\right) \tag{B.5}$$

The first Lamé parameter λ is given by Eq. 4.22, where the second Lamé parameter μ can be replaced by Eq. 4.35 in terms of λ and ν. The undrained first Lamé parameter λ_u is given by Eq. 4.23, where the undrained bulk modulus K_u is defined by Eq. 4.24 (Gassmann, 1951). The bulk moduli K_f and K_g in Eq. 4.24 are ABAQUS input parameters, K_d is determined by Eq. B.5. The porosity φ in Eq. 4.24 can be expressed in terms of void ratio e:

$$\varphi = \frac{e}{1+e} \tag{B.6}$$

The diffusivity c is given by Eq. 4.28, where the permeability K can be expressed in terms of hydraulic conductivity k_f (Eq. 4.30), which is part of parameter set A.

Appendix C

In order to calculate the circumferential stress $\sigma_{\vartheta\vartheta}$ around arbitrarily inclined and orientated wellbores of the geomechanical model, and to compare the direction of maximum $\sigma_{\vartheta\vartheta}$ with observed borehole breakouts, a matlab program was written. It is based on the transformation of a stress tenor in a geographic coordinate system into a local wellbore coordinate system, done by a simplified transformation of Equation 6.2. As the stress tensor is used as Abaqus output variable and not the principal stresses, the part of the transformation which is rotating the geographical coordinate system in such way that the axes of the system are aligned with the directions of the principal stresses, can be omitted. The program consists of five parts:

1) Read in of data

To transform the modelled stress tensors into local wellbore coordinate systems, to calculate the orientations of maximum circumferential stress $\sigma_{\vartheta\vartheta,max}$ and to compare these directions with observed borehole breakout orientations, first the program is fed with data. The trajectories (Figure C-1, small dots) of all wellbores inside the model volume, along borehole breakouts are observed, are imported. Furthermore, the locations and orientations of the observed borehole breakouts (Figure C-1, elongated rectangles) are read in, as well as the coordinates of points in the model, which are located on the wellbore trajectories, and the stress tensors calculated at those points (Figure C-1, black circles).

2) Transformation of stress tensor into local wellbore coordinate system

Before starting with the transformation of the stress tensor from the geographic into the local wellbore coordinate system, some preparations are done. As for stresses in Abaqus the engineering sign convention (compression is negative) is used, the stresses calculated along the wellbore trajectories are multiplied by -1 to bring the stresses into geo sign convention (compression is positive). Afterwards, these stresses and their coordinates are sorted with increasing depth. To use the coordinate transformation according to Peska and Zoback (1995), the stresses given in the coordinate system X = east, Y = north, Z = up are transformed into a coordinate system X' = north, Y' = east, Z' = down by two rotations; one rotation about the z-axis by $\pi/2$, and another one about the x-axis by π with the rotations matrices

$$R_1 = \begin{pmatrix} 0 & 1 & 0 \\ -1 & 0 & 0 \\ 0 & 0 & 1 \end{pmatrix}, \qquad R_2 = \begin{pmatrix} 1 & 0 & 0 \\ 0 & -1 & 0 \\ 0 & 0 & -1 \end{pmatrix} \tag{C.1}$$

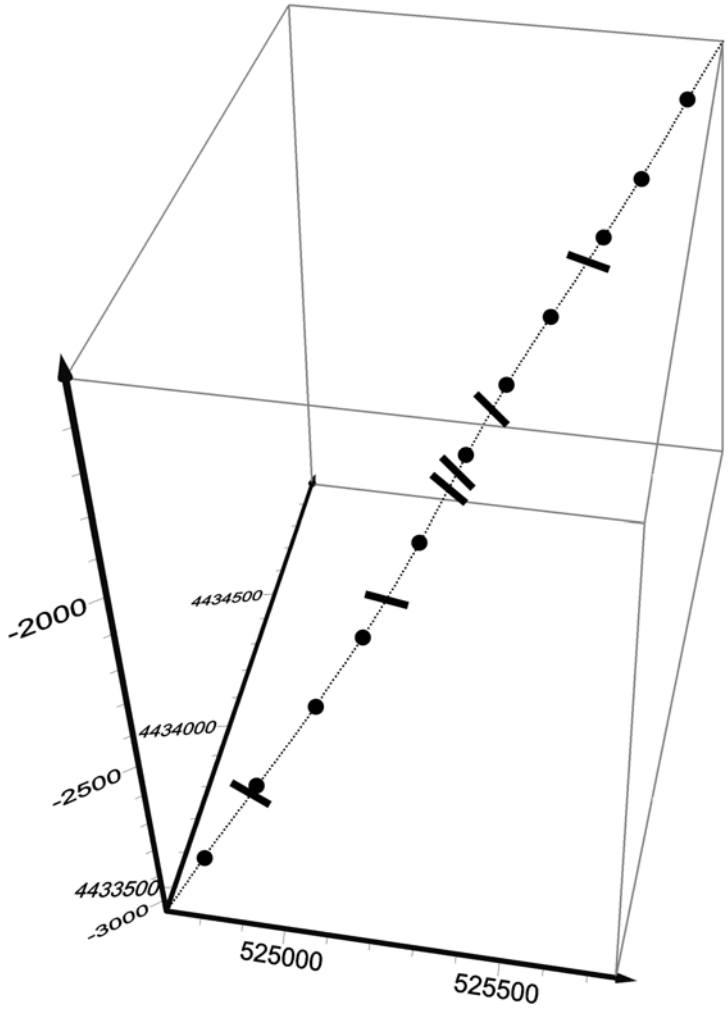

Figure C-1. Illustration of the input for the matlab program. Small dots represent an inclined wellbore trajectory, black circles element nodes of the model volume, which are located on the trajectory and at which the states of stress are calculated. Coordinates and modelled stresses are read in the program. The black elongated rectangles stand for the locations and orientations of observed borehole breakouts, both imported into the program.

To implement the actual transformation, the two rotation angles δ, azimuth of the horizontal projection of the borehole clockwise from geographic north to geographic east, and φ, deviation of the borehole axis from the vertical (Figure 6-4), has to be known. For all points along the wellbore trajectories, where the state of stress is modelled at, δ is calculated by $\delta = \arctan(\Delta y / \Delta x)$. Δx and Δy, respectively, are differences in *x*-direction and *y*-direction of the two trajectory points (Figure C-1, small dots) which are closest to the point the state of stress is calculated at (Figure C-1, black circle). One of the two trajectory points is the closest above, and the other the closest below the point at which the state of stress is calculated at. The angle φ is calculated by determining the tangents at the distinct points, the stress states are calculated at, and by calculating the angle between this tangent and the vertical.

3) Calculation of $\sigma_{\vartheta,\vartheta}$ and the direction of $\sigma_{\vartheta,\vartheta,max}$

After the two rotation angles δ and φ are known, the modelled stress tensors at the distinct points inside the model volume (black circles, Figure C-1) are rotated into local wellbore coordinate systems by $\sigma_b = R_b \cdot \sigma \cdot R_b^T$, with the rotated stress tensor σ_b, the stress tensor to be rotated σ, and the rotation matrix

$$R_b = \begin{pmatrix} -\cos\delta\cos\varphi & -\sin\delta\cos\varphi & \sin\varphi \\ \sin\delta & -\cos\delta & 0 \\ \cos\delta\sin\varphi & \sin\delta\sin\varphi & \cos\varphi \end{pmatrix} \tag{C.2}$$

According to Peska and Zoback (1995) the circumferential stress $\sigma_{\vartheta\vartheta}$ is calculated using the rotated stresses by

$$\sigma_{\vartheta\vartheta} = \sigma_{11} + \sigma_{22} - 2(\sigma_{11} - \sigma_{22})\cos 2\vartheta + 4\sigma_{12}\sin 2\vartheta - \Delta P \tag{C.3}$$

where ΔP is the difference between the borehole fluid pressure and the pore pressure in the rock. For elastic rheology the term ΔP disappears, and total stresses are considered. For poroelastic rheology, the normal stresses σ_{ii} are replaced by the effective normal stresses $\sigma_{ii,eff}$ and ΔP is assumed to be zero.

In order to compare modelled potential breakout orientations and observed breakout orientations, the direction of maximum $\sigma_{\vartheta\vartheta}$, which coincides with the direction of potential borehole breakouts, is calculated by building the derivative of $\sigma_{\vartheta\vartheta}$ with respect to ϑ and setting the result equal to zero:

$$\frac{d\sigma_{\vartheta\vartheta}}{d\vartheta} = 4(\sigma_{11}\sigma_{22})\sin 2\vartheta + 8\sigma_{12}\cos 2\vartheta = 0 \tag{C.4}$$

$$\Rightarrow \vartheta_{\max} = \frac{1}{2}\arctan\left(-\frac{2\sigma_{12}}{\sigma_{11} - \sigma_{22}}\right) \tag{C.5}$$

With forming the arctan, one has to perform a case differentiation. The tangent of an angle is π-periodic, but the factor 1/2 in Equation C.5 leads the tangent to be $\pi/2$-periodic. Thus, one has to consider the direction, in which ϑ is maximal, also as $\vartheta_{max} \pm \pi/2$. Then, $\sigma_{\vartheta\vartheta}$ is calculated for both ϑ_{max} and $\vartheta_{max} \pm \pi/2$, and compared to each other. The larger of these two stresses is the maximum circumferential stress and the direction to this stress gives the direction of potential borehole breakout.

4) Comparison to observed borehole breakout orientations

In order to correctly compare modelled and observed breakout orientations, two facts has to be taken into consideration.

a) The calculated potential borehole breakout orientations using the modelled stress states are compared to the observed borehole breakout orientations. As the locations of observed borehole breakout orientations do not coincide with element nodes along the wellbore trajectories, at which the output of the modelled stresses is generated, a maximum distance between one of the element nodes and the locations of the observed borehole breakouts was defined. For vertical distances less than 60 m, what is equivalent to half of the average element size in vertical direction, the observed

borehole breakout orientation is compared to the closest point of modelled potential breakout orientation. If the vertical distance between the location of an observed borehole breakout and the closest model element node is more than 60 m, the comparison with this breakout orientation is discarded.

b) The angle ϑ describes the orientation of a potential breakout orientation with respect to the low side of the wellbore and not with respect to geographic north direction. To compare modelled potential breakout orientation with observed breakout orientations which are given with respect to geographic north direction, the modelled breakout orientations has to be transformed into angles with respect to geographic north. As the angle δ between geographic north and the low side of the wellbore is given by the orientation of the wellbore, one has to add the two angles δ and ϑ. The summation of those two angles is correct only in case of vertical wellbores. For inclined wellbores, δ and ϑ can not be added as simple as mentioned before, because the two angles are in different planes which coincide only for vertical wellbores. δ is in a horizontal plane, ϑ in a plane perpendicular to the inclination of the wellbore. Thus, before adding those two angles, ϑ has to be projected into a horizontal plane, what is done by

$$\vartheta_{hori} = \arctan\left(\frac{\tan\vartheta}{\cos\varphi}\right) \tag{C.6}$$

where φ describes the deviation of the wellbore axis from the vertical direction. Then, δ can be added to ϑ_{hori} to receive the modelled potential breakout orientation.

5) In the final program step modelled and observed breakout orientations are graphically compared in rosette plots. Modelled data as well as plots are saved as files.

8 References

ABAQUS Documentation Version 6.8, 2008. Dassault Systèmes Simulia Corp., Providence, Rhode Island, USA.

Abramowitz, M., and Stegun, I.A., 1965. *Handbook of mathematical functions with formulas, graphs and mathematical tables*. Dover publications, ISBN 0-486-61272-4.

Addis, M.A., 1997. The stress-depletion response of reservoirs. *Society of Petroleum Engineers*, SPE 38720, p. 55-65.

Ahmadov, R., Vandorio, T., and Mavko, G., 2009. Confocal laser scanning and atomic-force microscopy in estimation of elastic properties of the organic-rich Bazhenov formation. *The Leading Edge*, Special section: Rock Physics, Jan. 2009, p. 18-23.

Altmann, J.B., Müller, T.M., Müller. B.I.R., Tingay, M.R.P, and Heidbach, O., 2010a. Poroelastic contribution to the reservoir stress path. *International Journal of Rock Mechanics and Mining Sciences*, v. 47, p. 1104-1113.

Altmann, J.B., Müller, B.I.R., Müller, T.M., Heidbach, O., and Wenzel, F., 2010b. Impact of tectonic regime and initial state of on pore pressure/stress coupling process in 3D. *Geophysical Prospecting*, under review.

Anderson, E.M., 1905. The dynamics of faulting. *Transactions of the Edinburgh Geological Society*, v. 8, no. 3, p. 387-402.

Bagirov, E., Bagirov, B., Lerche, I., and Mamedova, S., 1999. South Caspian oil fields: onshore and offshore reservoir properties. *Natural Resources Research*, v. 8, no. 4, p. 299-313.

Bardainne, T., Dubos-Sallee, N., Senechal, G., Gaillot, P., and Perroud, H., 2008. Analysis of the induces seismicity of the Lacq gas field (Southwestern France) and model of deformation. *Geophysical Journal International*, v. 172, p. 1151-1162.

Barton, C.A., Zoback, M.D., and Burns, K.L., 1988. In-situ stress orientation and magnitude at the Fenton geothermal site, New Mexico, determined from wellbore breakouts. *Geophysical Research Letters*, v. 15, no. 5, p. 467-470.

Bear, J., 1972. *Dynamics of fluids in porous media*. American Elsevier Publishing Company, Inc, New York, ISBN 0-486-65675-6.

Bell, J.S., 1990. The stress regime of the Scotian Shelf offshore eastern Canada to 6 kilometers depth and implications for rock mechanics and hydrocarbon migration. In: Maury, V., and Fourmaintraux, D., Editors, *Rock at great depth*, Balkema, Rotterdam, p. 1243-1265.

Bell, J.S., and Gough, D.I., 1979. Northeast-southwest compressive stress in Alberta: Evidence from oil wells. *Earth and Planetary Science Letters*, v. 45, p. 475-482.

Biot, M.A., 1941. General theory of three-dimensional consolidation. *Journal of Applied Physics*, v. 12, p. 155-164.

Birch, F., 1961. The velocity of compressional waves in rocks to 10 kilobars, Part 2. *Journal of Geophysical Research*, v. 66, p. 2199-2224.

Breckels, I.M., and van Eekelen, H.A.M., 1982. Relationship between horizontal stress and depth in sedimentary basins. *Journal of Petroleum Technology*, v. 34, p. 2191-2198.

Brudy, M., Zoback, M.D., Fuchs, K., Rummel, F., and Baumgärtner, J., 1997. Estimation of the complete stress tensor to 8km depth in the KTB scientific drill holes: Implications for crustal strength. *Journal of Geophysical Research*, v. 102, p. 18453-18475.

Buryakovsky, L.A., Djevanshir, R.D., and Chilingar, G.V., 1995. Abnormally-high formation pressures in Azerbaijan and the South Caspian basin (as related to smectite ↔ illite transformations during diagenesis and catagenesis). *Journal of Petroleum Science and Engineering*, v. 13, p. 203-218.

Chen, Q., and Nur, A., 1992. Pore fluid pressure effects in anisotropic rocks: mechanism of induced seismicity and weak faults. Pure and Applied Geophysics, v. 139, no. 3/4, p. 463-479.

Choquette, P.W., and Pray, L.C., 1970. Geologic nomenclature and classification of porosity in sedimentary carbonates. *AAPG Bulletin*, v. 54, no. 2, p. 207-244.

Cooper, G.A., 1994. Directional drilling. *Scientific American*, v. 270, no. 5, p. 82-87.

Coulomb, C.A., 1776. Sur une application des règles maximis et minimis a quelques problèmes de statique, relatifs à l'architecture. *Mémoires de mathématique et de physique, Académie Royale des Scienes*, v. 7, p. 343-382.

Cuenot, N., Charléty, J., Dorbath, L., and Haessler, H., 2006. Faulting mechanism and stress regime at the European HDR site Soultz-sous-Forêts, France. *Geothermics*, v. 35, p. 561-575.

Darcy, H., 1856. Les fountains publiques de la ville de Dijon. Dalmont, Paris.

Davis, S.D., Nyffenegger, P.A., and Frohlich, C., 1995. The 9 April 1993 earthquake in south-central Texas: Was it induced by fluid withdrawal? *Bulletin of the Seismological Society of America*, v. 85, no. 6, p. 1888-1895.

Detournay, E., and Cheng, A.H.-D., 1993. Fundamentals of poroelasticity. In: Hudson, J.A., Editor, *Comprehensive rock engineering: Principles, practice and projects*, Pergamon Press, Oxford, UK, v. 2, p. 113-171.

D'Heur, M., 1984. Porosity and hydrocarbon distribution in the North Sea chalk reservoirs. *Marine and Petroleum Geology*, v. 1, p. 211-238.

Doser, D.I., Baker, M.R., Luo, M., Marroquin, P., Ballesteros, L., Kingwell, J., Diaz, H.L., and Kaip, G., 1992. The not so simple relationship between seismicity and oil production in the Permian basin, West Texas. *Pure and Applied Geophysics*, v. 139, no. 3/4, p. 481-506.

Eckert, A., 2007. 3D multi-scale finite element analysis of the crustal state if stress in the Western US and the Eastern California shear zone, and implications for stress – fluid flow interactions for the Coso geothermal field. PhD thesis, Geophysical Institute, Physics Department, University of Karlsruhe, Germany, 116p.

Ehrenberg, S.N., and Nadeau, P.H., 2005. Sandstone vs. carbonate petroleum reservoirs: A global perspective on porosity-depth and porosity-permeability relationships. *AAPG Bulletin*, v. 89, no. 4, p. 435-445.

Eisbacher, G.H., 1996. Einführung in die Tektonik. Ferdinand Enke Verlag, Stuttgart, Germany, ISBN 3-432-99252-1, 374p.

Engelder, T., 1993. Stress regimes in the lithosphere. Princeton University Press, Princeton, New Jersey, USA, ISBN 0-691-08555-2, 475p.

Engelder, T., and Fischer, M.P., 1994. Influence of poroelastic behaviour on the magnitude of minimum horizontal stress, S_h, in overpressured parts of sedimentary basins. *Geology*, v. 22, p. 949-952.

Eseme, E., Urai, J.L., Krooss, B.M., and Littke, R., 2007. Review of mechanical properties of oil shales: implications for exploitation and basin modelling. *Oil Shale*, v. 24, no. 2, p. 15-174.

Feignier, B., and Grasso, J.-R., 1990. Seismicity induced by gas production: I. Correlation of focal mechanics and dome structure. *Pure and Applied Geophysics*, v. 134, no. 3, p. 405-426.

Fielding, E.J., Blom, R.G., and Goldstein, R.M., 1998. Rapid subsidence over oil fields measured by SAR interferometry. *Geophysical Research Letters*, v. 25, no. 17, p. 3215-3218.

Freeze, R.A., 1994. Henry Darcy and the fountains of Dijon. *Ground Water*, v. 32, no. 1, p. 23-30.

Gassmann, F., 1951. *Ueber die Elastizitaet poroeser Medien*. Vierteljahrsschrift der Naturforschenden Gesellschaft in Zuerich, v. 96, p.1-23.

Goulty, N.R., 2003. Reservoir stress path during depletion of Norwegian chalk oilfields. *Petroleum Geoscience*, v. 9, p. 233-241.

Grasso, J.R., 1992. Mechanics of seismic instabilities induced by the recovery of hydrocarbons. *Pure and Applied Geophysics*, v. 139, no. 3/4, p. 507-534.

Grasso, J.R., and Wittlinger, G., 1990. Ten years of seismic monitoring over a gas field. *Bulletin of the Seismological Society of America*, v. 80, no. 2, p. 450-473.

Haimson, B., 1975. Deep in-situ stress measurements by hydro fracturing. *Tectonophysics*, v. 29, p. 42-47.

Handin, J., 1969. On the Mohr-Coulomb failure criterion. *Journal of Geophysical Research*, v. 74, no. 22, p. 5343-5348.

Heidbach, O., Tingay, M., Barth, A., Reinecker, J., Kurfeß, D., and Müller, B., 2008. The 2008 release of the World Stress Map, http://dc-app3-14.gfz-potsdam.de/

Hergert, T., 2009. Numerical modelling of the absolute stress state in the Marmara Sea region – a contribution to seismic hazard assessment. PhD thesis, Geophysical Institute, Physics Department, University of Karlsruhe, Germany, 152p.

Herwanger, J., and Horne, S., 2005. Predicting time-lapse stress effects in seismic data. *The Leading Edge*, p. 1234-1242.

Hettema, M.H.H., Papamichos, E., and Schutjens, P.M.T.M., 2002. Subsidence delay: Field observations and analysis. *Oil & Gas Science and Technology*, v. 5, p. 443-458.

Hickman, S.H., Healy, J.H., and Zoback, M.D., 1985. In situ stress, natural fracture distribution, and borehole elongation in the Auburn geothermal well, Auburn, New York. *Journal of Geophysical Research*, v. 90, p. 5497-5512.

Hickman, S.H., and Zoback, M.D., 2004. Stress orientations and magnitudes in the SAFOD Pilot Hole. *Geophysical Research Letters*, v. 31, L15S12, doi: 10.1029/2004/GL020043.

Hillis, R., 2000. Pore pressure/stress coupling and its implications for seismicity. *Exploration Geophysics*, v. 31, p. 448-454.

Hillis, R.R., 2001. Coupled changes in pore pressure and stress in oil fields and sedimentary basins. *Petroleum Geoscience*, v. 7, p. 419-425.

Hillis, R.R., 2003. Pore pressure/stress coupling and its implications for rock failure. In: Van Rensbergen, P., Hillis, R.R., Maltman, A.J., and Morley, C.K., Editors, *Subsurface sediment mobilization*, Geological Society of London, London, Special Publications 2003, v. 216, p. 359-368, doi: 10.1144/GSL.SP.2003.216.01.23.

Hillis, R.R., and Reynolds, S.D., 2000. The Australian stress map. *Journal of the Geological Society, London*, v. 157, p. 915-921.

Jaeger, J.C., Cook, N.G.W., and Zimmerman, R.W., 2007. *Fundamentals of rock mechanics*. Wiley-Blackwell Publishing, Oxford, ISBN-10 0632057599, ISBN-13 978-0632057597, 488p.

Kirsch, G., 1898. Die Theorie der Elastizität und die Bedürfnisse der Festigkeitslehre. *Zeitschrift des Vereins Deutscher Ingenieure*, v. 29, p. 797-807.

Li, S., 2009. Characteristics of fluid substitution in porous rock. *Petroleum Science*, v. 6, no. 2, p.139-145, doi: 10.1007/s12182-009-0022-z.

Lonardelli, I., Wenk, H.-R., and Ren, Y., 2007. Preferred orientation and elastic anisotropy in shales. Geophysics, v. 72, no. 2, p. D33-D40.

Lucia, F.J., 1999. *Carbonate reservoir characterization*. Springer-Verlag, Berlin Heidelberg New York, ISBN 3-540-63782-6.

Mavko, G., Mukerji, T., and Dvorkin, J., 2009. The rock physics handbook, tools for seismic analysis of porous media. *Cambridge University Press*, ISBN-13: 978052186 1366.

Mohr, O., 1882. Ueber die Darstellung des Spannungszustandes und des Deformationszustandes eines Korperelementes und ueber die Anwendung derdelben in der Festigkeitslehre. *Civilengenieur*, v. 28, p. 113–156.

Moore, C.H., 2001. Carbonate reservoirs, porosity evolution and diagenesis in a sequence stratigraphic framework. Elsevier Science B.V., Amsterdam, ISBN 0-444-50838-4.

Nicholson, C., and Wesson, R.L., 1992. Triggered earthquakes and deep well activities. *Pure and Applied Geophysics*, v. 139, no. 3/4, p. 561-578.

Parry, R.H.G., 1995. *Mohr circles, stress paths and geotechnics*. E & FN Spon, Chapman & Hall, London, ISBN 0 419 19290 5.

Peska, P., and Zoback, M.D., 1995. Compressive and tensile failure of inclined well bores and determination of in situ stress and rock strength. *Journal of Geophysical Research*, v. 100, no. B7, p. 12791-12881.

Plumb, R.A., and Cox, J.W., 1987. Stress directions in Eastern North America determined to 4.5 km from borehole elongation measurements. Journal of Geophysical Research, v. 92, no, B6, p. 4805-4816.

Rice, J.R., and Cleary, M.P., 1976. Some basic stress diffusion solutions for fluid-saturated elastic porous media with compressible constituents. *Reviews of Geophysics and Space Physics*, v. 14, no. 2, p. 227-241.

Rozhko, A.Y., 2010. The role of seepage forces on seismicity triggering. *Journal of Geophysical Research*, accepted for publication.

Rudnicki, J.W., 1986. Fluid mass sources and point forces in linear elastic diffusive solids. *Mechanics of Materials*, v. 5, p. 383-393.

Ruistuen, H., Teufel, L.W., and Rhett, D.W., 1999. Influence of reservoir stress path on deformation and permeability of weakly cemented sandstone reservoirs. SPE Reservoir Evaluation & Engineering, v. 2, n. 3, p. 266-272.

Rutledge, J.T., Phillips, W.S., and Schuessler, B.K., 1998. Reservoir characterization using oil-production-induced microseismicity, Clinton County, Kentucky. *Tectonophysics*, v. 289, p. 129-152.

Salz, L.B., 1977. Relationship between fracture propagation pressure and pore pressure. *Society of Petroleum Engineers*, SPE 6870-MS, SPE annual fall technical conference and exhibition, Denver, Colorado, doi: 10.2118/6870-MS.

Santoso, D., Alam, S., Hendraya, L., Alfian, Sulistiyono, and Munadi, S., 1995. Estimation of limestone reservoir porosity by seismic attribute and AVO analysis. *Exploration Geophysics*, v. 26, p. 437-443.

Sayers, C., 2004. Inversion of elastic wave velocity measurements for monitoring changes in rock stress resulting from production. *Gulf Rocks 2004, the 6th North America Rock Mechanics Symposium (NARMS)*, Houston, Texas, 8p.

Sayers, C., 2006. Sensitivity of time-lapse seismic to reservoir stress path. *Geophysical Prospecting*, v. 54, p. 369-380.

Schmitt, D.R., Smither, C., and Ahrens, T.J., 1989. In-situ holographic elastic moduli measurements from boreholes. *Geophysics*, v. 54, no. 4, p. 468-477.

Schoenball, M., Müller, T.M., Müller, B.I.R., and Heidbach, O., 2010. Fluid-induced microseismicity in pre-stressed rock masses. *Geophysical Journal International*, v. 180, p. 813-819.

Schutjens, P.M.T.M., Hanssen, T.H., Hettema, M.H.H., Merour, J., de Bree, P., Coremans, J.W.A., and Helliesen, G., 2004. Compaction-induced porosity/permeability reduction in sandstone reservoirs: Data and model for elasticity-dominated deformation. *SPE Reservoir Evaluation & Engineering*, v. 7, no. 3, p. 202-216.

Schutjens, P.M.T.M., Snippe, J.R., Mahani, H., Turner, J., Ita, J., and Mossop, A.P., 2010. Production-induced stress change in and above a reservoir pierced by two salt domes: A geomechanical model and its implications. *72nd SPE EUROPEC/EAGE conference and exhibition*, Barcelona, Spain, Extended abstracts L013.

Segall, P., 1989. Earthquakes triggered by fluid extraction. *Geology*, v. 17, p. 942-946.

Segall, P., Grasso, J.-R., and Mossop, A., 1994. Poroelastic stressing and induced seismicity near the Lacq gas field, southwestern France. *Journal of Geophysical Research*, v. 99, no. B8, p. 15423-15438.

Settari, A., and Sen, V., 2007. The role of geomechanics in integrated reservoir modelling. *The Leading Edge*, p. 622-627.

Shapiro, S.A., Royer, J.-J., and Audigane, P., 1998. Estimating the permeability from fluid-injection induced seismic emission. In: Thimus, J.-F., Abousleiman, Y., Cheng, A.H.-D., Coussy, O., and Detournay, E., Editors, *Poromechanics*, Balkema, Rotterdam, p. 301-305.

Shapiro, S.A., Patzig, R., Rothert, E., and Rindschwentner, J., 2003. Triggering of seismicity by pore-pressure perturbations: Permeability-related signatures of the phenomenon. Pure and Applied Geophysics, v. 160, p. 1051-1066.

Sheorey, P.R., 1994. A Theory for in situ stresses in isotropic and transversely isotropic rock. *International Journal of Rock Mechanics and Mining Sciences*, v. 31, no. 1, p. 22-34.

Simpson, D.W., 1986. Triggered earthquakes. *Annual review of Earth and Planetary Sciences*, v. 14, p. 21-42.

Simpson, D.W., and Leith, W., 1985. The 1976 and 1984 Gazli, USSR, earthquakes – were they induced? *Bulletin of the Seismological Society of America*, v. 75, no. 5, p. 1465-1468.

Soltanzadeh, H., Hawkes, C.D., McLellan, P.J., and Smith, S.A., 2009. Poroelastic modelling of production and injection-induces stress changes in a Pinnacle Reef. In: Proceedings of RockEng09, Rock engineering in difficult conditions, *3rd Canada-US Rock Mechanics Symposium*, Toronto, Ontario.

Stoll, R.D., 1998. Comments on "Biot model of sound propagation in water-saturated sand" [J. Acoust. Soc. Am. 97, 199-214 (1995)]. *Journal of the Acoustical Society of America*, v. 103, no. 5, Pt. 1, p. 2723-2725.

Suckale, J., 2010. Moderate-to-large seismicity induced by hydrocarbon production. *The Leading Edge*, p. 310-319.

Sze, E., Toksoz, M.N., and Burns, D.R., 2005. Characterization of induced seismicity in a petroleum reservoir: A case study. *Department of Earth, Atmosphere and Planetary Sciences, Massachusetts Institute of Technology*, p. 7.

Terzaghi, K., 1943. *Theoretical soil mechanics*. J. Wiley and Sons, New York, xvii, 510p (465 T45 1943).

Teufel, L.W., 1996. Influence of pore pressure and production-induced changes in pore pressure on in situ stress. *United States Department of Energy*, Sandia report, p. 54.

Teufel, L.W., Rhett, D.W., and Farrell, H.E., 1991. Effect of reservoir depletion and pore pressure drawdown on in situ stress and deformation in the Ekofisk Field, North Sea. In: Roegiers, Editor, *Rock Mechanics as a Multidisciplinary Science*, Balkema Rotterdam, ISBN 906191194X, p. 63-72.

Tingay, M.R.P., Hillis, R.R., Morley, C.K., Swarbrick, R.E., and Okpere, E.C., 2003. Pore pressure-stress coupling in Brunei Darussalam – implications for shale injection. In: Van Rensbergen, P., Hillis, R.R., Maltman, A.J., and Morley, C.K., Editors, *Subsurface sediment mobilization*, Geological Society of London, London, Special Publications 2003, v. 217, p. 214-224.

Tingay, M.R.P., Hillis, R.R., Morley, C.K., Swarbrick, R.E., and Drake, S.J., 2005. Present-day stress orientation in Brunei: a snapshot of 'prograding tectonics' in a tertiary delta. *Journal of the Geological Society, London*, v. 162, p. 39-49.

Turcotte, D.L., and Schubert, G., 2002. *Geodynamics*. Cambridge University Press, ISBN 0-521-66186-2.

Van Eck, T., Goutbeek, F., Haak, H., and Dost, B., 2006. Seismic hazard due to small-magnitude, shallow-source, induced earthquakes in the Netherlands. *Engineering Geology*, v. 87, p. 105-121.

Van Eijs, R.M.H.E., Mulders, F.M.M., Nepveu, M., Kenter, C.J., and Scheffers, B.C., 2006. Correlation between hydrocarbon reservoir properties and induced seismicity in the Netherlands. *Engineering Geology*, v. 84, p. 99-111.

Wang, H.F., 2000. Theory of linear poroelasticity with applications to geomechanics and hydrology. Princeton University Press, ISBN 0-691-03746-9.

Whitehead, W.S., Hunt, E.R., and Holditch, S.A., 1987. The effects of lithology and reservoir pressure on the in-situ stresses in the Waskom (Travis Peak) Field. *Society of Petroleum Engineers*, SPE 16403.

Woodland, D.C., and Bell, J.S., 1989. In situ stress magnitudes from mini-frac records in western Canada. *Journal of Canadian Petroleum Technology*, v. 28 (5), p. 22-31.

Zheng, Z., Kemeny, J., and Cook, N.G.W., 1989. Analysis of borehole breakouts. *Journal of Geophysical Research*, v. 92, no. B6, p. 7171-7182.

Zienkiewicz, O.C., and Taylor, R.L., 1994. *The finite element method*. Vol. 1&2, McGraw Hill Book Company, London.

Zoback, M.D., Moos, D., Mastin, L.G., and Anderson, R.N., 1985. Well bore breakouts and in situ stress. *Journal of Geophysical Research*, v. 90, p. 5523-5530.

Zoback, M.L., and Zoback, M.D., 1988. Tectonic stress field of the continental United States. In: Pakiser, L., and Mooney, W., Editors, *Geophysical framework of the continental United States*, GSA Memoir.

Zoback, M.D., and Zinke, J.C., 2002. Production-induced normal faulting in the Valhall and Ekofisk oil field. *Pure and Applied Geophysics*, v. 159, p. 403-420.

Zoback, M.D., Barton, C.A., Brudy, M., Castillo, D.A., Finkbeiner, T., Grollimund, B.R., Moos, D.B., Peska, P., Ward, C.D., and Wiprut, D.J., 2003. Determination of stress orientation and magnitude in deep wells. *International Journal of Rock Mechanics and Mining Sciences,* v. 40, p. 1049-1076.